Investigation of Ordered Shell Nanoparticles as Catalytic Platforms for Organic Synthesis

by

Benjamin H. Wunsch

B.S., Materials Science and Engineering
Arizona State University, 2003

SUBMITTED TO THE DEPARTMENT OF MATERIALS SCIENCE AND ENGINEERING
IN PARTIAL FULFILLMENT OF THE REQUIREMENT FOR
THE DEGREE OF

DOCTOR OF PHILOSOPHY IN MATERIALS SCIENCE AND ENGINEERING

at the

MASSACHUSETTS INSTITUTE OF TECHNOLOGY

February 2009

Signature of Author: _____
Department of Materials Science and Engineering
December 11, 2008

Certified by: ____________________
Francesco Stellacci
Associate Professor of Materials Science and Engineering
Thesis Supervisor

Accepted by: _________
Christine Ortiz
Associate Professor of Materials Science and Engineering
Chair, Department Committee for Graduate Students

Abstract

By observing the molecular structure of nature, the field of nanotechnology is exploring the significant versatility and complexity of the local, molecular environment. Through the careful positioning of the components of atoms and molecules into well-defined patterns or structures, unique properties and functions can be developed that are not obtainable by the basic components alone. This structure of the local environment is deeply important to catalysis, in which the catalyst affects a chemical transformation without being consumed itself. In pursuit of control over local molecular structure, previous work has discovered a general, spontaneous ordering of long, aliphatic molecules on the surfaces of nanoparticles. This ordering generates stripe-like domains, termed *ripple domains*, which have widths less than a nanometer and well-defined spatial separations. This structuring reminds us of the sub-nanometer ordering seen in biological enzymes, and we seek to investigate catalytic reactions occurring at the interface of the ripple domain interface as a possible new method in organic synthesis.

Using nanoparticles as my chosen *platform* for the ripple domain, I have conducted research to test the hypothesis that the local ordering in the ripple domain shell can improve the catalytic rate of reaction. I am guided by recent evidence that the unique ripple domain morphology can cause ordering in the solvation shell that surrounds the nanoparticle, and thus alter the surface energy observed on the interface. Our investigation has found that when ripple domain gold-core nanoparticles synthesized with an imidazole terminated ligand are used in the general acid-base hydrolysis of an aromatic ester that the catalytic rate is modulated by the presence of the ripple domain, however the degree of modulation varies substantially between synthetic batches, preventing a conclusion of any statistical significance on the ability of the ripple domain to influence the catalytic reactivity. In mixed ethanol: water solvent I find that the ripple domain can modulate the catalyst rate in a non-monotonic manner, and when compared to a homo-ligand non-ripple catalyst particle, the modulated catalyst rate can be either enhanced or attenuated depending on the ligand ratio used. In pure water, non-ripple, homo-ligand catalyst particles have higher catalytic rates than ripple-domain particles; however the binding constant and attempt frequency of these types of particles is modulated by changes in the ripple domain, and provides evidence that the monolayer structure is affecting catalysis by producing a local environment capable of holding a reactive intermediate state. The results provide a beginning link between nanoparticle monolayer morphology and catalysis, and open the way to developing nanoparticles as selective catalysts based on changes in the structure of the monolayer.

Acknowledgements

This work has benefited in great part to my advisor Franesco Stellacci, who has been a guiding mentor and good friend during my graduate endeavors and has supported and helped me through difficult times in my career. I am grateful to all my co-workers and friends within my research group and who I've met along the way. Finally, most importantly, I'm deeply indebted to my wonderful parents, Charles and Amy Wunsch, to my brother Evan, and to my whole family, who have helped me to this point and have always been a house of warmth and love for me in all the long trials.

Table of Contents

Chapter 1 – Introduction

A catalyst is a substance that shortens the time of a chemical transformation, a chemical machinery with a function that allows it to change the energy state or physical arrangement of a group of atoms [1-3]. Catalysts come in many forms – biological enzymes and ribozymes, solid surfaces, organometallic complexes, molecules, or single atoms. Even ice has been found to be a catalyst, and it could be argued that many crystals could be considered primitive autocatalysts [4]. Such a seemingly disparate source of catalysts speaks to the point that catalysis is not so much a phenomenon about *what*, as about *where*. To accelerate a reaction requires placing the right energy or atomic structure in the right place at the right moment. A local environment that affords atoms the opportunity to arrange their chemical structure without destroying the environment itself is a catalyst. We emphasize this idea that the local environment where the catalytic transformation takes place is important as the basic inspiration for this thesis. Herein we explore a new medium for catalysis, one which provides a local environment for modifying catalytic reactions – *nanoparticles with locally ordered domain shells.*

The work contained in this thesis investigates how morphology, in the form of phase ordering in the nanoparticle monolayer, can affect organic catalysis. *Nanoparticles*, as referred within, are metal crystal cores < 50 nm in diameter, encapsulated by a shell of ligand molecules which bond to the core and prevent its aggregation with other crystals. This shell of ligands is termed a *monolayer*, a single layer of molecules that provides the physical and chemical properties to the particle. The monolayer shell imparts stability and affects what solvents the nanoparticles dissolve into, allowing colloidal solutions to be generated. These materials have become a major part of nanotechnology research in the past decades, as machinery for interacting with biology, and exploring new physics and chemistry.

Nanoparticles have been proven to be viable catalysts [5-8]. Typically the core crystal has been used as the catalytic machinery, where molecules diffuse to the core and react, allowing metal and organometallic catalysts to be reborn in an easily prepared, handled, and separated colloid [5,9]. However, work is beginning to focus on the nanoparticle monolayer as a catalytic machine, where substrates interact with catalytic specie embedded in the ligand shell [10,11]. Initial work has already shown that the plurality of the monolayer shell and its unique molecular structure can produce surprising catalytic effects, and has created the concept of monolayer-driven nanoparticle catalysts as a type of prototype enzyme or protein [11,12]. Both nanoparticles and enzymes are of the same size and compactness[1], and their catalysis occurs completely at the interface between solvent and surface [1,13,14]. Now interest is growing in understanding how to control catalysis in nanoparticle monolayers to the level of molecular control seen in biology.

This thesis explores a unique type of ordering in nanoparticle monolayers, *ripple domain phase separation*, in which two different molecules form a monolayer with bands or "ripple" phases of alternating composition ~ 1-1.5 nm width [15-17]. The question addressed in this thesis is whether the ripple domain can modulate, either by enhancing or attenuating, catalysis as a function of monolayer morphology. The essential idea is to see if the ripple domain's structure influences the local, physical environment of the catalyst and therefore affects it reactivity. To test this hypothesis, nanoparticles were prepared using an imidazole terminated ligand as a general acid/base catalyst, in combination with different alkanethiol filler ligands (1-octanethiol, 1-hexadecanethiol, or 16-mercaptohexadecanoic acid), and tested in the catalytic hydrolysis of 2,4-dinitrophenyl acetate. It was found that depending on the system of ligands used that the ripple domain morphology could indeed modulate catalysis with respect to a non-ripple, homo-ligand catalyst particle but that the modulation deviated strongly between different batches of the same type of nanoparticles. This prevented an acceptance of the hypothesis, but provides a foundation to guide further work to study catalytic, ripple domain nanoparticles. The binding constant and attempt frequency of the catalysis reaction were found to be modulated by ripple morphology as well, in a reproducible manner, suggesting the monolayer affects catalysis by interacting and structuring the bound substrate with the catalyst. These results open the way for studying monolayer morphology as a general concept in surface catalysis.

Chapter 1 References

1. Bugg, T. *Introduction to Enzyme and Coenzyme Chemistry*, (Blackwell Publishing, Oxford, 2004).
2. Bruice, T.C. & Benkovic, S.J. Chemical Basis for Enzyme Catalysis. *Biochemistry* **39**, 6267-6275 (2000).
3. Chorkendorff, I. & Niemantsverdriet, J.W. *Concepts of Modern Catalysis and Kinetics*, (Wiley-VCH, 2003).
4. Trinks, H., Schroder, W. & Bierbricher, C.K. Ice and the Origin of Life. *Origins of Life and Evolution of Biospheres* **35**, 429-445 (2005).
5. Bonnemann, H. & Richards, R.M. Nanoscopic Metal Particles - Synthetic Methods and Potential Applications. *European Journal of Inorganic Chemistry*, 2455-2480 (2001).

---

[1] *Compactness* is the ratio of a system's atomic volume divided by the total spatial volume it occupies.

6. Crooks, R.M., Zhao, M., Sun, L., Chechik, V. & Yeung, L.K. Dendrimer-Encapsulated Metal Nanoparticles: Synthesis, Characterization, and Applications to Catalysis. *Accounts of Chemical Research* **34**, 181-190 (2001).
7. Daniel, M.C. & Astruc, D. Gold Nanoparticles: Assembly, Supramolecular Chemistry, Quantum-Size-Related Properties, and Applications Toward Biology, Catalysis, and Nanotechnology. *Chemical Review* **104**, 293-346 (2004).
8. Schlogl, R. & Aba Hamid, S.B. Nanocatalysis: Mature Science Revisited or Something Really New? *Angewandte Chemie International Edition* **43**, 1628-1637 (2004).
9. Henry, C.R. Chapter 3 - Nanoparticle Catalysis. in *Nanocatalysis* (ed. Heiz U, L.U.) (Springer, Berlin, 2007).
10. Fan, J. & Gao, Y. Nanoparticle-Supported Catalysts and Catalytic Reactions-A Mini-Review. *Journal of Experimental Nanoscience* **1**, 457-475 (2006).
11. Pasquato, L., Pengo, P. & Scrimin, P. Nanozymes: Functional Nanoparticle-based Catalysts. *Supramolecular Chemistry* **17**, 163-171 (2005).
12. Guarise, C. et al. Cooperative Nanosystems. *Journal of Peptide Science* **14**, 174-183 (2008).
13. Branden, C. & Tooze, J. *Introduction to Protein Structure*, (Garland Publishing, New York, 1999).
14. Finkelstein, A.V. & Ptitsyn, O.B. *Protein Physics: A Course of Lectures*, (Academic Press, San Diego, 2002).
15. Centrone, A., Hu, Y., Jackson, A.M., Zerbi, G. & Stellacci, F. Phase Separation on Mixed-Monolayer-Protected Metal Nanoparticles: A Study by Infrared Spectroscopy and Scanning Tunneling Microscopy. *Small* **3**, 814-817 (2007).
16. Jackson, A.M., Myerson, J.W. & Stellacci, F. Spontaneous Assembly of Subnanometre-Ordered Domains in the Ligand Shell of Monolayer-Protected Nanoparticles. *Nature Materials* **3**, 330-336 (2004).
17. Jackson, A.M., Hu, Y., Silva, P.J. & Stellacci, F. From Homoligand- to Mixed-Ligand-Monolayer-Protected Metal Nanoparticles: A Scanning Tunneling Microscopy Investigation. *Journal of the American Chemical Society* **128**, 11135-11149 (2006).

2.1 Monolayer Protected Nanoparticles

In general, a nanoparticle is any substance with all spatial dimensions in the nano-scale (~ 1 – 100 x 10^{-9} m). In this study we are concerned with the family of particles generated by the encapsulation of a metal crystal core by a shell of organic molecules, termed *monolayer-protected-metal-clusters* (MPCs or MPMCs) or simply *nanoparticles* [1] (**Figure 2.1.1**). The shell consists of a single layer – known as a *monolayer* – of organic molecules termed *ligands* [2]. The core can be composed of almost any metal, as has been demonstrated extensively [3], but primarily is made of coinage metals (e.g. gold, zinc, copper) and catalytic, mid-transition metals (palladium, platinum, rhodium, iron, cobalt, nickel, etc.). The organic shell acts as a barrier to separate the core from other particles, preventing aggregation. As a consequence, the ligands dominate the interface of the particles and determine their physical / chemical properties.

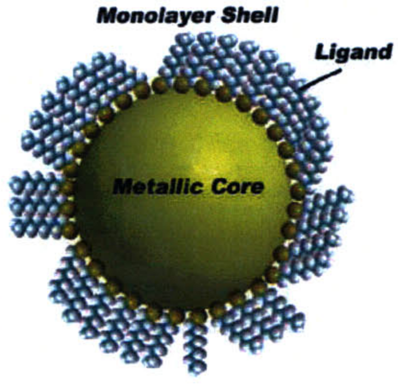

Figure 2.1.1: Schematic of an ideal monolayer-protected-metal-cluster – *nanoparticle*. Organic ligand molecules are bound to a metallic crystal through an anchoring head group (small golden orbs), forming a monolayer shell around the crystal.

The gold-core/alkanethiol-monolayer nanoparticle is used frequently in material science due to the ease of synthesis, the strong gold-thiol bond stability, and well established chemistry. As this current work is based on gold nanoparticles I will focus on their properties, in particular the ligand monolayer. Gold nanoparticle synthesis, structure and applications have been extensively studied and reviewed in the literature [1,2,4]. Much of what is known of the monolayer shell on gold nanoparticles has come from the study of the thiol-gold self-assembled monolayer. Self-assembled monolayers (SAMs) are produced from individual ligands that bind to a surface in a packed, two-dimensional lattice [5-8]. The model SAM is the oil-like alkanethiol ligand on a Au (111) surface (seen in **Figure 2.1.2**) which provides the basic understanding of the molecular structure and properties of SAMs [5,6]. The important features to note of the thiol-gold SAM are that the strong gold-thiol bond packs ligands into a two-dimensional lattice in which each ligand is tilted (~32-34^{0}) and twisted (0^{0}-90^{0}) to reduce dispersion energies. The terminal group of the ligand forms the new surface between the monolayer and the surrounding medium, and determines the monolayer's properties.

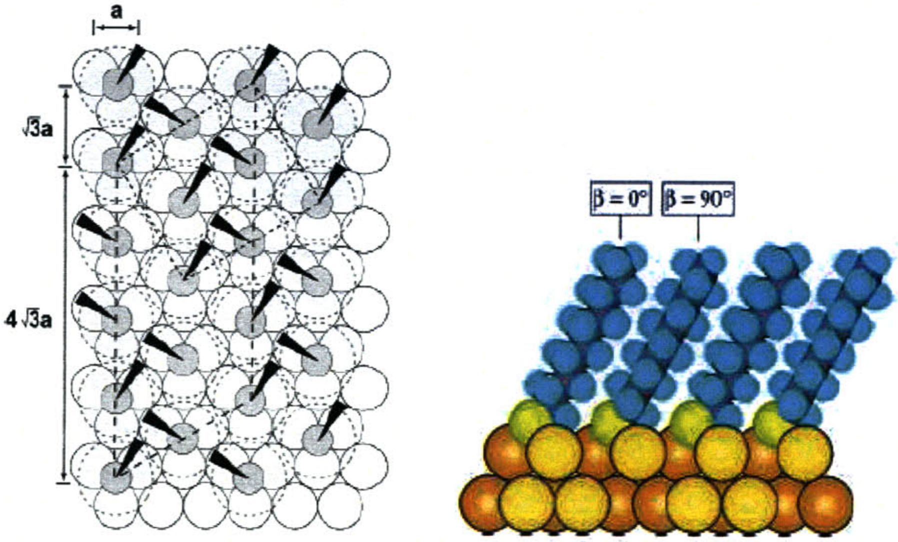

Figure 2.1.2: (Left) Schematic of an ideal Au(111) surface coated in a close-packed alkanethiol self-assembled monolayer (SAM), showing the anchoring thiolates as gray circles and the super-lattice as the dashed rectangle. The parameter ***a*** is the gold lattice spacing. The black wedges represent the twist angle of the extended alkane chain. **(Right)** Schematic cross-section of alkanethiols on a gold surface. The β angles correspond to the twist angles shown in the schematic to the left. The figure has been taken from reference [5] without permission.

One significant, recent discovery on gold-thiol SAMs has shown that the interface between the gold and monolayer is disrupted by gold vacancies [9]. These vacancies are formed due to the thiol monolayer extracting gold atoms out of the core to generate a corrugated interface of gold-thiol-gold bonds, known as *staple motifs* [10,11]. The same effect occurs in nanoparticles, except that it is accentuated by the nanoparticle curvature, allowing the interface to relax to a higher degree and cause compression of the monolayer surface. This compression of the interface allows tighter packing of ligands in the nanoparticle monolayer, from 30% surface coverage up to ~65% [1,12-14]. Simulations have shown that well formed monolayers can still exist despite the curved nanoparticle interface [15-19] (**Figure 2.1.3**).

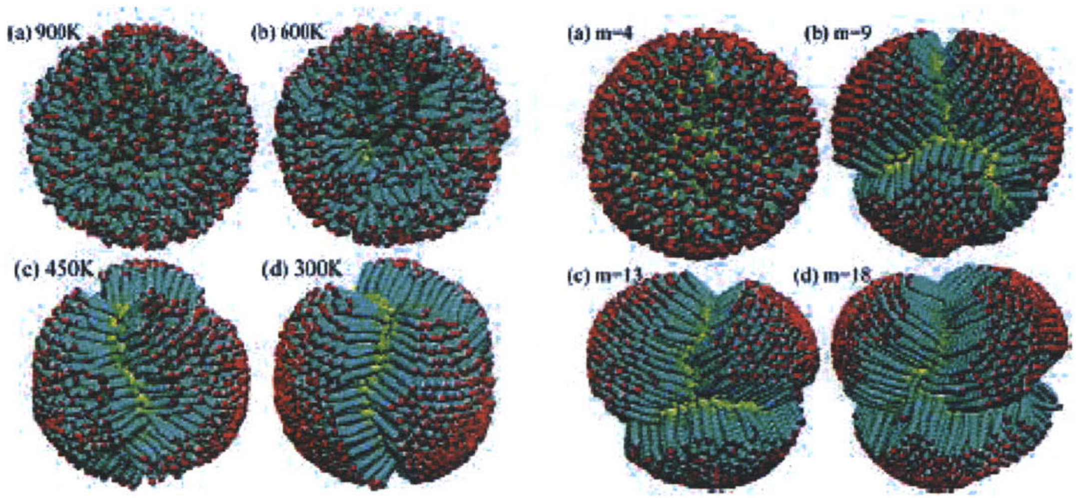

Figure 2.1.3: Simulated structures of alkanethiols on spherical gold cores at various temperatures **(Left)** and ligand lengths (m = number of methylene –CH_2- units in the alkane chain) **(Right)**. The figure has been taken from reference [15] without permission.

It is generally difficult to obtain crystallographic data of the monolayer on nanoparticles (> 2-3 nm diameter) due to the inability to form supercrystals capable of being used in diffraction studies. Studies of well-defined nanoparticle clusters (< 500 gold atoms) have demonstrated that thiol atoms form bridging states between the gold atoms [11,20-24]. A recent example of a 102 Au atom nanoparticle gave the first crystallographic construction to 0.115 nm resolution of the monolayer/core [23]. In this work, p-mercaptobenzoic acid homo-ligand nanoparticles crystallized, exhibiting a C2/c space group and, interestingly, two enantiomeric states produced by the two spins or "whorls" of the monolayer around the gold core, as seen in **Figure 2.1.4**. The staple motif, as seen in SAM studies, was also clearly present on the nanoparticle and constituted the major bonding structure at the metal/ligand interface. Crystallographic studies of this form provide a basic understanding of the detailed molecular structure of ligand monolayers on nanoparticles.

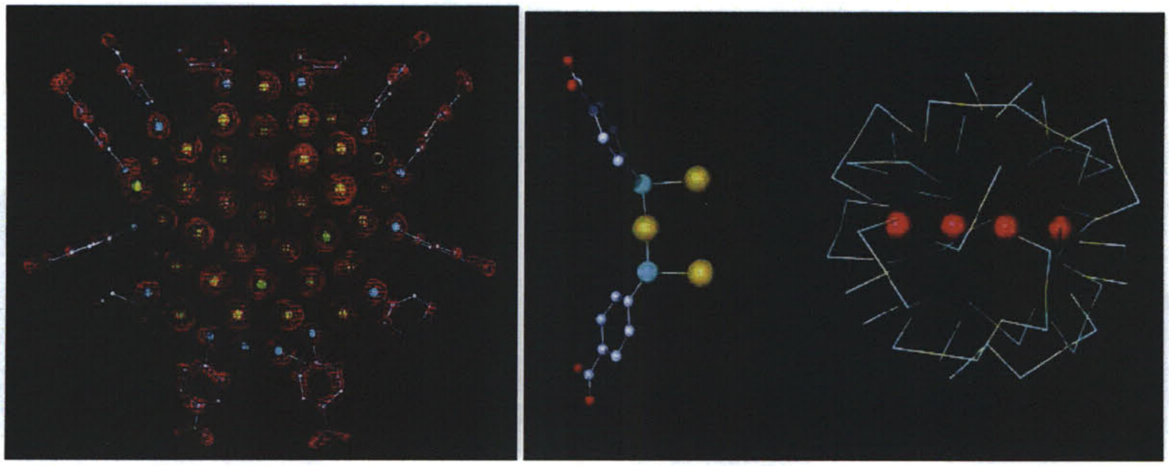

Figure 2.1.4: (Left) Computer rendering of the 102 atom gold particle for which crystallographic detail of the monolayer. The electron density is drawn in a red mesh. The p-mercaptobenzoic acid ligands are shown with blue cores, the gold atoms with yellow cores. The layer of ligands in front has been removed to show the crystal structure below. **(Middle)** Rendering of the gold atom μ -bridge or "staple motif" between two ligands in the particle monolayer. Sulfur atoms are the cyan spheres, gold atoms are the yellow spheres. **(Right)** Schematic map of the ligand-gold-ligand bridges or "staples" which make up the monolayer shell. The red atoms in the middle detail the gold atoms crossing through the core of the particle and give a sense of proportion. The figure has been taken from reference [23] without permission.

2.2 Mixed-Ligand Monolayers and the Ripple Domain Phase on Nanoparticles

When two distinct ligands are used to form a monolayer, either with large differences in the hydrocarbon back-bone, changes in exclusion volume of head groups, or different head group polarities, phase separation can be observed [8,25-31]. Whether and to what extent phase separation occurs depends on the type of ligands used, the SAM preparation, and the time scales of the observation [5,6]. It is found that even in a two-dimensional lattice dominated by the sulfur-gold bond that strong interactions between the terminals of the ligands and the surrounding medium can drive clustering and phase separation.

When two distinct aliphatic hydrocarbon ligands are used to synthesize gold nanoparticles a unique phase separation occurs in which ligands form stripe-like phases that circumscribe around the monolayer shell [32-35]. Originally, this phase separation was seen under scanning probe microscopy as bands or *ripples*, and this phase separation is termed *ripple domain phase* and the individual homo-phases as *ripple domains* [32] **(Figure 2.2.1)**. The ripple domain can be visualized experimentally using Scanning Tunneling Microscopy (STM) (**Figure 2.2.1**) or liquid cell Atomic Force Microscopy (AFM) of nanoparticles, and has been generated in simulations as well as predicted by geometric considerations [33,34,36].

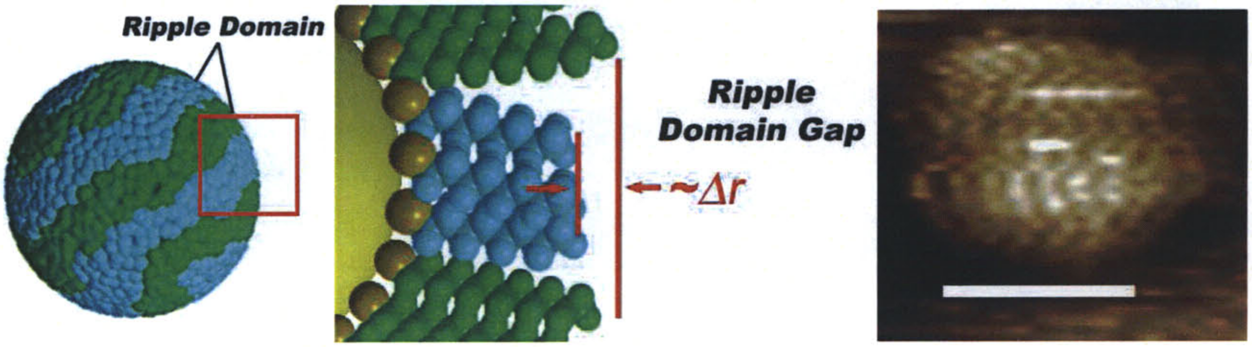

Figure 2.2.1: (Left) Simulated ripple domain phase on a gold nanoparticle core, showing the characteristic ripple domains. A single ripple domain is defined by the set of two stripes, each of a single ligand type (the figure has been taken from reference [34] without permission). The red box denotes the surface domain structure shown in zoom **(Middle)**, defining the ripple domain gap and its change in radial length, Δr. In this schematic, the green alkanethiols are longer than the cyan. **(Right)** Scanning tunneling microscope image of a ripple domain nanoparticle, 5 nm scale bar (the figure has been taken from reference [37] without permission). The light-dark bands are caused by changes in electronic density as the probe rasters over the ripple domain gaps (the figure has been taken from reference [33] without permission).

The ripple domain can be considered the phase configuration that maximizes the number of ligands that sit on an interface, allowing longer ligands to have free volume to maximize entropy. In a homo-ligand particle, all of the ligands are of the same length and thus pack with the same projected area and radial height. This packing impedes the hydrocarbon chains from moving, reducing entropy; but allowing close-packing to minimize dispersion force energy. However, if one ligand is longer than the other it will have greater entropy due to the mobility of the hydrocarbon chain portion not bound in the monolayer. If this entropic term is smaller than the enthalpic packing of long and short ligands, there is little difference if one ligand packs next to its own type or the other and a mixed phase monolayer occur. However, if the entropic term dominates then it becomes energetically favorable for the longer ligands to pack next to the shorter ligands. This would normally disperse the long ligands so as to maximize their surrounding by short ligands; however the long ligands also have a driving enthalpy to associate and close back. If the longer ligands formed a single phase, then a majority of the molecules would again lose their conformational freedom (save for those by defects or the phase border).

Unless the close-packing of the longer ligands is strong enough to overcome the entropic term, the longer ligands will phase separate into thin ripple domains which place the majority on the phase border and allow them to maintain the balance between their conformation freedom and enthalpy of packing. The result is the ripple domain, in which the width of the domain is determined by the degree of separation of long and short ligands into separate strips. Typical domain widths are experimentally found and calculated from simulation as ~ 0.6-1.5 nm (1 to 3 ligands wide) [33,34], as quantified in **Figure 2.2.2**.

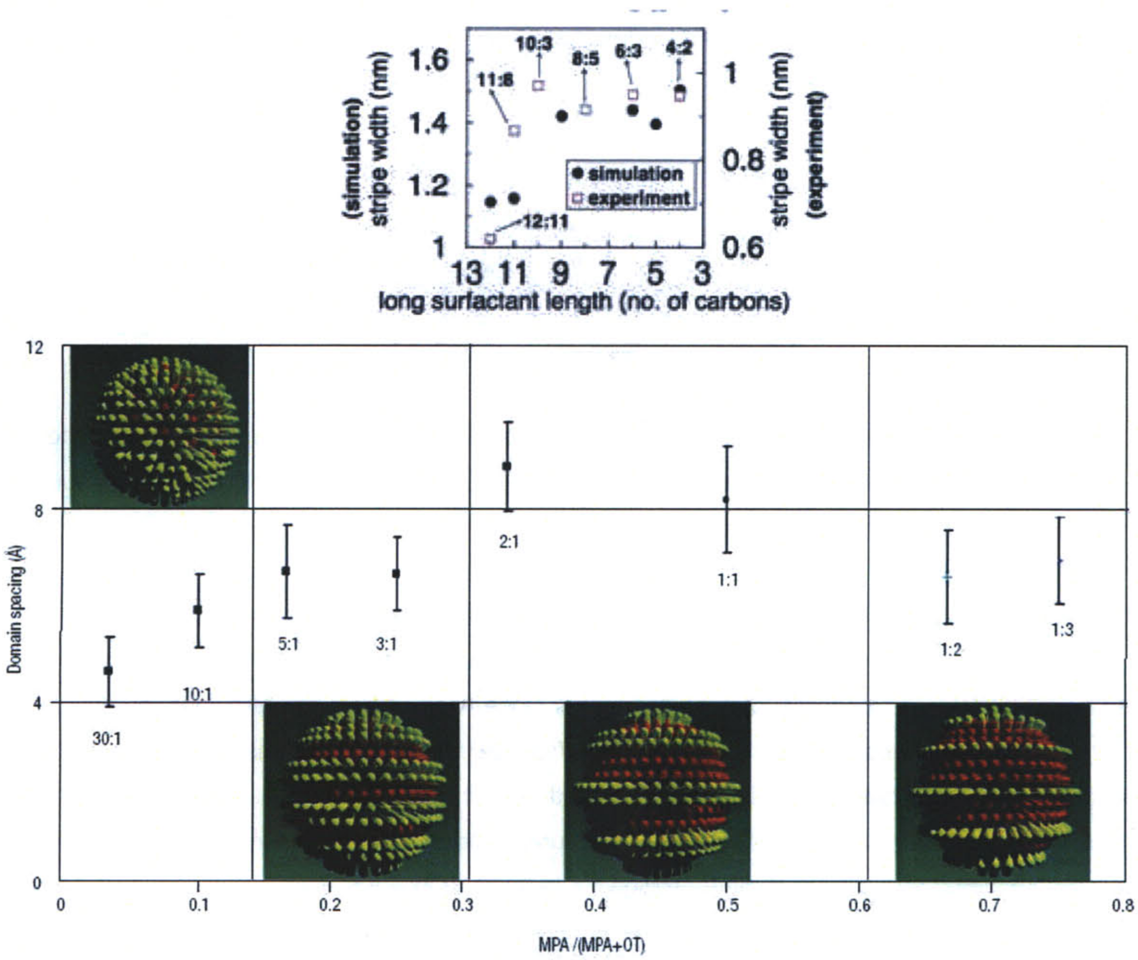

Figure 2.2.2: (Top) Ripple domain width (stripe width) as a function of ligand length given from simulated and experimental (from scanning probe measurement)data (the figure has been taken from reference [34] without permission). **(Bottom)** Experimentally determined domain spacing as a function of particle ligand ratio. (the figure has been taken from reference [32] without permission).

The physical theory of ripple domain formation is not unique to nanoparticles; it predicts that flat surfaces should exhibit ripples as well, and indeed this has been verified [34]. Nanoparticles, however, have high curvature due to rapid change in orientation across the facets of their poly hedral cores. Curvature is implicitly important to the ripple domain because it affects the splay of the ligand monolayer, and hence the amount of conformation freedom available to the longer ligand [33]. With high curvature (small radius) the ligand splay is higher, providing greater free volume between ligands and thus a larger conformational entropy contribution. For small radii (< 3 x the length of the ligands – e.g. for a 1 nm long ligand such as 1-octanethiol, a nanoparticle of ~ 3 nm), it is predicted that ligands form Janus-type particles (**Figure 2.2.3**) in which each ligand forms a single homologous phase [34,38]. Experimentally and in simulation, it is seen that particles with large radii (~ 10 x the length of the ligands) transition from ripple domains to *worm-like domains* in which individual homo-ligand stripe phases cannot circumscribe the particle radius [34] (**Figure 2.2.3**).

Figure 2.2.3: Simulation generated images of Janus-type **(Left)**, ripple domain **(Middle)** and worm-like domain **(Right)** nanoparticles. The figure has been taken from reference [34] without permission.

Experiment and simulation suggest that the difference in length that generates ripple domain phases for aliphatic ligands is between 3 and 10 methylene carbons; shorter lengths give too little entropic freedom and longer lengths begin to favor close-packing to minimize dispersion energy [32-35]. The physical theory depends only on the difference in the ligand lengths; it is not known what the absolute lengths of the ligands can be although it is considered that ligands beyond 12-14 methylene carbons are affected less by curvature, have less conformational entropy, and thus close-pack better and reduce ripple formation [33]. In addition, bulky ligands which occupy a large volume and projected area on the core surface disrupt the ripple domain [32,33,39]. It is not understood what polar and charged groups do to the ripple phase, although both have been used to form ripple domains [37]. Ripple domains generally occur when the ligand ratio varies between 2:1 and 1:2 (33% to 67% longer ligand); outside this window the monolayer is a mixed phase of single or small clusters of ligands [32]. The ripple domain provides a method for self-assembling molecules at the nano-scale in large quantities. There is no long-range order in the surface organization of the ripples; however, the assembly orders the structure in the radial direction and in the width of the ripple domains (gaps) through selection of the two ligands.

Ripple domain morphology imparts unusual physical properties to nanoparticles. The presence of ripple domains in the particle shell has been conjectured to be linked with non-monotonic behavior in the solubility [40]. Particles of varying ratios of 1-octanethiol (OT) and 3-mercapto-1-propionic acid (MPA) were shown to have varying solubility in ethanol, with maximum solubility at 50% MPA, and minimal solubility at 0% and 100% MPA [40]. Furthermore, 25% MPA particles are highly soluble in ethanol, but are almost totally insoluble in methanol, despite the fact methanol and ethanol differ only by one methylene unit [40].

In another study in my group, by Verma and coworkers, ripple and non-ripple domain nanoparticles were tested to see differences in their capacity to penetrate through cellular membranes [39]. In these studies, three types of particles were used: particles with ripple domains formed of 1-octanethiol and 11-mercapto-undecane-1-sulfonic acid (MUS), homo-ligand non-ripple particles of MUS, and non-ripple particles formed by MUS and 3,7-dimethyl-octane-1-thiol, which I call a *disrupted domain* (**Figure 2.2.4**). The disrupted domain is caused by the branching methyl groups on the octanethiol backbone, which disallow close-packing and thus prevent ripple domains from forming. The disrupted domain particles present the same ratio of polar / non-polar ligands as the ripple domain particles; the only difference is in their structure – the disrupted domain is simply a random mixture of the two ligands – allowing a direct comparison of how structure influences the nanoparticles.

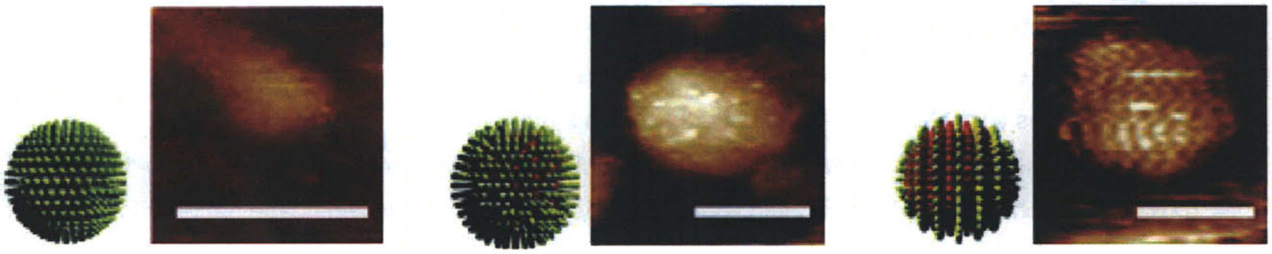

Figure 2.2.4: Schematic images and scanning tunneling microscope images of the nanoparticle monolayer morphologies used in the study of nanoparticle cellular uptake. **(Left)** Non-ripple homoligand nanoparticle, **(Middle)** disrupted domain nanoparticle, **(Right)** ripple domain nanoparticle. The scale bars are all 5 nm. The figure is taken from reference [39] without permission.

In the study, mouse cells were incubated with the nanoparticles and the uptake of nanoparticles observed. It was found that ripple domain particles can easily enter into the cell's cytosol, whereas the non-ripple homo-ligand and disrupted domain particles are absorbed only through a endocytoic vesicle, demonstrating a clear effect of the monolayer structure on the particles' properties [39].

These solubility and biological effects cannot be associated with the particle size or the chemical properties of the dominate ligand type. In an attempt to understand these physical observations better, a study was conducted in my group on the surface energy of ripple nanoparticles [36]. The results and theory of this study are the launch points for the current thesis.

2.3 Surface Energy of Ripple Domain Nanoparticles

As nanoparticles represent surfaces which interact with their surrounding medium through the monolayer, one way to quantify effects of the nano-scale domain morphology is to look for changes in the macroscopic surface properties. A study conducted in my group focused on a combined experimental and simulation study of the three-phase work of adhesion, W_{SLS}, of a thin film of ripple domain and non-ripple homo-ligand nanoparticles [36]. The work W_{SLS} is the energy stored between two surfaces which have been removed from a liquid medium; in this case the energy between the monolayer and either water (removed from air) or an AFM probe tip (removed from water). Conceptually W_{SLS} can be thought of as the combination of energy to create the two surfaces in the liquid medium, remove the liquid from the surfaces, and then bringing the surfaces together. Therefore W_{SLS} is a measure of the integral of forces at the two surfaces. The structure at the interface directly affects what forces are present and in what magnitude, thus a measure of the work of adhesion is a probe of surface structuring. In the system studied the nanoparticles were formed of 1-octanethiol (OT) and 6-mercapto-hexane-1-ol (MH), a hydrophilic hydroxyl terminated ligand. A series of SAMs and mixed-ligand nanoparticle thin films were formed at various ratios of OT:MH and the W_{SLS} measured by both macroscopic contact angle measurements and microscopic amplitude modulation atomic force microscopy (AM-AFM), shown in **Figure 2.3.1**.

It was observed that the SAMs produced a linear response to OT:MH ligand ratio, suggesting the composition of the monolayer determined the surface energy. However the mixed-ligand nanoparticle thin films show a non-linear (modulated) rise in W_{SLS}. This implied that the composition alone did not determine the surface energy for these particles and that one must consider the detailed microstructure. The strong correlation between the data of the AFM and contact angle methods supports that both measurements are seeing the same effect from the monolayer surface. The presence of pinning effects or of hysteresis due to a restructuring of the surface by the presence of water, both effects which do not depend on specific morphology, cannot be controlling the results since the observed modulation is present in both the macroscopic contact angle measurements and the nanoscopic AFM measurements. The relevant result is that the mixed-ligand ratios within the ripple domain regime show marked changes (of ΔW_{SLS} max ~ 70%) in surface energy [36].

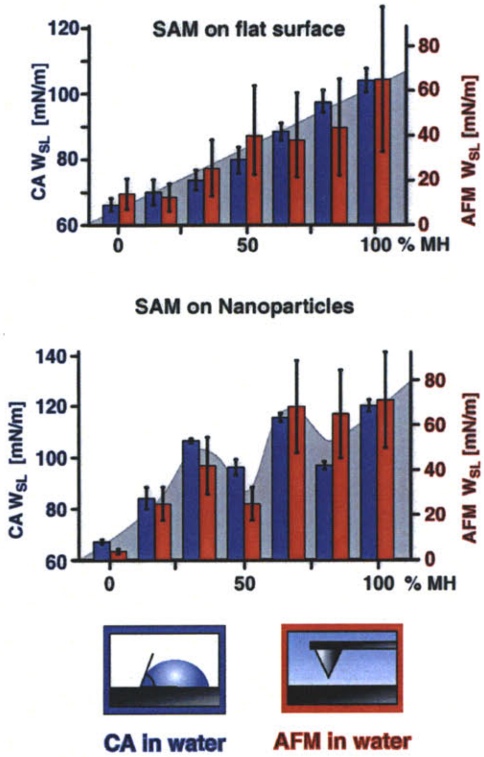

Figure 2.3.1: Work of adhesion, W_{SLS} , as a function of ligand ratio for flat SAMs **(Top)** and films of ripple domain nanoparticles **(Middle)**. The monolayers are made of 1-octanethiol / 6-mercapto-hexane-1-ol (MH) ligand ratios. The blue/gray bar graphs are from contact angle (CA) measurements; the red line is from atomic force microscopy measurements. **(Bottom)** Schematic representations of the measured water structure in contact angle *(left)* and atomic force microscopy *(right)*. The figure has been taken from reference [36] without permission.

To explain this phenomenon, a theory was proposed that combined the concepts of (1) microscopic cavitation and (2) enhanced hydrophilicity [36]. (1) Microscopic cavitation is the forming of small voids over alternating hydrophobic-hydrophilic molecular structure by solvent molecules. The solvent bridges over molecules it is not attracted to, and these nano-scale voids alter the solvation shells (solvent structure) and the hydrophobicity of the resulting interface. (2) Enhanced hydrophilicity is an effect where a hydrophilic (polarizable) molecule increases in hydrophilicity when embedded in a local, hydrophobic environment. A dipole embedded in a polar environment will have its local electrostatic field attenuated by the surrounding charge; however in a hydrophobic (non-polar) environment there is little attenuation of the dipole's local field, allowing a stronger interaction with other polar molecules.

In ripple domains, the two effects generate an interface at which solvent molecules become more highly structured around the domains. This first solvation shell forms most of its secondary bonding to the ripple domains and cannot interact strongly with the second, third, etc. solvation shells, reducing the effective solubility of the particles. In effect, the ripple domain harvests solvent to form a new "shell" that becomes the surface with which the solvent interacts. As W_{SLS} is a measure of how the two surfaces (the solid ripple domain and the liquid solvent) interact, we see that at the molecular level this interaction is dominated by these voids and strong hydrophilic centers forming "tighter" solvation shells. **Figure 2.3.2** shows the work of adhesion as a function of ripple spacing, n, for hydrophobic and hydrophilic domains, demonstrated a modulation behavior with composition.

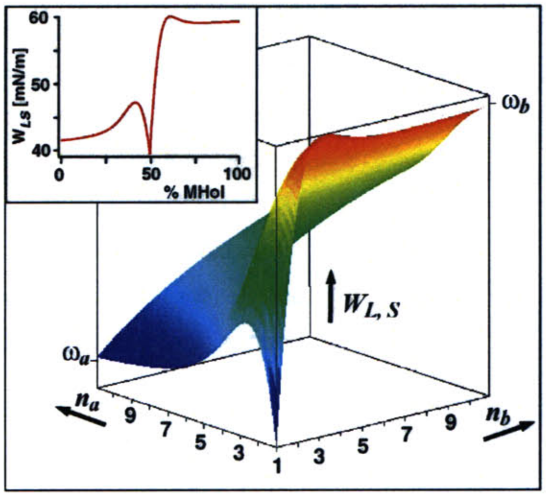

Figure 2.3.2: Plot of the work of adhesion as a function of the hydrophobic ripple domain width (n_a) and hydrophilic ripple domain width (n_b). The inset is the curve traced out by moving along the x-y edge of the graph – i.e. going from completely hydrophobic to hydrophilic domains. MHol is the percentage of 6-mercapto-hexane-1-ol in a 1-octanethiol ripple domain nanoparticle. The figure has been taken from reference [36] without permission.

The data and theory from this study provide the impetus to investigate if these molecular phenomena could be used to perform work in a catalytic system. Enhanced hydrophilicity suggests that a polar catalytic molecule might exhibit an increased reactivity if embedded in a ripple nanoparticle, and the restructuring of the solvent shell could provide a driving force for attracting and binding substrates into catalytic domains.

2.4 Nanozymes

The term *nanozyme* was coined by Scrimin and co-workers to refer to supported catalytic nanoparticles whose monolayers were produced from short peptides and which exhibited some of the same, basic properties of enzymes [41]. However, the term extends to any supported catalyst which uses biochemistry. The first nanozymes and their catalytic rates were investigated by Scrimin and coworkers, and these investigations provide the model for the current work [42]. In these investigations gold core nanoparticles were used with 12-mercapto-N-(2-(1-methyl-1H-imidazol-4-yl)ethyl)dodecanamide (MID) as the catalyst, and 1-dodecanethiol (DT) as a non-reactive, filler ligand (see **Figure 2.4.1**). Homo-ligand DT particles were synthesized and ligand exchanged with MID to produce a 1:1 mixture in the monolayer as determined by NMR [42].

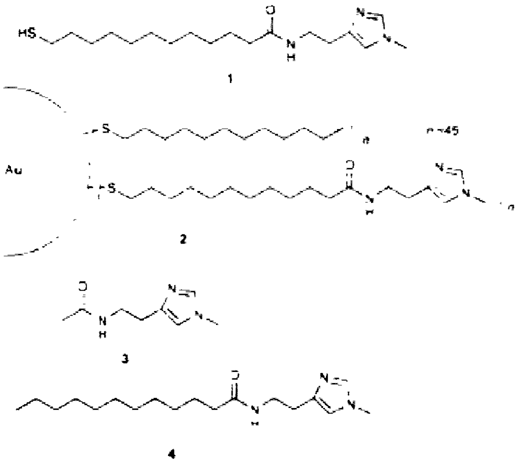

Figure 2.4.1: Schematic of ligands used in Scrimin and coworkers' study.

1. Catalyst ligand 12-mercapto-N-(2-(1-methyl-1H-imidazol-4-yl)ethyl)dodecanamide (MID),
2. Schematic of ligand ratios on nanoparticles.
3. Basic catalytic unit.
4. Free form catalyst for control.

The figure has been taken from reference [42] without permission.

The MID:DT particles were used in a 3:2 ethanol : water solution to hydrolyze 2,4-dinitrophenyl acetate (DNPA) to the free acetic acid (AcOH) and phenol (DNP-OH). The imidazole terminus is the catalytic site, providing a general acid/base function for cleaving water, as well as hydrogen bonding to stabilize the anionic oxide complex. The reaction could be followed *in situ* by a UV-VIS spectrometer as the absorbance signal from the DNPA at 400 nm increases when it is hydrolyzed to DNP-OH. The kinetic curve for these particles was measured at varying pH (4-7) and the catalytic rates obtained. The results from this first study demonstrate, as shown in

Figure 2.4.2, many of the key properties of nanozymes. The catalytic nanoparticle has a larger rate (~ 30x enhancement) compared to the independent, free form catalyst. More interestingly, the nanoparticles exhibit a cooperative peak close to the pKa of the imidazole 3N imine. *Cooperativity* is the observed increase in rate, higher than would be expected by the summation of individual catalysts working independently, implying the catalysts are operating together to produce faster reactions [43]. The suspected reason for the cooperativity in this system is due to the presence of both protonated and de-protonated imidazoles at the pKa. Since the completion of hydrolysis requires both protonation states, in this pKa region the two populations of imidazole states can operate together to complete the transformation. This demonstrates a common method in the work of Scrimin, in which cooperativity is probed by changing the catalyst population of states either through pH or ion concentration.

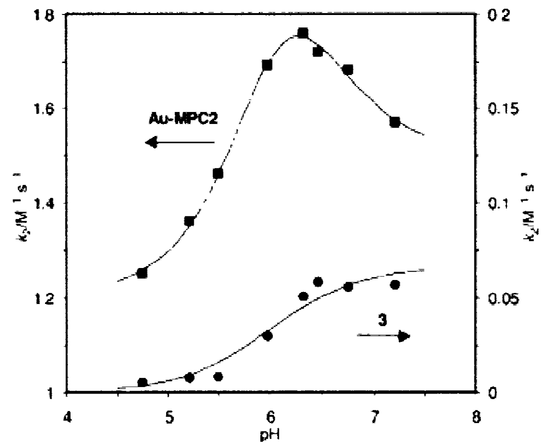

Figure 2.4.2: Catalytic rate, k_2, as a function of acidity from Scrimin and coworkers' work. The upper curve is from the nanoparticles and the lower curve from the free form control catalyst. The peak seen at pH ~ 6.6 for the nanoparticles is the cooperativity peak. The figure has been taken from reference [42] without permission.

This work on nanozymes was further extended by Scrimin and coworkers to short peptide systems on gold nanoparticles, where they could demonstrate various ester hydrolyses and cooperativities [44-47]. In another study, PEG terminated, water-soluble nanoparticles were ligand exchanged with a di-peptide ligand; histidine-phenylalanine [46] (**Figure 2.4.3**). The histidine provides an imidazole (as in the previous system) capable of acting as a hydrogen bond donor and general acid/base catalyst. The phenylalanine serves a dual purpose: (1) it is the carboxylic terminal residue and thus its free carboxylic acid can participate in the catalytic chemistry, and (2) the benzyl moiety is intended to complex with the aromatic substrates: 2,4-dinitrop-phenyl butonate (DNPB) and Z-leucine-p-nitrophenyl ester (Z-Leu-PNP). The combination of the imidazole base and terminal carboxylic acid forms a simple catalytic site that mimics that observed in protease enzymes. As a control, a free form analog of the dipeptide ligand which cannot aggregate in solution was used.

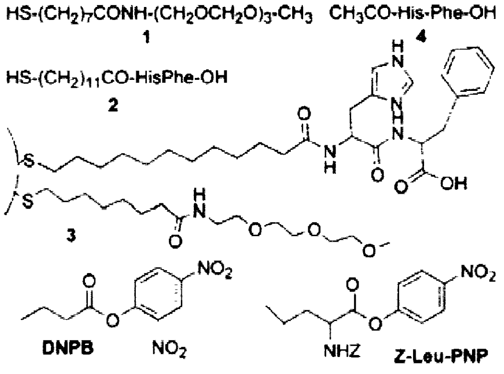

Figure 2.4.3: Schematic of ligands used for the di-peptide catalysis.

1. PEG terminated filler ligand for water solubility.
2. Di-peptide catalyst ligand.
3. Schematic of filler and di-peptide ligand on nanoparticle.
4. Free form di-peptide catalyst for control.

Substrates: 2,4-dinitrop-phenyl butonate (DNPB), Z-leucine-p-nitrophenyl ester (Z-Leu-PNP). The figure has been taken from reference [46] without permission.

The results for the catalytic rate (given as k^2_{app} in **Figure 2.4.4**) show an enhancement in catalytic rate, of ~ 10 – 1000x, and a more complicated cooperativity compared to the control. It is seen in the k^2_{app} that the supported catalyst has two pH transitions at 4.2 and 8.1. These transitions correspond to the pKa's of the carboxylic acid and imidazole base, respectively. In comparison, the k^2_{app} for the control catalyst shows a single transition at pH 6.6, corresponding to the pKa of the imidazole alone. The data show that the nanoparticle confined di-peptide has become more acidic due to its position in the monolayer, having a lower pKa, and that the carboxylic acids are interacting with each other through their negative charge. The anionic nature of the monolayer produces a local environment that prevents the imidazole base from deprotonating (losing the positive charge) and thus shifts the imidazole pKa upwards. As in the first study, the presence of both the activated acid and protonated base in close proximity provides the machinery needed to carry out the catalysis. This is in contrast to the control which, at pH 4.2, shows almost no catalysis because the acids are not coordinating with the imidazole.

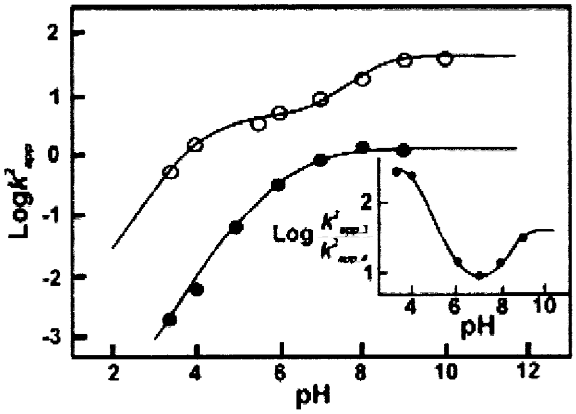

Figure 2.4.4: Logarithm of catalytic rate, k$^{2}_{app}$, as a function of acidity for the dipeptide system. **Open circles** – catalytic nanoparticles demonstrating two transition cooperativity, **close circles** – free form catalyst. **Inset** – ratio of nanoparticle to free form catalyst, demonstrating the cooperativity effect by the transition at pH ~ 6.6. The figure has been taken from reference [46] without permission.

The complex cooperativity was observed in larger peptide systems, the most interesting being a dodeca-peptide designed to further enhance secondary interactions in the hydrolysis of an ester bond [47]. The dodeca-peptide is suspected to form an alpha-helix within the monolayer and contains several active groups – a hisitidine imidazole (pKa 6.4), tyrosine phenol (pKa 9.7), lysine primary amine (pKa 10.4), arginine guanadinium (pKa 12.0), and the terminal carboxylic acid (pKa 4.0) (see **Figure 2.4.5**). As expected, the catalytic rate k$^{2}_{app}$ demonstrated the same multi-step cooperativity, showing three supposed transitions at 4.2, 7.2 and 9.9 (**Figure 2.4.6**). These are assigned to the ionizations of the carboxylic acid, imidazole and either lysine or tyrosine, respectively.

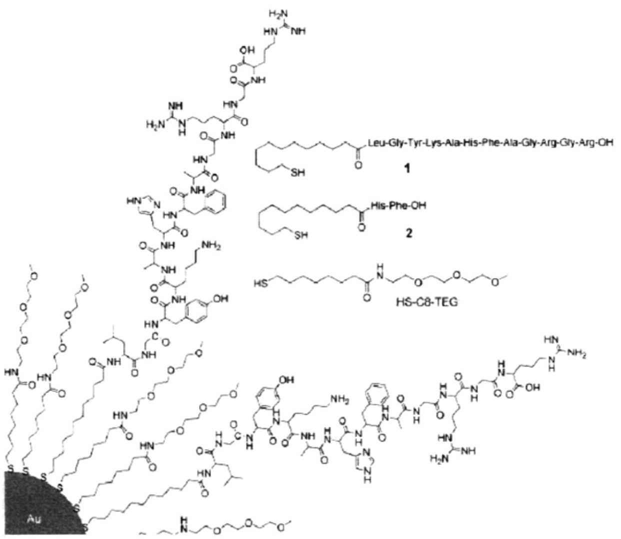

Figure 2.4.5: Schematic of ligands used in the dodeca-peptide catalysis.

1. Dodeca-peptide catalyst ligand.
2. Di-peptide catalyst ligand for comparison.
3. **Below ligand 2:** PEG terminated filler ligand.
4. **Lower left picture:** Schematic of filler and catalyst on particle.

The figure has been taken from reference [47] without permission.

The results, shown in **Figure 2.4.6**, provide additional evidence of cooperativity in the nanoparticle monolayer, and highlights how the local environment can affect the relative activity of the catalytic molecules. In this case, the tyrosine, lysine and imidazole are all buried within the monolayer and are suspected to be withdrawn from the solvent interface. This seems to increase their pKa because the anionic nature of the carboxylate prevents the deprotonation of these species. This again has the effect of producing all of the necessary machinery for ester hydrolysis (proton donors and acceptors) allowing faster catalysis.

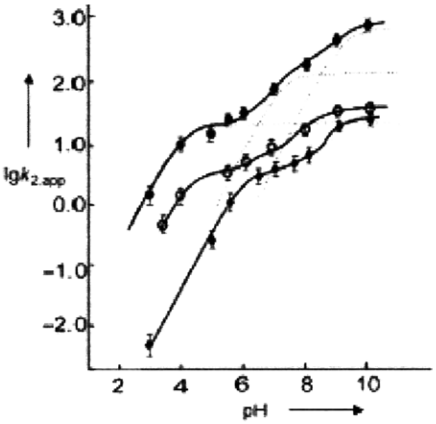

Figure 2.4.6: Catalytic rate, k^{2}_{app}, as a function of acidity. **Upper curve, large circles** – dodecapeptide catalyst with three cooperativity transitions. **Middle curve, open circles** – di-peptide catalyst with two cooperativity transitions. **Lower curve, small circles** – free form dodecapeptide ligand. The figure has been taken from reference [47] without permission.

Scrimin and co-workers have extended their nanozyme methods to another, classic enzymatic system – metal ion catalysis [44]. Most of the fundamental enzymes in biology function with metal ions, which are used for electron transfer, coordination, and organometallic reactions. Scrimin and coworkers developed a metal chelator from an aza-crown derivative, (S)-2-amino-3-[1-(1,4,7)-triazacyclononane]-propate, shown in **Figure 2.4.7**. The aza-crown is capable of capturing zinc(II) ions which can be used to coordinate to phosphate bonds and catalyze phosphate ester cleavage.

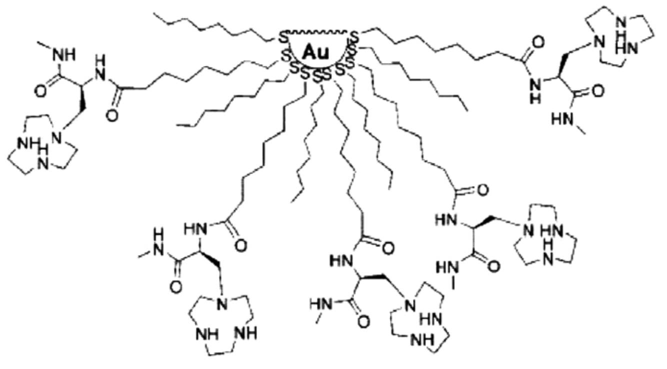

Figure 2.4.7: Schematic of zinc(II) binding catalyst system. The figure has been taken from reference [44] without permission.

When the catalytic rate for hydrolysis of 2-hydroxypropyl-p-nitrophenyl-phosphate (HPNP) was measured as a function of zinc(II) concentration (**Figure 2.4.8**), a cooperative effect was found in which increasing numbers of activated, zinc(II) bound aza-crowns caused a non-linear increase in catalysis. It should be considered that, as the amount of zinc(II) increases, the number of zinc aza-crown complexes will increase until the nanoparticles are saturated. If each zinc complex operated independently, the catalytic rate would rise linearly since each newly formed complex would add its catalytic contribution and the observed rate would be the summation of these independent rates. However, the observed sigmoid curve deviates strongly from a linear regime, the enhancement due to several zinc complexes working in synchrony. Enzymatic hydrolysis of phosphate esters is known to operate with two or three zinc centers, coordinating the oxides of the phosphate and stabilizing the attack of water onto the phosphate. The molecular detail of the catalysis mechanism in the zinc-chelate nanozymes is not yet known; however it is hypothesized to involve a simplistic form of this multiple-stabilization/activation.

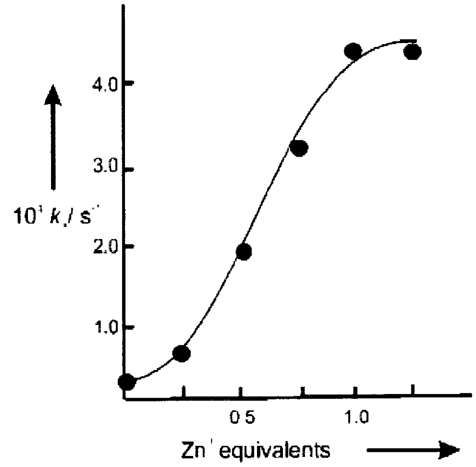

Figure 2.4.8: Catalytic rate, k_1, as function of zinc concentration. The non-linear rise in the catalysis rate suggest a cooperative behavior as multiple zinc ions are captured. The sigmoidal shape is due to the saturation of reactivity when all the aza-crown chelators have become occupied with zinc ions, thus preventing further cooperativity. The catalysis rate seen at zero zinc concentration corresponds to the background solvent's catalysis. The figure has been taken from reference [44] without permission.

An interesting variation on the nanozyme concept was developed by Rotello and co-workers [48]. In this system they produced anionic nanoparticles which attract and bind with peptide fragments. By bringing two complimentary peptide fragments together on the nanoparticle surface, they facilitated the auto-catalytic linking of the peptides via thioester formation (**Figure 2.4.9**). Although the molecular machinery for the catalytic reaction was placed on the substrates - the peptide fragments - the nanoparticle is acting as a true, catalytic platform for stabilizing and pre-organizing the reaction. This work suggests a new path for nanozymes, in which the nanoparticle facilitates the bound intermediate between the substrate(s), using its physical properties to guide catalysis rather than chemical reactivity.

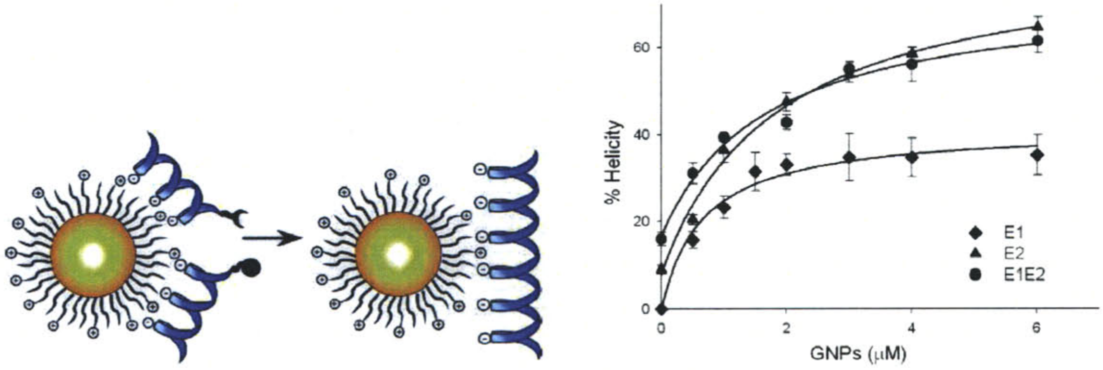

Figure 2.4.9: Left – Schematic of peptide fragments binding to anionic nanoparticle and the induced catalytic joining. **Right** – Kinetic curves of % alpha-helicity (used as a measure of product formation) as a function of gold nanoparticle, GNP, concentration. E1 and E2 are the two peptide fragments and E1E2 is the fully joined peptide. The low helicity of E1 demonstrates the instability of this peptide helix before it bonds with E2. The figures have been taken from reference [48] without permission.

These studies open a new field of catalytic systems in which monolayer-protected nanoparticles may be used to design and carry out complicated catalytic reactions. It also suggests nanoparticles can be used as a platform to study cooperative, catalytic chemistry as it applies to biological systems, in particular, the types of coordination found in enzymes.

2.5 Magnetic Supported Catalyst Nanoparticles and Metal-Complex Catalysis

The second major class of supported catalyst nanoparticles involves magnetic nanoparticles for industrial chemical processes, in particular iron oxides such as magnetite (Fe_3O_4) and maghemite (Fe_2O_3). These particles have several useful properties, the most important being their magnetism, which is generally superparamagnetism. This phenomenon occurs in nanoscale ferromagnets when the size of nanoparticle becomes smaller than the average domain size. This generates a population of spin-states which move in synchronicity to an applied field, generating a large paramagnetic response. This paramagnetism can be used to separate out the particles from a solution [49,50]. Researchers are developing these magnetic particles as supported catalyst platforms that can be used in commercial processes, where the traditional problem of separating the catalyst from the product continues to be a major technical challenge. In addition, the use of non-reactive oxides produces nanoparticles that are compatible with a wide range of organic and organometallic groups, making them capable of carrying catalysts such as amines and thiols which cannot be placed on gold or silver nanoparticles.

There is a growing body of work in magnetic supported catalysts, from which several important examples are presented here to demonstrate the scope of this monolayer catalysis. In the work of Phan and Jones, magnetite nanoparticles were functionalized via a siloxane bond with an ethylenediamine derivative and used in the Knoevengel Condensation of an aldehyde with a nucleophilic carbon center [51] (**Figure 2.5.1**). The amine groups do not react with the iron oxide core and thus do not cause aggregation of the particles. In contrast to the thiol-gold monolayers, the monolayers of magnetic particles form stronger bonds and therefore no re-arrangement or ligand exchange occurs.

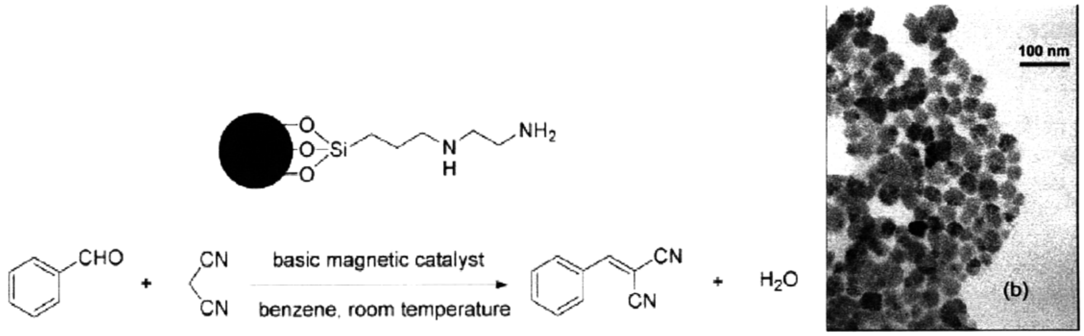

Figure 2.5.1: Left – Top Schematic of ethylenediamine derivative nanoparticle catalyst used by Phan and Jones in the, **Bottom**, Knoevengel condensation. **Right** – TEM image of nanoparticles. The figures have been taken from reference [51] without permission.

The supported catalyst demonstrated high catalytic rates, showing completion times of 30 min – 3 hr with catalyst loadings of 2.5 – 0.5 %mol respectively, as shown in **Figure 2.6.2**. When the particles were removed from the solution, no catalysis was observed. An important factor for all supported catalysts is *recyclability*, and when the particles were re-tested up to five times it was observed they could repeatedly function as catalysts [51]. It was found the particles could carry out full conversion of the substrate to product on each run after several hours, but that the rate of conversion slowed down with each retrial, suggesting decomposition of the monolayer during reaction.

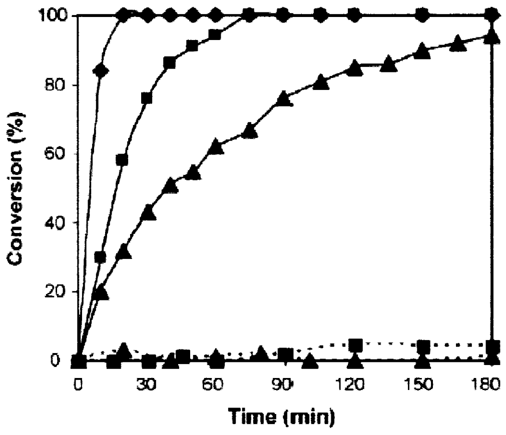

Figure 2.5.2: Kinetic curves of nanoparticles from Phan and Jones in Knoevengel condensation.

1. Upper diamonds – 2.5% mol catalyst.
2. Second squares – 1.5% mol catalyst.
3. Third triangles – 0.5% mol catalyst.
4. Lower triangles – Non-catalytic nanoparticles.
5. Lower squares – Supernatant after the extraction of nanoparticles, demonstrating that the nanoparticles are the active catalyst.

The figure has been taken from reference [51] without permission.

In similar work, Gao and co-workers produced maghemite (Fe_2O_3) particles coated in various acid-base dipeptides to evaluate their use in ester hydrolysis [52]. The system is a crossing between the gold core nanozymes described previously, which use organic molecules exclusively, and the use of magnetic cores as a means of separation from solution. A different approach uses supported metal complexes as the catalytic sites. Many of the most reactive and versatile chemical reactions, particularly in reduction-oxidation chemistry and carbon bond formation, rely on metal centers to coordinate and fuse organic molecules together. Examples include reactions such as Suzuki, Heck, Sharpless, Negishi, and the Metathesis reaction, all of which require a metal center (usually a transition metal) [53]. One idea has been to take these well established solution chemistries and support them on magnetic nanoparticles, allowing easy extraction of the catalyst from the products via an applied field [54-74].

An example of this strategy is the work of Lin and co-workers who produced a monolayer of BINAP (2,2'-bis(diphenylphosphino)-1,1'-binaphthyl) ligands which could be complexed to a ruthenium center [60] (**Figure 2.5.3**). This metallic complex was used in the enantioselective hydrogenation of aromatic ketones to alcohols. Although no kinetic data was given (a common feature of these types of studies) the conversion rates for the catalyst were high and gave enantiomeric excesses (ee) of ~ 70-95%. These particles could not be reused more than 4-10 times before they lost complete catalytic activity, a result they attribute to oxidation from the atmosphere.

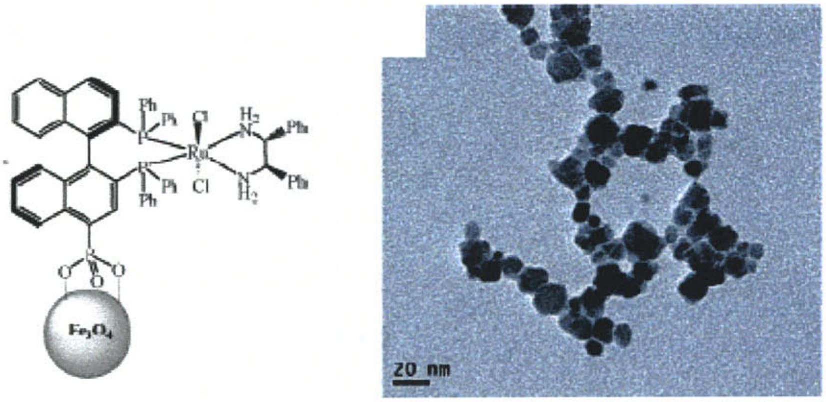

Figure 2.5.3: Left – Schematic of nanoparticles used by Lin and co-workers in the hydrogenation of aromatic ketones, demonstrating a supported metal center catalyst. **Right** – TEM image of particles. The figures have been taken from reference [60] without permission.

The work of Lin and coworkers demonstrates the use of metal complexes for straightforward, small molecule reactions. Shen and co-workers extended this to polymerization reactions in which they used a tri-amine ligand to chelate a Cu(I) ion for atom-transfer radical living polymerization (ATRP) of methyl-methacrylate [57] (**Figure 2.5.4**). Testing of the supported and free form catalyst demonstrated comparable kinetics, a major improvement over traditional surface supported ATRP catalysts which suffer from low initiation and polymerization rates.

The findings of Shen and coworkers demonstrate that the supported catalyst operates more as a homogenous system, and that the particles can be easily separated from the product solution (see **Figure 2.5.4**). The recyclablility of the particles required addition of CuBr to convert the Cu(II) oxide state to Cu(I), however this proved slow and caused a reduction in kinetic rates for rerun trials. However, this rate could be boosted by the slight addition of triethyl amine which reduces Cu(II) to Cu(I) rapidly and regenerated the supported catalysts rates to those of the as-synthesized particles. The poly-dispersity found in the polymer product matched closely with that obtained with an unsupported catalyst, and was found to improve with recycling.

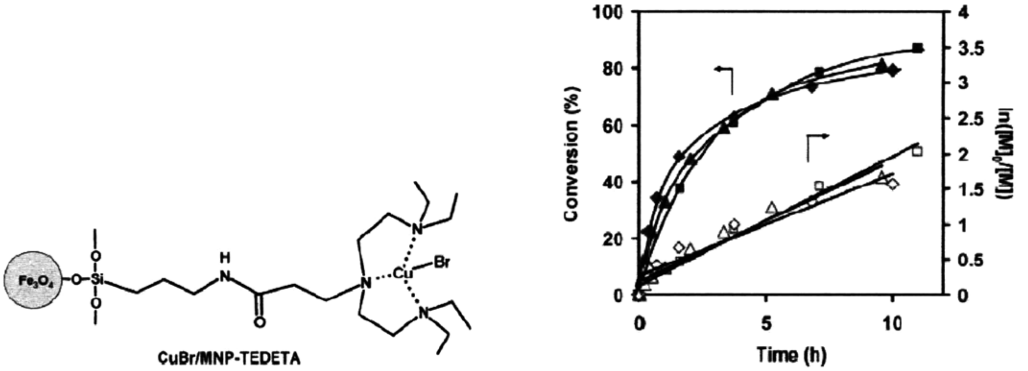

Figure 2.5.4: (Left) – Schematic of Shen and co-workers' catalytic nanoparticle demonstrating a bound metal center for living polymerization. **(Right)** – Kinetic curves of atom-transfer radical polymerization as a function of time. The dark shapes show the catalysis for the nanoparticles (squares) and free form catalysts (triangles, circles) with Cu(I). The open shapes represent the same systems without Cu(I) present. The kinetic curves demonstrate that the supported catalyst works as well as the free form catalyst. The figures have been taken from reference [57] without permission.

These examples highlight the use of metal complexes as supported catalysts on magnetic particles. As with the nanozyme examples, these particles possess monolayers that provide the catalytic sites and physical properties, of which the most important are increased solubility and homogenous mixing. These supported catalysts also introduce the notion of using both the core and the monolayer of the nanoparticle, allowing the linking of the magnetic crystal core with the supported catalyst to produce a better chemical machine.

The number of supported catalyst reactions is large; **Table 2.5.1** provides a summary of many of the examples from the literature, demonstrating the breadth of reactions being pursued on supported catalysts and suggesting the potential for these catalysts. It is seen that not only magnetic oxides but also gold particles are used for metal centers, showing how the two classes of particles describe are part of a continuum of well-matched monolayer and core chemistry.

First Author	Core	Catalyst	Reaction	References
Bartz	Au	Grubb's 1st Generation Catalyst	Ring-closing metathesis	[54]
Belser	Au	Salen-Co(III) complex	Hydrolytic kinetic resolution of Epoxides	[55]
Kisailus	Au	Imidazole, hydroxyl homo-ligand particles	Silanol hydrolysis to silicate	[61]
Lee	Au	Grubb's 2nd Generation Catalyst	Ring-closing metathesis	[62]
Li	Au	Beta-cyclodextrin-metal center	Ester hydrolysis	[75]
Li	Au	Dihydroquinidine derivative	Asymmetric dihydroxylation of olefins	[63]
Lin	Au	Pd(II) catalyst	Microwave-assisted alkyne trimerization to aromatics	[64]
Marubayashi	Au	Ti-BINOL derviative	Asymmetric alkylation	[66]
Ono	Au	Chiral bisoxazoline Derivative	Ene reaction	[67]
Gill	Co Fe_2O_4	Sulfonic acid derviative	Acetal deprotection	[58]
Yoon	Co Fe_2O_4	Rh cationic complex	Hydroformylation of olefins	[71]
Stevens	Fe_2O_3	Polymer-shell bound Pd(II) catalyst	Suzuki coupling	[68]
Zheng	Fe_2O_3	Dipeptide-Asp-His	Ester hydrolysis	[52]
Abu-Reziq	Fe_3O_4	Amine dendron with Rh Complex	Hydroformylation	[74]
Chouhan	Fe_3O_4	Click-chemistry, proline Derivative	N-arylation of N-heterocycles with aryl bromides	[56]
Dalaigh	Fe_3O_4	Pyridine derivative	Acetylation reactions	[76]
Ding	Fe_3O_4	Cu chelate derivative	Atom transfer radical polymerization of methyl methacrylate	[57]
Hu	Fe_3O_4	Ru(BINAP-PO3)(DPEN)Cl2	Enantioselective carbonyl reduction	[60]
Luo	Fe_3O_4	Quinuclidine derivative	Marita-Baylis-Hillman reaction	[65]
Lv	Fe_3O_4	Dipyridyl Pd(II) complex	Suzuki coupling	[72]
Phan	Fe_3O_4	Primary amine derivative	Knoevengel condensation	[51]
Yinghuai	Fe_3O_4	Palladium clusters	Suzuki coupling, Heck coupling	[73]
Huang	Poly-styrene	Tellurium-based, duel, organic ligands	Glutathione peroxidase	[77]

Table 2.5.1: Literature of Supported Catalysts on Nanoparticles.

The proceeding presentation of nanoparticles, nanozymes and supported catalyst nanoparticles shows a progression in complexity of nanoparticle monolayer chemistry, and in particular the development of nanoparticles as catalytic platforms. Previous literature, studies focused on the chemistry of the nanoparticle monolayer itself. I now present work that is concerned with how the *organization* of the monolayer affects the chemistry. The discovery of ripple domain nanoparticles provides a tool with which nano-scale structure can be self-assembled onto nanoparticles, and allowing me to investigate how this structure can influence catalysis. This is fundamental to understanding how the molecular environment of nanoparticles particles is operating with the substrate and catalysts, and for developing a clearer link between structure and function in nanoparticle supported catalysis.

Chapter 2 References

1. Templeton, A.C., Wuelfing, W.P. & Murray, R.W. Monolayer-Protected Cluster Molecules. *Accounts of Chemical Research* **33**, 27-36 (2000).
2. Daniel, M.C. & Astruc, D. Gold Nanoparticles: Assembly, Supramolecular Chemistry, Quantum-Size-Related Properties, and Applications Toward Biology, Catalysis, and Nanotechnology. *Chemical Review* **104**, 293-346 (2004).
3. Wang, X., Zhuang, J., Peng, Q. & Li, Y. A General Strategy for Nanocrystal Synthesis. *Nature* **437**, 121-124 (2005).
4. Bonnemann, H. & Richards, R.M. Nanoscopic Metal Particles - Synthetic Methods and Potential Applications. *European Journal of Inorganic Chemistry*, 2455-2480 (2001).
5. Love, J.C., Estroff, L.A., Kriebel, J.K., Nuzzo, R.G. & Whitesides, G.M. Self-Assembled Monolayers of Thiolates on Metals as a Form of Nanotechnology. *Chemical Review* **105**, 1103-1169 (2005).
6. Schreiber, F. Structure and Growth of Self-Assembling Monolayers. *Progress in Surface Science* **65**, 151-256 (2000).
7. Ulman, A. Formation and Structure of Self-Assembled Monolayers. *Chemical Review* **96**, 1533-1554 (1996).
8. Delamarche, E., Michel, B., Biebuyck, H.A. & Gerber, C. Golden Interfaces: The Surfaces of Self-Assembled Monolayers. *Advanced Materials* **8**, 719-729 (1996).
9. Cossaro, A. et al. X-ray Diffraction and Computation Yield the Structure of Alkanethiols on Gold(111). *Science* **321**, 943-946 (2008).
10. De-en, J., Tiago, M.L., Luo, W. & Dai, S. The "Staple" Motif: A Key to Stability of Thiolate-Protected Gold Nanoclusters. *Journal of the American Chemical Society* **130**, 2777-2779 (2008).
11. Akola, J., Walter, M., Whetten, R.L., Hakkinen, H. & Gronbeck, H. On the Structure of Thiolated-Protected Au25. *Journal of the American Chemical Society* **130**, 3756-3757 (2008).
12. Huang, W.J. et al. Coordination-Dependent Surface Atomic Contraction in Nanocrystals Revealed by Coherent Diffraction. *Nature Materials* **7**, 308-313 (2008).

13. Terrill, R.H. et al. Monolayers in Three Dimensions: NMR, SAXS, Thermal and Electron Hopping Studies of Alkanethiol Stabilized Gold Clusters. *Journal of the American Chemical Society* **117**, 12537-12548 (1995).

14. Hostetler, M.J. et al. Alkanethiolate Gold Cluster Molecules with Core Diameters from 1.5 to 5.2 nm: Core and Monolayer Properties as a Function of Core Size. *Langmuir* **14**, 17-30 (1998).

15. Ghorai, P.K. & Glotzer, S.C. Molecular Dynamics Simulation Study of Self-Assembled Monolayers of Alkanethiol Surfactants on Spherical Gold Nanoparticles. *Journal of Physical Chemistry C* **111**, 15857-15862 (2007).

16. Luedtke, W.D. & Landman, U. Structure, Dynamics, and Thermodynamics of Passivated Gold Nanocrystallites and Their Assemblies. *The Journal of Physical Chemistry* **100**, 13323-13329 (1996).

17. Luedtke, W.D. & Landman, U. Structure and Thermodynamics of Self-Assembled Monolayers on Gold Nanocrystallites. *Journal of Physical Chemistry B* **102**, 6566-6572 (1998).

18. Whetten, R.L. et al. Nanocrystal Gold Molecules. *Advanced Materials* **8**, 428-433 (1996).

19. Henz, B.J., Hawa, T. & Zachariah, M.R. Mechano-Chemical Stability of Gold Nanoparticles Coated with Alkanethiolate SAMs. *Langmuir* **24**, 773-783 (2008).

20. Heaven, M.W., Dass, A., White, P.S., Holt, K.M. & Murray, R.W. Crystal Structure of the Gold Nanoparticle [N(C8H17)4][Au25(SCH2CH2PH)18]. *Journal of the American Chemical Society* **130**, 3754-3755 (2008).

21. Mednikov, E.G. & Dahl, L.F. Crystallographically Proven Nanometer-Sized Gold Thiolate Cluster Au102(SR)44: Its Unexpected Molecular Anatomy and Resulting Stereochemical and Bonding Consequences. *Small* **4**, 534-537 (2008).

22. Zhu, M., Aikens, C.M., Hollander, F.J., Schatz, G.C. & Jin, R. Correlating the Crystal Structure of A Thiol-Protected Au25 Cluster and Optical Properties. *Journal of the American Chemical Society* **130**, 5883-5885 (2008).

23. Jadzinsky, P.D., Calero, G., Ackerson, C.J., Bushnell, D.A. & Kornberg, R.D. Structure of a Thiol Monolayer-Protected Gold Nanoparticle at 1.1 Angstrom Resolution. *Science* **318**, 430-434 (2007).

24. Dass, A., Stevenson, A., Dubay, G.R., Tracy, J.B. & Murray, R.W. Nanoparticle MALDI-TOF Mass Spectroscopy without Fragmentation: Au25(SCH2CH2Ph)18 and Mixed Monolayer Au25(SCH2CH2Ph)18-x(L)x. *Journal of the American Chemical Society* **130**, 5940-5946 (2008).

25. Sanchez, J. & Badia, A. Atomic Force Microscopy Studies of Lateral Phase Separation in Mixed Monolayers of Dipalmitoylphosphatidylcholine and Dilauroylphosphatidylcholine. *Thin Solid Films* **440**, 223-239 (2003).

26. Folkers, J.P., Laibinis, P.E. & Whitesides, G.M. Self-Assembled Monolayers of Alkanethiols on Gold: Comparisons of Monolayers Containing Mixtures of Short- and Long-Chain Constituents with CH3 and CH2OH Terminal Groups. *Langmuir* **8**, 1330-1341 (1992).
27. Sawaguchi, T., Sato, Y. & Mizutani, F. In Situ STM Imaging of Two-Component Self-Assembled Monolayers of 1-Decanethiol and 3-Mercaptopropionic Acid on Au(111). *Electrochemistry* **67**, 1178-1180 (1999).
28. Imabayashi, S., Narutoshi, G., Sasaki, T., Hobara, D. & Kakiuchi, T. Langmuir. *Langmuir* **14**, 2348-2351 (1998).
29. Smith, R.K. et al. Phase Separation within a Binary Self-Assembled Monolayer on Au{111} Driven by an Amide-Containing Alkanethiol. *Journal of Physical Chemistry B* **105**, 1119-1122 (2001).
30. Munakata, H., Kuwabata, S., Ohko, Y. & Yoneyama, H. Spatial Distribution of Domains in Binary Self-Assembled Monolayers of Thiols Having Different Lengths. *Journal of Electroanalytical Chemistry* **496**, 29-36 (2001).
31. Phong, P.H., Sokolov, V.V., Nishi, N., Yamamoto, M. & Kakiuchi, T. Concentration-Dependent Switching of the Mode of Phase Separation in Ternary Self-Assembled Monolayers of 2-Mercaptoethane Sulfonic Acid, 2-Aminoethanethiol and 1-Dodecanethiol on Au(111). *Journal of Electroanalytical Chemistry* **600**, 35-44 (2007).
32. Jackson, A.M., Myerson, J.W. & Stellacci, F. Spontaneous Assembly of Subnanometre-Ordered Domains in the Ligand Shell of Monolayer-Protected Nanoparticles. *Nature Materials* **3**, 330-336 (2004).
33. Jackson, A.M., Hu, Y., Silva, P.J. & Stellacci, F. From Homoligand- to Mixed-Ligand-Monolayer-Protected Metal Nanoparticles: A Scanning Tunneling Microscopy Investigation. *Journal of the American Chemical Society* **128**, 11135-11149 (2006).
34. Singh, C. et al. Entropy-Mediated Patterning of Surfactant-Coated Nanoparticles and Surfaces. *Physical Review Letters* **99**(2007).
35. Centrone, A., Hu, Y., Jackson, A.M., Zerbi, G. & Stellacci, F. Phase Separation on Mixed-Monolayer-Protected Metal Nanoparticles: A Study by Infrared Spectroscopy and Scanning Tunneling Microscopy. *Small* **3**, 814-817 (2007).
36. Kuna, J.J. et al. On the Role of Nanometer Structure in Interfacial Energy. *Publication in progress.*
37. Uzun, O. et al. Water-soluble Amphiphilic Gold Nanoparticles with Structured Ligand Shells. *Chemical Communications*, 196-198 (2008).
38. Carney, R.P. et al. Size Limitations for the Formation of Ordered Striped Nanoparticles. *Journal of the American Chemical Society* **130**, 798-799 (2008).

39. Verma, A. et al. Surface-Structure-Regulated Cell-Membrane Penetration by Monolayer-Protected Nanoparticles. *Nature Materials*, 1-8 (2008).

40. Centrone, A. et al. The Role of Nanostructure in the Wetting Behavior of Mixed-Monolayer-Protected Metal Nanoparticles. *Proceedings of the National Academy of Sciences* **105**, 9886-9891 (2008).

41. Pasquato, L., Pengo, P. & Scrimin, P. Nanozymes: Functional Nanoparticle-based Catalysts. *Supramolecular Chemistry* **17**, 163-171 (2005).

42. Pasquato, L., Rancan, F., Scrimin, P., Mancin, F. & Frigeri, C. N-Methylimidazole-Functionalized Gold Nanoparticles as Catalysts for Cleavage of a Carboxylic Acid Ester. *Chemical Communications*, 2253-2254 (2000).

43. Guarise, C. et al. Cooperative Nanosystems. *Journal of Peptide Science* **14**, 174-183 (2008).

44. Manea, F., Houillon, F.B., Pasquato, L. & Scrimin, P. Nanozymes: Gold-Nanoparticle-Based Transphosphorylation Catalysts. *Angewandte Chemie International Edition* **43**, 6165-6169 (2004).

45. Pasquato, L., Pengo, P. & Scrimin, P. Functional Gold Nanoparticles for Recognition and Catalysis. *Journal of Materials Chemistry* **14**, 3481-3487 (2004).

46. Pengo, P., Polizzi, S., Pasquato, L. & Scrimin, P. Carboxylate-Imiddazole Cooperativity in Dipeptide-Functionalized Gold Nanoparticles with Esterase-Like Activity. *Journal of the American Chemical Society* **127**, 1616-1617 (2005).

47. Pengo, P., Baltzer, L., Pasquato, L. & Scrimin, P. Substrate Modulation of the Activity of an Artificial Nanoesterase Made of Peptide-Functionalized Gold Nanoparticles. *Angewandte Chemie International Edition* **46**, 400-404 (2007).

48. Fillon, Y. et al. Peptide Ligation Catalyzed by Functionalized Gold Nanoparticles. *Journal of the American Chemical Society* **129**, 6676-6677 (2007).

49. Fan, J. & Gao, Y. Nanoparticle-Supported Catalysts and Catalytic Reactions-A Mini-Review. *Journal of Experimental Nanoscience* **1**, 457-475 (2006).

50. Phan, N.T.S., Gill, C.S., Nguyen, J.V., Zhang, Z.J. & Jones, C.W. Expanding the Utility of One-Pot Multistep Reaction Networks through Compartmentation and Recovery of the Catalyst. *Angewandte Chemie International Edition* **45**, 2209-2212 (2006).

51. Phan, N.T.S. & Jones, C.W. Highly Accessible Catalytic Sites on Recyclable Organosilane-Functionalized Magnetic Nanoparticles: An Alternative to Functionalized Porous Silica Catalysts. *Journal of Molecular Catalysis A: Chemical* **253**, 123-131 (2006).

52. Zheng, Y., Duanmu, C. & Gao, Y. A Magnetic Biomimetic Nanocatalyst for Cleaving Phosphoester and Carboxylic Ester Bonds under Mild Conditions. *Organic Letters* **8**, 3215-3217 (2006).

53. Negishi, E. *Organometallics in Organic Synthesis*, (Wiley, New York, 1980).

54. Bartz, M., Kuther, J., Seshadri, R. & Tremel, W. Colloid-Bound Catalysts for Ring-Opening Metathesis Polymerization: A Combination of Homogenous and Heterogenous Properties. *Angewandte Chemie International Edition* **37**, 2466-2468 (1998).

55. Belser, T. & Jacobsen, E.N. Cooperative Catalysis in the Hydrolytic Kinetic Resolution of Epoxides by Chira [(salen)Co(III)]I Complexes Immobilized on Gold Colloids. *Advanced Synthetic Catalysis* **350**, 967-971 (2008).

56. Chouhan, G., Wang, D. & Alper, H. Magnetic Nanoparticle-Supported Proline as a Recyclable and Recoverable Ligand for the CuI Catalyzed Arylation of Nitrogen Nucleophiles. *Chemical Communications*, 4809-4811 (2007).

57. Ding, S., Xing, Y., Radosz, M. & Shen, Y. Magnetic Nanoparticle Supported Catalyst for Atom Transfer Radical Polymerization. *Macromolecules* **39**, 6399-6405 (2006).

58. Gill, C.S., Price, B.A. & Jones, C.W. Sulfonic Acid-Functionalized Silica-Coated Magnetic Nanoparticle Catalysts. *Journal of Catalysis* **251**, 145-152 (2007).

59. Hara, K., Iwahashi, K., Takakusagi, S., Uosaki, K. & Sawamura, M. Contstruction of Self-Assembled Monolayer Terminated with N-Heterocyclic Carbene-Rhodium(I) Complex Moiety. *Surface Science* **601**, 5127-5132 (2007).

60. Hu, A., Yee, G.T. & Lin, W. Magnetically Recoverable Chiral Catalysts Immobilized on Magnetite Nanoparticles for Asymmetric Hydrogenation of Aromatic Ketones. *Journal of the American Chemical Society* **127**, 12486-12487 (2005).

61. Kisailus, D., Najarian, M., Weaver, J.C. & Morse, D.E. Functionalized Gold Nanoparticles Mimic Catalytic Activity of a Polysiloxane-Synthesizing Enzyme. *Advanced Materials* **17**, 1234-1239 (2005).

62. Lee, B.S., Namgoong, S.K. & Lee, S. Monolayer Protected Au Cluster (MPC)-Bound Ru-Carbene Complex: Synthesis and Its Catalytic Activity in Ring-Closing Olefin Metathesis. *Tetrahedron Letters* **46**, 4501-4503 (2005).

63. Li, H., Luk, Y.Y. & Mrksich, M. Catalytic Asymmetric Dihydroxylation by Gold Colloids Functionalized with Self-Assembled Monolayers. *Langmuir* **15**, 4957-4959 (1999).

64. Lin, Y.Y., Tsai, S.C. & Yu, S.J. Highly Efficient and Recyclable Au Nanoparticle-Supported Palladium(II) Interphase Catalysts and Microwave-Assisted Alkyne Cyclotrimerization Reactions in Ionic Liquids. *Journal of Organic Chemistry* **73**, 4920-4928 (2008).

65. Luo, S. et al. Magnetic Nanoparticle-Supported Morita-Baylis-Hillman Catalysts. *Advanced Synthetic Catalysis* **349**, 2431-2434 (2007).

66. Marubayashi, K., Takizawa, S., Kawakusu, T., Arai, T. & Sasai, H. Monolayer-Protected Au Cluster (MPC)-Supported Ti-BINOLate Complex. *Organic Letters* **5**, 4409-4412 (2003).

67. Ono, F., Kanemasa, S. & Tanaka, J. Reusable Nano-Sized Chiral Bisoxazoline Catalysts. *Tetrahedron Letters* **46**, 7623-7626 (2005).

68. Stevens, P.D., Fan, J., Gardimalla, H.M.R., Yen, M. & Gao, Y. Superparamagnetic Nanoparticle-Supported Catalysis of Suzuki Cross-Coupling Reactions. *Organic Letters* **7**, 2085-2088 (2005).

69. Takizawa, S., Patil, M.L., Marubayashi, K. & Sasai, H. Development of New Methods Toward Efficient Immobilization of Chiral Catalysts. *Tetrahedron* **63**, 6512-6528 (2007).

70. Wilton-Ely, J.D.E.T. The Surface Functionalisation of Gold Nanoparticles with Metal Complexes. *Dalton Transactions*, 25-29 (2008).

71. Yoon, T.J., Lee, W., Oh, Y.S. & Lee, J.K. Magnetic Nanoparticles as a Catalyst Vehicle for Simple and Easy Recycling. *New Journal of Chemistry* **27**, 227-229 (2003).

72. Lv, G., Mai, W., Jin, R. & Gao, L. Immobilization of Dipyridyl Complex to Magnetic Nanoparticle via Click Chemistry as a Recyclable Catalyst for Suzuki Cross-Coupling Reactions. *Synlett*, 1418-1422 (2008).

73. Yinghuai, Z. et al. Supported Ultra Small Palladium on Magnetic Nanoparticles Used as Catalysts for Suzuki Cross-Coupling and Heck Reactions. *Advanced Synthesis & Catalysis* **349**, 1917-1922 (2007).

74. Abu-Reziq, R., Alper, H., Wang, D. & Post, M.L. Metal Supported on Dendronized Magnetic Nanoparticles: Highly Selective Hydroformylation Catalysts. *Journal of the American Chemical Society* **128**, 5279-5282 (2006).

75. Li, X. et al. An Artificial Supramolecular Nanozyme Based on Beta-Cyclodextrin-Modified Gold Nanoparticles. *Catalysis Letters* (2008).

76. Dalaigh, C.O., Corr, S.A., Gun'ko, Y. & Connon, S.J. A Magnetic-Nanoparticle-Supported 4-N,N-Dialkylaminopyridine Catalyst: Excellent Reactivity Combined with Facile Catalyst Recovery and Recyclability. *Angewandte Chemie International Edition* **46**, 4329-4332 (2007).

77. Huang, X., Liu, Y., Liang, K., Tang, Y. & Liu, J. Construction of the Active Site of Glutathione Peroxidase on Polymer-Based Nanoparticles. *Biomacromolecules* **9**, 1467-1473 (2008).

CHAPTER 3 - THE HYPOTHESIS AND RESULTS

Hypothesis

For my thesis I propose the following hypothesis:

Ripple domain nanoparticles can be used to generate a local molecular structure that can modulate a catalyst embedded in the monolayer. Observation of catalysis as a function of ripple domain structure should show a non-linear pattern of enhanced or attenuated catalysis when compared to a non-ripple nanoparticle.

Several details of this hypothesis must be elaborated. First I make clear that the ripple domain is a structure, a morphology, in which two ligands can be arranged. The structure itself is not the catalysis, insofar that it does not directly react chemically with the substrate. Instead, I consider that the ripple domain structure affects the physical environment of the catalyst and therefore alters its chemistry. This alternation of the physical environment can be either through (1) a physical mechanism in which the geometry of the solvent-substrate-monolayer affects the positioning of atomic structure and electron density necessary for the reaction to proceed, or (2) by changing the local polarity of the environment around the catalysis-substrate, thus affecting the electron states of the molecules and their concomitant reactivity. These mechanisms are based on the theory developed in explanation of the ripple nanoparticle surface energy study [1]. In these statements I join together the concept of local structure in catalytic chemistry with the structure in monolayer protected nanoparticles.

How to compare catalysis between different particles? Required is a quantitative measure that can be compared between the ripple domain and non-ripple domain particles. The two major quantities that describe a catalytic reaction are the catalysis rate, k_{cat}, and the efficiency, η (see *Appendix A* for details). The catalysis rate describes how fast the catalyst can transform a substrate molecule into a final product, where a faster rate implies product is generated in a shorter time. Efficiency describes how well the catalyst performs the reaction depending on the substrate concentration. Highly efficient catalysts produce the final product rapidly even with low concentrations of substrate. Both of these quantities can be obtained from basic kinetic data and therefore both can be used to quantify and compare the ripple and non-ripple nanoparticles. What is central to the thesis is that if the structure of the ripple domain changes the catalysis I expect changes in the catalytic rate and/or efficiency, and by quantifying these values I can test if the ripple domain modulates non-linearly catalysis compared to a non-ripple nanoparticle.

To test the hypothesis that ripple domain nanoparticles can improve a catalytic reaction, a series of ripple domain nanoparticles was synthesized using the imidazole terminated alkanethiol 11-(1N imidazo)-undecane-1-thiol (referred to as IT) as the catalyst, in combination with an aliphatic, non-reactive filler ligand. A series consists of batches of ripple particles, each batch of a specific ratio of the two ligands (e.g. 2:1 (33% catalyst), 1:1 (50% catalyst), 1:2, etc.). Homo-ligand nanoparticles composed completely of either the catalyst ligand or filler ligand were used as non-ripple nanoparticle references against which to compare modulation in the catalysis chemistry. The ratios selected for the ripple domain particles were taken based on ratios known to produce ripples in other ligand systems.

Although I could use flat SAM ripple domains the use of nanoparticles is favored. Currently there is no easy way to control reproducibility of the formation or size of ripple domains on flat substrates. Exacerbating this is the inability to control the composition of the two ligands in the ripple domain. In contrast, the ripple domain can be generated easily with nanoparticles in large quantities which produce an effective total area much larger than could be achieved practically on a flat surface. Furthermore, nanoparticle solubility allows us the opportunity to work in solution (termed *homogeneous catalysis*), improving the ability to transport potential substrates to the particles and offering a wider range of possible reactions to explore.

Overview of Experimental Work

Following the procedure of Scrimin and coworkers [2], ripple domain particles were tested in a hydrolysis reaction in which 2,4-dinitrophenyl acetate (DNPA), an ester, is split into its constituent carboxylic acid (acetic acid, AcOH) and hydroxyl group (2,4-dinitrophenol (DNP-OH)). The imidazole acts as a general acid/base catalyst by mediating proton transfer between the water and ester. The necessity of water as a reagent required all reactions to be carried out in aqueous solutions. To obtain the catalysis rate, a solution is made of nanoparticles, an appropriate buffer to control the pH, and the DNPA substrate. The buffer is present to prevent the imidazole from becoming protonated permanently; as an ion the imidazole cannot act as a catalyst. It is important to keep the amount of catalyst used in each measurement, and between particles, equal so that changes in catalyst amount do not swamp out or distort effects due to the monolayer morphology. Therefore all nanoparticles are run with the same catalyst concentration, $\langle cat \rangle$; however, because of differences in particle sizes and the fact that I am varying the catalyst content across the ripple particles and non-ripple homo-ligand particles this means that each measurement was run with *different amounts of nanoparticles*.

The DNPA molecule absorbs visible light at 400 nm, and as it is hydrolyzed to DNP-OH its absorption increases. Using an ultraviolet-visible spectrometer (UV-Vis) I monitored the catalyzed hydrolysis of the DNPA in solution by the nanoparticles. The resulting change in absorbance as a function of time produces the kinetic curve which can be fit with a computer to the rate formula to obtain the catalysis rate k_{cat}. The kinetic curve approaches asymptotically a saturation absorbance which is equal to the full hydrolysis of the DNPA concentration. To verify that this saturation absorbance corresponds to the actual product concentration, sodium hydroxide base can be used to fully hydrolyze the DNPA and the corresponding value compared to the kinetic curve maximum.

Three filler ligands were used in the experiments: 1-octanethiol (OT), 1-hexadecanethiol (HD), and 16-mercapto-hexadeca-1-oic acid (MHA). OT and HD are aliphatic, methyl terminated ligands which exhibit an oil-like monolayer and are soluble in organic medium. MHA is an aliphatic, carboxylic terminated ligand which exhibits a polar / charged monolayer and is soluble in water and highly polar organic medium. HD and MHA are homologous in their length and differ only by their terminal functional groups. OT and HD are respectively 8 (8.8 Å) and 16 (18.9 Å) methylene $-CH_2-$ units long, and differ from the catalytic IT ligand by, respectively, -3 (-2.5 Å) and +5 (+5.0 Å) methylenes. In all of these comparisons of dimensions it must be emphasized that this is for ligands fully extended; within the monolayer the ligands can relax somewhat due to the conformational freedom of their head groups. As was stated, the ripple domain forms a gap between the longer and shorter ligands. In an OT:IT ripple domain, the IT ligand extends above the OT ligand and thus is presented as the "ridges" of the gap, whereas in the HD:IT ripple domain the IT is buried within the gap formed by the longer HD ligands. These morphologies allowed testing if the position of the catalyst within the monolayer would affect the catalytic rate.

The OT:IT and HD:IT systems were run in a 3:2 ethanol:water mixture; however, during the course of the work it was found that the poor solubility of the OT and HD systems (10-100 nM nanoparticles) combined with their low reaction speed (1-2 days to complete hydrolysis) made it difficult to obtain data. To improve the situation, the MHA:IT system was developed such that all reactions could be run in pure water. Although MHA-IT particles have the same solubility in water as OT:HD:IT particles, the fact that water is in high excess improves the reaction speed to a few hours, allowing more measurements and thus greater resolution in the data.

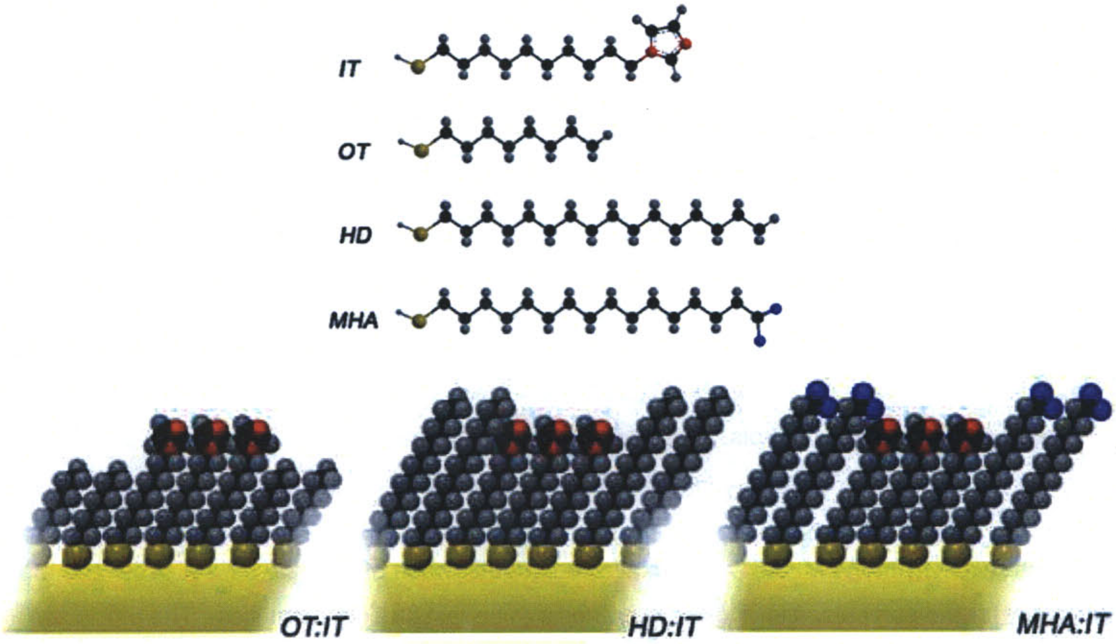

Figure 1: (Top) Schematic structures of the alkanethiol ligands used in this study. **Catalyst ligand – IT** - 11-(1N imidazo)-undeca-1-thiol, with the imidazole group that is the catalytic site used for general acid/base catalysis. **Filler ligands – OT** – 1-octanethiol, **HD** – 1-hexadecanethiol, **MHA** – 16-mercapto-hexadeca-1-oic acid. The models show the relative sizes of the ligands. Color code – C (black), H (gray), S (yellow), N (red), O (blue). **(Bottom)** Schematic models showing the relative lengths of the catalyst ligand to filler ligands in the ripple domain monolayer on a gold surface. For the OT:IT system the catalyst extends above the filler monolayer, whereas for the HD:IT and MHA:IT systems the catalyst is embedded below. The models are not intended to display actual height differences.

As controls, catalysis was run (1) without any nanoparticles to obtain the background rate due to the solvent, (2) with the free form IT ligand and (3) with solutions of nanoparticles in which the nanoparticles themselves are extracted out with a filter and the remaining supernatant solution used (termed *extracted trial*). This third control is to ensure that no contaminate present in the nanoparticle solutions is responsible for the observed catalysis. The free form IT ligand could not be tested in pure water due to its insolubility. A summary of the experiments is provided in **Table 1**.

Series	***OT-HD-IT***	***MHA-IT***
Ripple Domain	*OT:IT 1:1*	*MHA:IT 2:1*
	OT:IT 1:2	*MHA:IT 1:1*
	OT:IT 1:3	*MHA:IT 1:2*
	HD:IT 1:1	
Non-Rippled	*IT*	*IT*
		MHA
Controls	*No particles*	*No particles*
	Molc. IT	*Extracted*
	Extracted	

Table 1: Summary for each system of ligands those particle types that are ripple and non-ripple and the experimental controls. The hypothesis test is if the catalytic rate of ripple particles improves over non-ripple.

The high reactivity of the MHA:IT system allowed quantification of both the catalytic rate and the efficiency for the particles, allowing the hypothesis to be test by both quantities. The efficiency required the measurement of the binding constant, K, as found in the Michaelis-Menten formulation of catalysis (see *Appendix A* for details). The binding constant is obtained by measuring how the catalytic rate changes as a function of substrate concentration. In considering the catalytic rate, the binding constant and efficiency quantify the *kinetics* of the catalysis, which deals with the time scales of the reaction but says nothing of the *thermodynamics* of the chemistry. All catalytic reactions require surmounting an energy barrier, and thus have extended the hypothesis to consider what effect the ripple domain particles would have on the energy barrier itself (see *Appendix A* for details). Therefore the thermodynamic parameters of the activation energy of the catalytic reaction and the attempt frequency were measured for the MHA-IT system; this was done by measuring the catalytic rate as a function of temperature. Observing changes in the activation energy and attempt frequency between the ripple nanoparticles and homo-ligand particles therefore allowed a third test of the hypothesis.

Results

The following results are presented in a more topical and less chronological order. Chronologically the OT-IT and HD-IT systems were developed first, followed later by MHA-IT when it was apparent that OT, HD demonstrated low catalytic rates. In the following results, the ratio of ligands for a given particle batch are given by their synthetic (ideal) ratios, but it must be pointed out that this is not the real ratio (e.g. a 2:1 OT:IT sample is ideally 33% catalyst ligand but is not the measured value).

3.1 Nanoparticle Synthesis and Purification

All nanoparticles were synthesized by the one-phase, ethanol solvent based method as previously described. For a given series of particles (e.g. OT:IT or MHA:IT), all of the samples were prepared in the same time frame (one day to a week) in order to provide experimental consistency, as described in **Table 3.1.1**. Due to the cost of the IT ligand, each batch of particles synthesized was scaled from 50-80% of the original recipe used in-house; no apparent difference in yield or quality was observed due to this modification. Each ripple domain system allowed for only a certain series of filler:catalyst ratios due to insolubility in the reaction medium, as shown in **Table 3.1.1**. OT:IT and HD:IT particles could not be synthesized with filler ratios (OT, HD) greater than 50% due to their incompatibility in ethanol / water. MHA-IT is soluble in water through the entire range of ratios and therefore the entire range, from homo-ligand to ripple domain, could be tested.

OT:IT, HD:IT Particles

Synthesis 1	***Synthesis 2***	***Ideal %mol Catalyst***
OT:IT 1:1	OT:IT 1:1 (3)	50%
OT:IT 1:2	OT:IT 1:2 (3)	67%
OT:IT 1:3	OT:IT 1:3 (3)	75%
IT (1)	IT (3)	100%
HD:IT 1:1		50%

MHA:IT Particles

Synthesis 1	***Synthesis 2***	***Ideal %mol Catalyst***
MHA		0%
MHA:IT 2:1	MHA:IT 2:1 (2)	33%
MHA:IT 1:1	MHA:IT 1:1 (2)	50%
MHA:IT 1:2	MHA:IT 1:2 (2)	67%
IT (4)	IT (5)	100%

Table 3.1.1: Particle batches and their series (syntheses) used in this study. Each batch shows the ideal catalyst ratio, used in synthesis. For the particle syntheses the time span for each series' synthesis is given as:

- OT:IT synthesis 1 – one week
- OT:IT synthesis 2 – one day
- MHA:IT synthesis 1 – one week
- MHA:IT synthesis 2 – one day

The as-synthesized MHA:IT particles precipitate rapidly out of the ethanol reaction solution due to their acquiring of a negative charge during synthesis, however the OT:IT and HD:IT particles, especially at higher loadings of catalytic IT, proved highly soluble in ethanol. To precipitate these particles required the addition of toluene and precipitation overnight at ~ 4^0C.

It was observed early on that the catalyst ligand particles behaved differently than typical particles previously synthesized in my group. Typically particles can be filtered through a quantitative fiber paper and collected as solids. However, for any of the particles synthesized with the IT catalyst ligand, when the particles are dried they cannot be re-dissolved back into solution, even with stirring, ultra-sonication, or heating. Currently there is no answer for this behavior, and its exploration is not the purpose of this thesis; however it is conjectured the problem lies in two possibilities: (1) the formation of a strong complex between the imidazole moieties when compacted together during drying, or (2) the presence of a contaminate that weakens the thiol/gold interface and causes monolayer degradation and subsequent aggregation. It is noted that the MHA:IT nanoparticles can be re-dissolved in water after drying, but that the amount that re-dissolves diminishes with each drying cycle. A new method for handling the particles was developed using ultra-centrifugation. To collect and handle particles, batches were reduced down to concentrates and centrifuged at 3 – 5 kRPM to precipitate into pellets. The solvent could be removed without disrupting these pellets, and the pellets themselves could be re-dissolved with stirring or ultra-sonication, but could not be dried completely.

When synthesized, nanoparticles must be separated from the remaining, free-form ligands and any salts or organic by-products generated during the reaction; the removal of these unwanted molecules is called *purification*. Typically purification is done by precipitating the particles, drying them into a solid powder, and washing the powder with solvents that selectively carry away the ligands and salts; however the inability to dry the catalysts particles prevented using this method. To purify the catalysts nanoparticles, each batch was precipitated with either ethanol or toluene, and then re-centrifuged several times in ethanol and water to remove excess ligand and borate salts, respectively. Washing with water proved very delicate, due to transformation of the flocculated particles into a slime that clung to the centrifuge tube – requiring careful extraction of the supernatant to prevent loss of material. MHA:IT particles could not be washed with water and so were washed only with ethanol extensively (8x -10x).

For the OT:IT system three synthetic series were prepared to test the reproducibility of the catalysis rate. However, one of these syntheses produced particles that were highly insoluble and gave poor catalytic responses. Upon checking the reagents used in the synthesis, it was found that the IT catalyst ligand used differed from the other batches. This ligand did not crystallize at ~ 4 ^{0}C as was observed with the other samples, and it formed a turbid solution in ethanol implying it did not dissolve well, suggesting the sample is pure IT and contains some contaminate that is more hydrophobic (apolar). NMR of this ligand showed no structural difference from the other samples used but showed a discrepancy in the amount of aliphatic hydrogens present compared to the imidazole, suggesting that alkanethiols with no imidazole group were present in the sample. This data prompted the disregarding of this synthesis so only two synthetic series of OT:IT were tested.

It was determined during the experiments that the IT catalyst ligand can form a nitrogen-boron complex with the borate esters that are generated during synthesis. This unforeseen consequence was determined when testing a different type of catalytic chemistry on the OT-IT particles. Literature of organonitrogen chemistry suggested that acid hydrolysis could break these types of complexes, especially for the moderately bound imidazol-borate complex [3,4]. Samples of homo-ligand IT were hydrolyzed in either aqueous acetic acid or 2-(N-morpholino)-ethanesulfonic acid (MES). Both particles had increased solubility and stability in water and ethanol. The catalytic rates from these two types of hydrolyzed samples differed extremely; the acetic acid sample having a greatly increased rate over unhydrolyzed IT, whereas the MES sample had no catalytic reactivity (see **Figure 3.1.1**). NMR of the decomposed particle samples shows that the MES hydrolysis disrupted the imidazole due to the disappearance of the imidazole methylene hydrogen singlets . The MES hydrolyzed particles were not destroyed because of the continuance of their plasmon and the direct imaging under TEM. The evidence from the IT hydrolysis suggested the ripple nanoparticles suffered from the same borate problem. A test was made with the acetic acid hydrolysis of a MHA:IT series, followed by testing their catalytic hydrolysis. No significant difference was observed in these particles catalytic rate.

From the difficulty with the borate and the required processing of the homo-ligand catalyst particles the question arises whether a legitimate test of the hypothesis can be made. The homo-ligand particles are the reference (non-ripple) particle against which I compare the ripple domain particles. The homo-ligand monolayer has only one type of ordering, the close-packed alkanethiol lattice; there are no "secondary" orderings such as in the ripple domain gaps. In using the acid hydrolysis I do not expect to be disrupting the monolayer's packing, and the observation that the particles do not aggregate or dissolve after hydrolysis is evidence the monolayer has not been destroyed. In my testing of the hypothesis, I am concerned only with catalyst that exists in a ripple domain environment or in a normal, close-packed monolayer. Therefore, so long as the homo-ligand catalysts are active, I can make a valid comparison between the treated homo-ligand and the ripple nanoparticles.

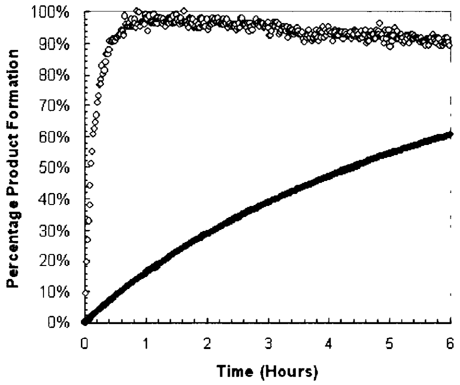

Figure 3.1.1: Kinetic curves of acetic acid hydrolyzed catalyst IT particles (open circles) and MES hydrolyzed catalyst IT particles (closed circles), demonstrating the loss of catalytic activity in the MES particles. The MES kinetic curve is equal to the background water catalytic rate.

3.2 Solubility and Stability of Nanoparticles

All particles display some degree of precipitation over time when stored over two months in a liquid medium (OT-IT in ethanol, HD-IT in chloroform or MHA-IT in water) as seen in a thin film of precipitation in the storage vile. To quantify the solubility, particles of each ligand ratio were centrifuged in buffered solution and the difference in their concentration before and after were compared (**Figure 3.2.1**). All concentrations were set at the same nanoparticle concentration, and changes due to centrifugation were interpreted as a measure of solubility. The most significant observation is particle ratios that were the least soluble tended to exhibit a higher catalytic rate. The centrifugation solubility reproduced between batches roughly.

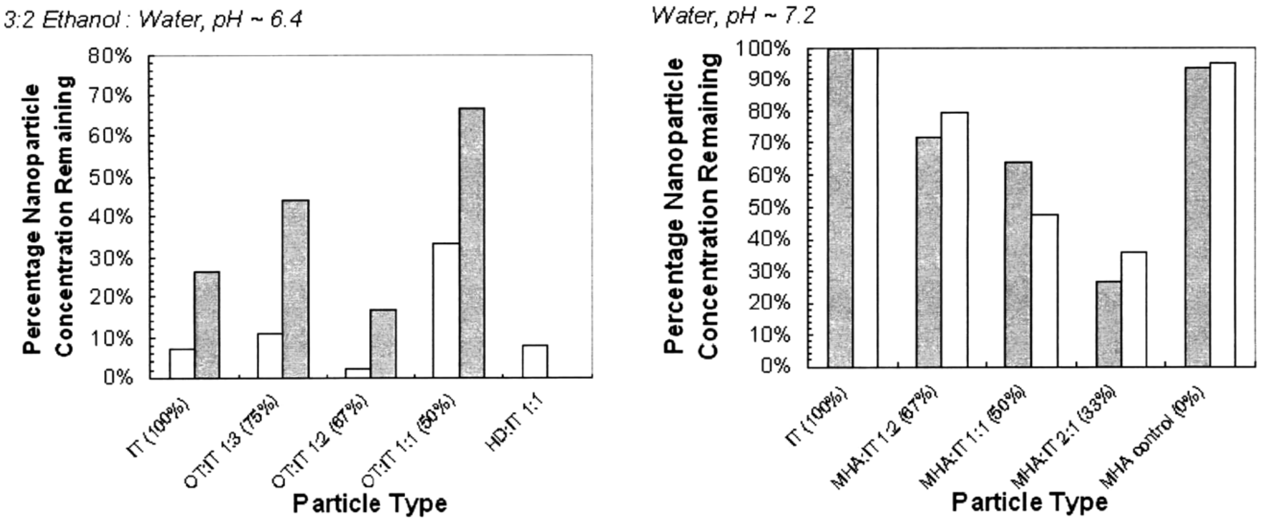

Figure 3.2.1: Centrifuge solubility for the particle syntheses as function of ligand ratio for the OT:HD:IT system **(Left)** and MHA:IT system **(Right)**. White columns denote synthesis 1 particles, gray columns synthesis 2.

OT-IT and HD-IT particles could be dissolved readily in organic medium such as chloroform and dichloromethane, and poorly in ethanol. MHA-IT could only be dissolved readily in water. MHA-IT particles would flocculate if introduced directly into pure Millipore^{TM} water (pH ~ 7.1); only water buffered above ~ 7.2 pH could be used.

3.3 Material Analysis of Particles

It was necessary to known the concentration of catalyst present to prepare equal concentration solutions and make comparisons of the rates. This was done by quantifying the size distribution of particles (done with transmission electron microscopy – TEM), the amount of organic ligand present (done with thermal gravimetric analysis – TGA), and the ratio of the catalyst ligand to the filler ligand (done with several methods described within). Knowing the particle distribution allows calculation of the concentration, which can be combined with the average amount of catalytic ligand on the particles to give the concentration of catalyst present per population of particles.

For TGA two assumptions were made for analysis – the amount of material decomposed below 600 ^{0}C represented the organic monolayer shell, and the amount of material remaining after 600^{0}C represented the inorganic metal core[2]. TGA of each particle series demonstrated the trend that the percentage of organic material decreased as the ratio of catalytic IT ligand increased, as

---

[2] In this text, all major assumptions used in the work are highlighted in red.

seen in **Figure 3.3.1**. Only one series, the reproduction series OT-IT synthesis 2, did not follow this trend (**Figure 3.3.2**). All TGA scans revealed a two stage transition (see **Figure 3.3.1**) the first between 200-300 ^{0}C, and the second between 300-500 ^{0}C. The percentage of organic did not exceed ~ 45%.

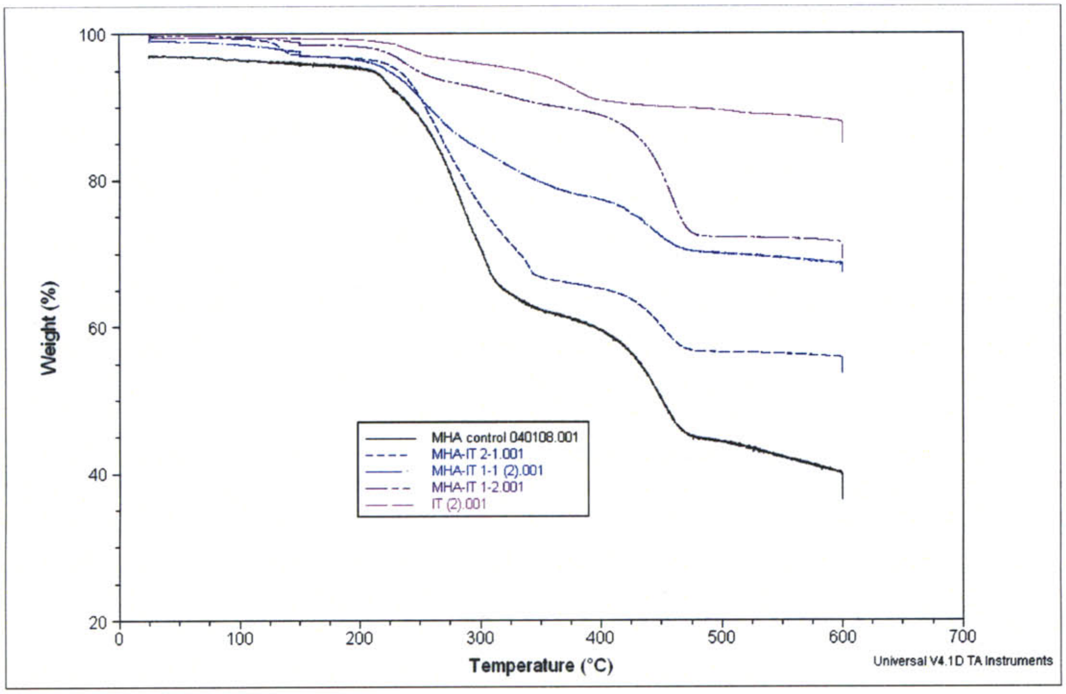

Figure 3.3.1: Example of TGA signal for the MHA-IT synthesis 1, demonstrating the observed trend that higher catalyst loading yields lower organic portion.

TEM analysis of the particles demonstrated the presence of particles and gave indication of their dispersity. In general there is very little consistency in the particle size distributions, mean, or standard deviation, both for a series of particles and inter-batch series. Following an analysis of variance, there is 99% confidence that the OT:HD:IT particles differ in the population mean for particle diameter between syntheses 1 and 2, and 59% confidence that the MHA:IT particles differ. The MHA:IT particles therefore have a slightly better consistency in particle diameter between syntheses, but only marginally. Examination of the particle distributions reveal that the resolution of the TEM pictures and the subsequent analysis tend to cut off the smaller diameter particles and therefore each distribution was fit to a log normal distribution to obtain the statistics. In only one batch (MHA:IT 1:1 Synthesis 1) could a log normal not be fit due to a bimodal distribution of particle sizes.

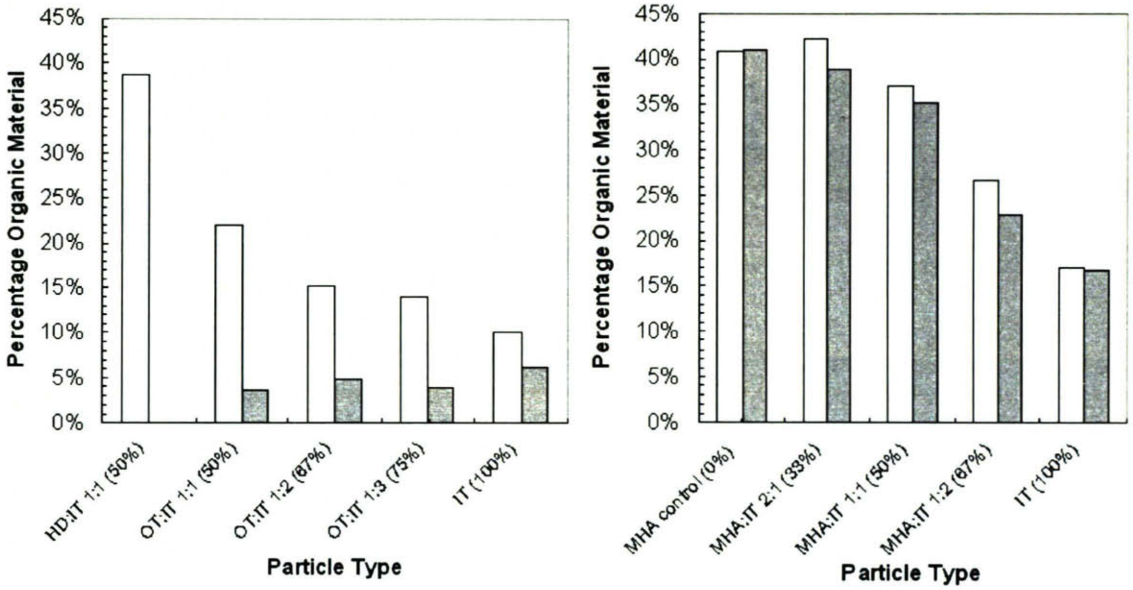

Figure 3.3.2: Experimentally determined organic portion for the nanoparticle series as a function of ligand ratio for the OT:HD:IT system **(Left)** and MHA:IT system **(Right)**. White columns denote synthesis 1 particles, gray columns synthesis 2.

To quantify the average ratio of the ligands in the monolayer different methods were applied (summarized in **Figure 3.3.4** and **3.3.5**) with each suited to the type of ligand system used. The amount of ligand used in the synthesis was carefully quantified, but it cannot be assumed that this synthetic ratio, SYN (the ideal ratio), is the same on the particles once formed. For the OT-IT and HD-IT systems NMR spectra were taken of the intact particles and of a solution made from the liberated ligands of particles that had been decomposed with excess iodine. This is the decomposition, DCP, ratio.

For MHA-IT the solubility mismatch in the ligands prevented the decomposition method from being deployed. An alternative method was used in which the supernatants of the pre and post-synthesis reaction solution were taken and any excess particles removed. These supernatants were purified nanopaticles, analyzed by NMR, and compared. It was considered that if the ratio of ligands changed from the pre and post solutions, this would be indirect evidence that the ratio of ligands on the particles was not the same as in solution, since any change in the balance of ligands in solution would be reversely matched on the particles. This analysis assumes that the ligands are perfectly soluble and partition only onto the particles or into solution. This assumption is considered valid due to the large excess of solvent compared to the ligand concentrations. The supernatant analysis gives the post-synthesis supernatant ratio of ligands, PSS. Finally, MHA-IT particle samples for the 1:2 and 1:1 MHA:IT ligand ratios were analyzed by elemental analysis, EA.

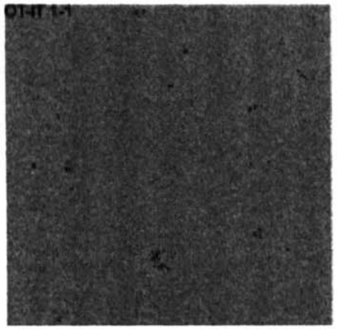

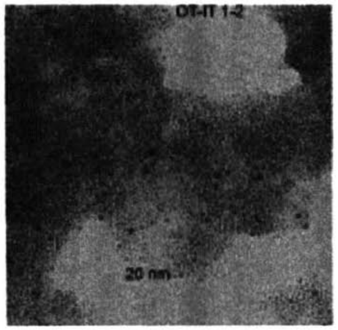

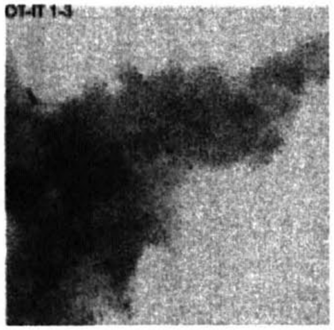

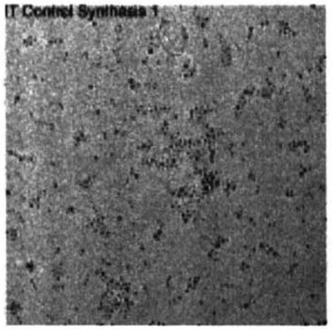

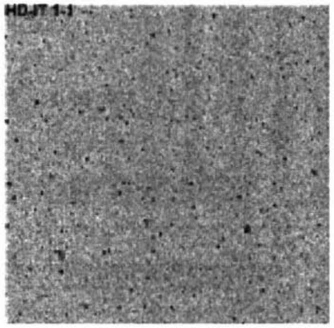

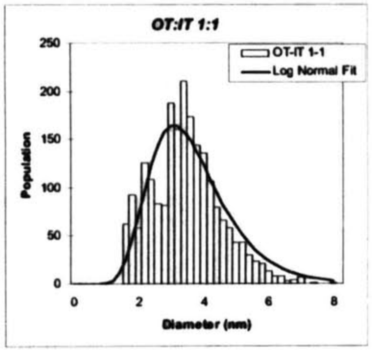

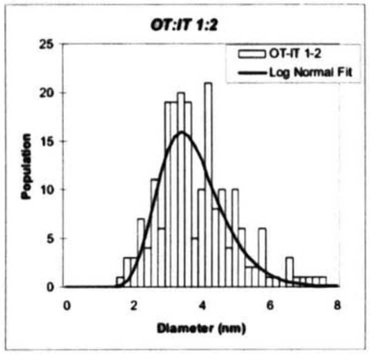

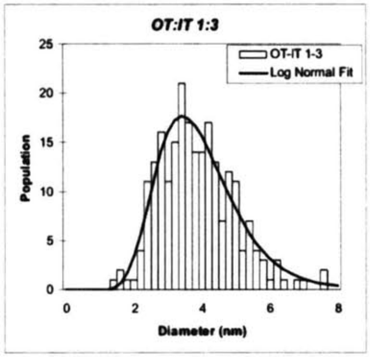

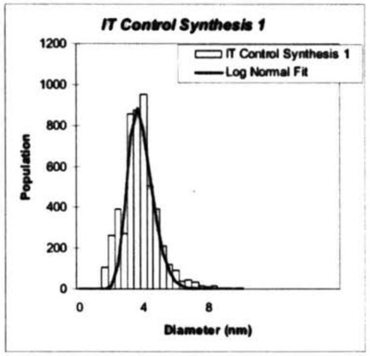

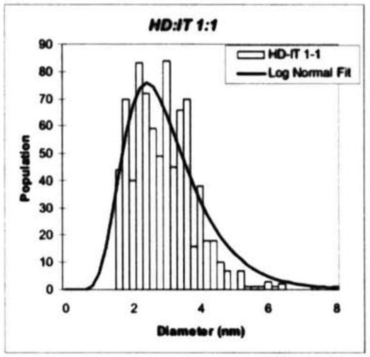

OT-IT Synthesis 1

	OT-IT 1-1	*OT-IT 1-2*	*OT-IT 1-3*	*IT*	*HD-IT 1-1*
Mean dia. - μ (nm)	3.67	3.75	3.94	3.84	3.03
Deviation dia. - σ (nm)	1.28	0.96	1.22	0.79	1.24
Particles Measured	2,144	206	228	5,205	807

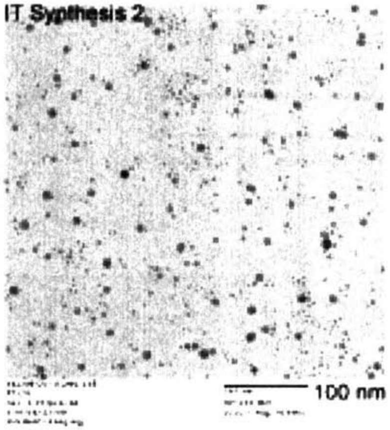

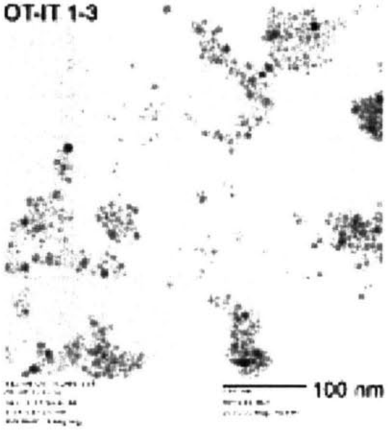

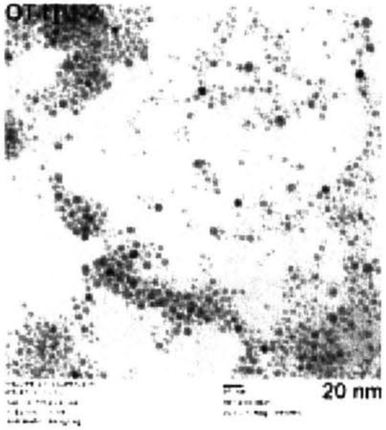

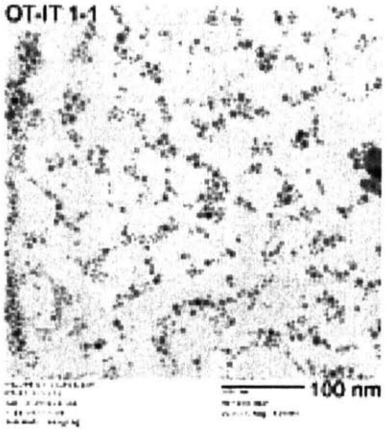

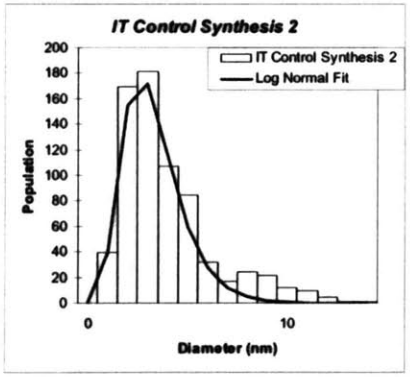
IT Control Synthesis 2

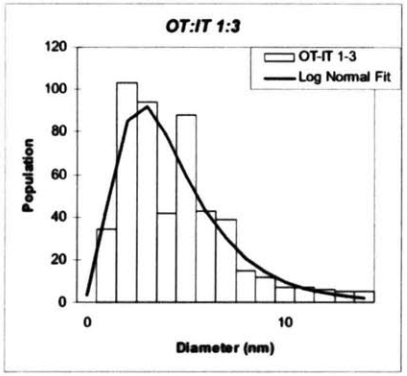
OT:IT 1:3

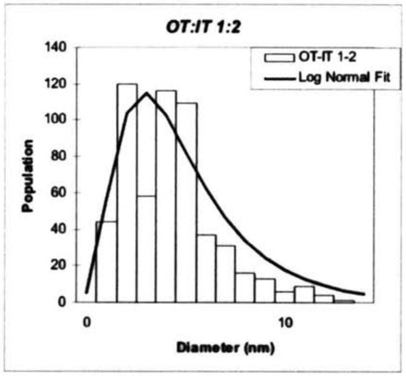
OT:IT 1:2

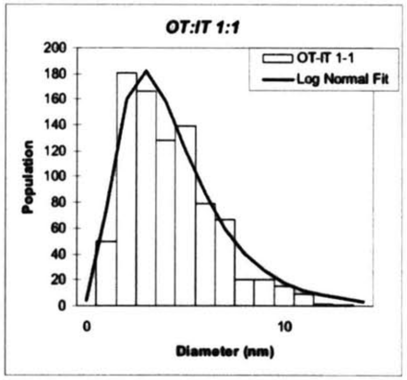
OT:IT 1:1

OT-IT Synthesis 2

	OT-IT 1-1	*OT-IT 1-2*	*OT-IT 1-3*	*IT*
Mean dia. - μ (nm)	5.51	5.98	5.49	4.30
Deviation dia. - σ (nm)	2.85	3.50	3.01	1.51
Particles Measured	877	564	495	701

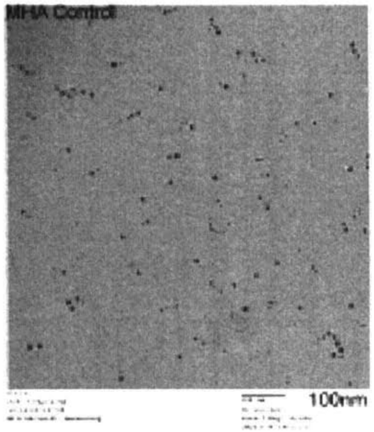

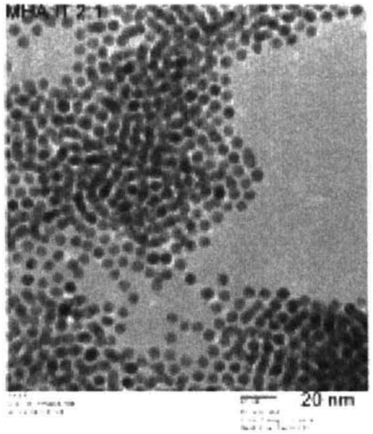

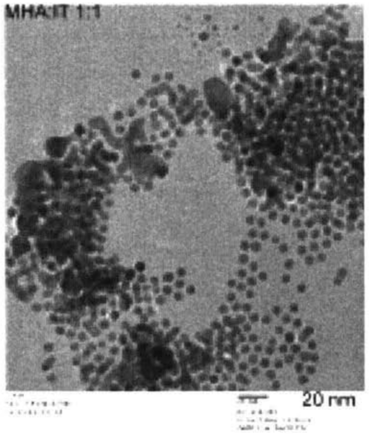

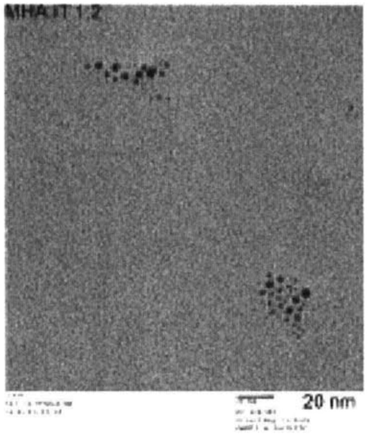

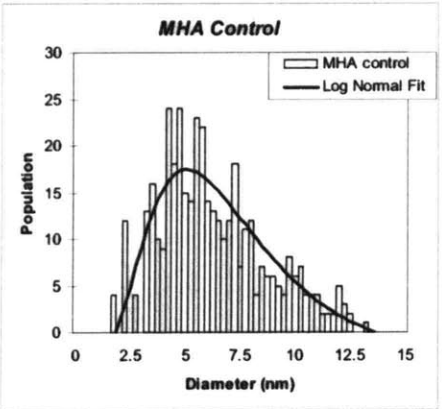

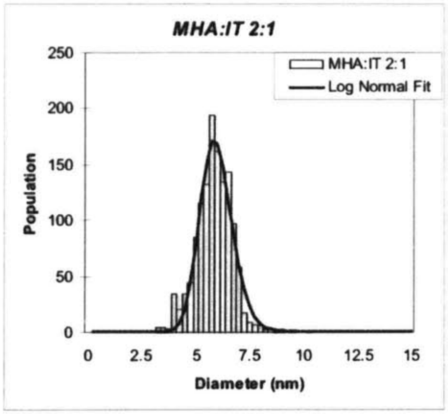

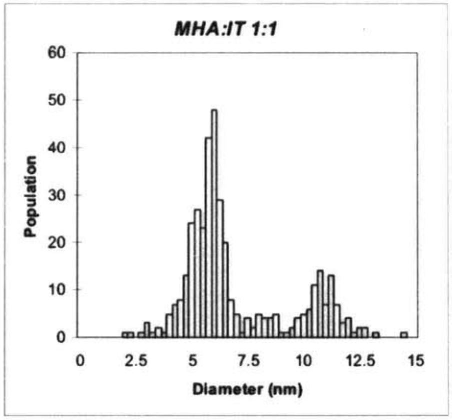

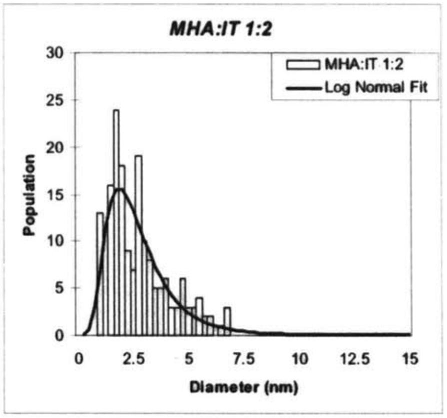

MHA-IT Synthesis 1

	MHA control	*MHA:IT 2:1*	*MHA:IT 1:1*	*MHA:IT 1:2*
Mean dia. - μ (nm)	7.56	5.97	6.88	2.75
Deviation dia. - σ (nm)	4.20	0.74	2.02	1.48
Particles Measured	399	1,318	379	170

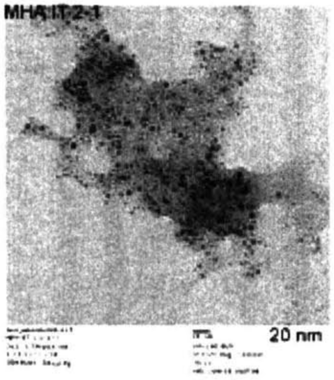

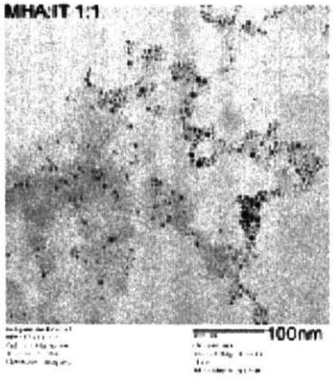

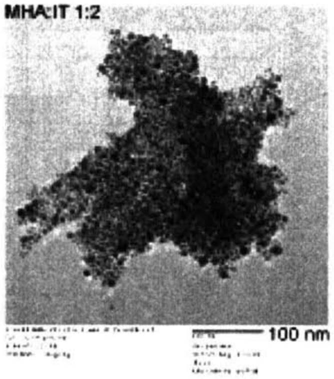

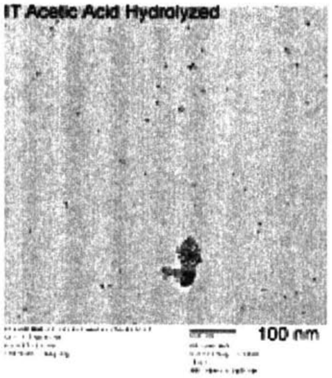

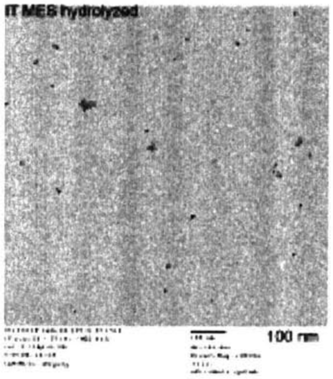

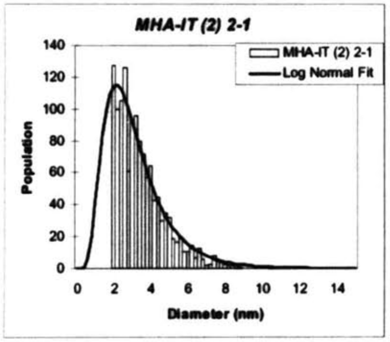

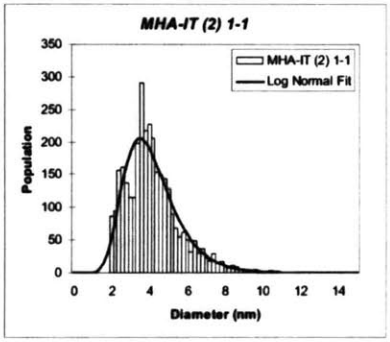

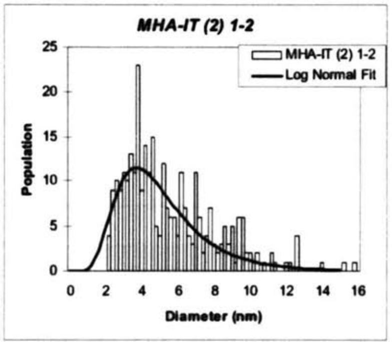

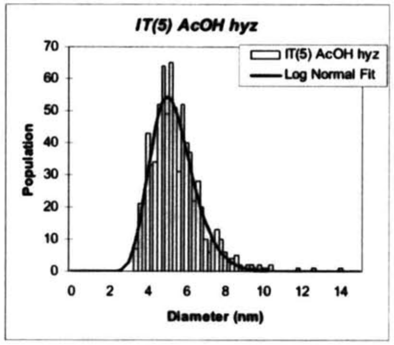

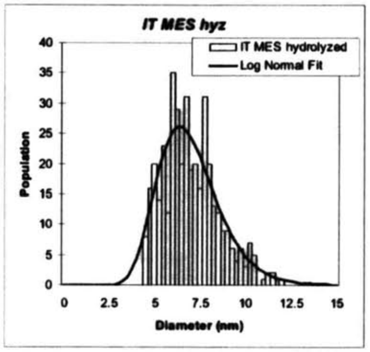

MHA-IT Synthesis 2

	MHA:IT 2:1	*MHA:IT 1:1*	*MHA:IT 1:2*	*IT AcOH hyz*	*IT MES hyz*
Mean dia. - μ (nm)	3.16	4.17	5.11	5.35	6.97
Deviation dia. - σ (nm)	1.76	1.46	2.50	1.14	1.74
Particles Measured	1,322	3,219	302	755	395

	SYN	***DCP***
HD:IT 1:1	*50%*	*55%*
OT:IT 1:1	*50%*	*63%*
OT:IT 1:2	*67%*	*78%*
OT:IT 1:3	*75%*	*84%*
IT	*100%*	*100%*

	SYN	***PSS***	***EA***
MHA	*0%*	*0%*	*NT*
MHA:IT 2:1	*33%*	*26%*	*NT*
MHA:IT 1:1	*50%*	*62%*	*19%*
MHA:IT 1:2	*67%*	*70%*	*39%*
IT	*100%*	*100%*	*NT*

Figure 3.3.4: (Left) Summary of percentage catalyst values determined for each method used. SYN – synthetic (ideal) percentage. DCP – NMR determined percentage by decomposing nanoparticles with iodine. PSS – NMR determined percentage by using the post-synthesis supernatant concentrations. EA – elemental analysis using hydrogen-carbon-nitrogen ratios. NT – Not tested.

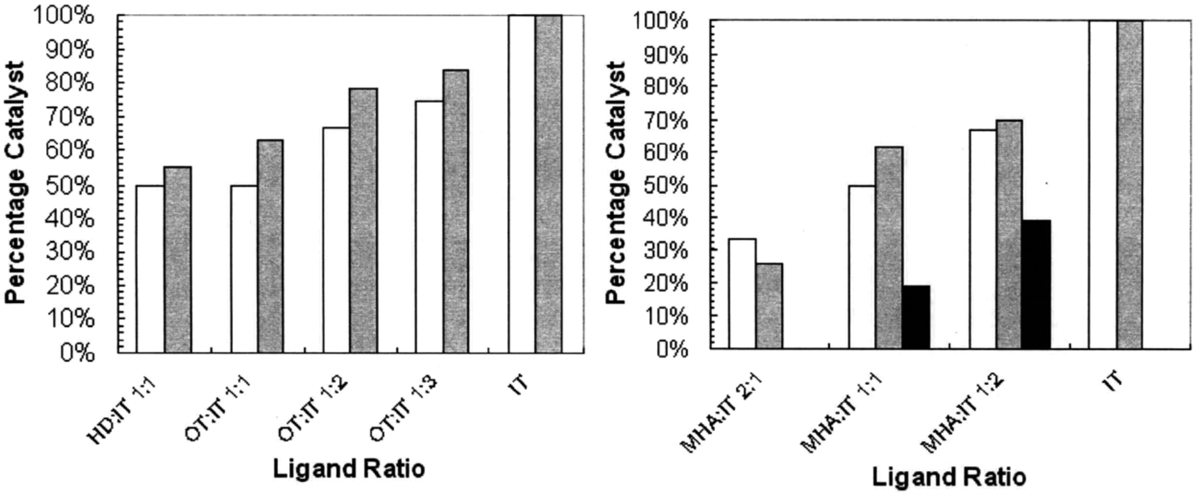

Figure 3.3.5: Plots of percentage catalyst as a function of ligand ratio. **(Left)** For the OT:IT system the white bars represent the synthetic (SYN) percentage and gray bars represent the decomposition (DCP) percentage. **(Right)** For the MHA:IT system white bars represent the synthetic (SYN) percentage, gray bars the post-synthesis supernatant (PSS) percentage, and the black bars the elemental analysis (EA) percentage.

In general the NMR based techniques showed a close comparison to the ideal, synthetic ratio. Only the elemental analysis of the MHA-IT system showed a significant difference from the expected ratio. In these samples an excess oxygen quantity was measured and it is conjectured that excess solvent, particularly water, remained in the particles despite vigorous drying. This suggests that new methods are needed for preparing samples for future elemental analysis.

From the material analysis data the extinction coefficient[3] of each particle batch could be determined using a previously developed empirical formula[5]. This extinction coefficient allowed the quantification of the *average* particle concentration in solution by measurement of the nanoparticle plasmon at 540 nm, base-lined at 850 nm. This concentration of particles (mol nanoparticles / L = M_{np}) could be converted to a concentration of catalyst (mol cat / L = M_{cat}) and used in evaluating the pseudo 1st order catalytic rate, k_{cat} ($1/sM_{cat}$):

$$k_{cat} = \frac{k_{observed}}{M_{cat}}$$ **Equation 3.3.1**

It should be noted that although the rate constant is pseudo first order, I scale the rate by the catalyst concentration in order to compare the kinetics of a single ligand in the monolayer. This gives a clearer measure of how local structure in the monolayer is affecting catalysis.

3.4 Catalytic Hydrolysis Trials – pH Dependence Reproduction

The first catalytic trials performed for the particles were on the OT-IT and HD-IT system to verify the behavior seen in the Scrimin et al work. This was to prove that my experiments were operating consistently and to compare my data against the established literature. Each series of particles was run in 3:2 ethanol:water buffered by combinations of HEPES and MES ranging between 4.9 to 7.1. In general, the catalytic rate is not linearly proportional to the ratio of substrate and catalyst (the excess ratio), therefore the concentration of *catalyst* and *substrate* was kept constant at ~ 6x M_{sub} / M_{cat}.

The trend in the catalytic rate for each ligand ratio in the OT-IT and HD-IT series show a sigmoid transition around ~ 6.0 – 6.5 pH followed by a drop off at ~ pH > 6.8 – 7.0 (**Figure 3.4.1**). The transition is close to the expected pK_a of an imidazole 3N-imide at ~ 6.8. At this ionic concentration, going from basic to acidic, the imidazole imido nitrogen becomes protonated and charged.

---

[3] The extinction coefficient, ε, is the imaginary component of the dielectric constant, κ, as related by: $\kappa^{\frac{1}{2}} = n + i\varepsilon$, with n the refractive index. The extinction coefficient quantifies the energy loss of radiation as it passes through material.

There is no observation of a cooperative enhancement peak as was observed by Scrimin and co-workers in their system. It is not possible to conclude that the original experiments are incorrect because the current system has two major differences from the Scrimin and co-workers' investigation: (1) the catalyst ligands, although containing the same catalytic functional group, are structurally different and (2) the current work uses particles that were synthesized with the catalyst, whereas Scrimin and coworkers prepared mono-ligand nanoparticles first and added the catalyst ligands afterward by an insertion mechanism. Therefore, it is possible a subtle difference in the monolayer chemistry has occurred which excludes cooperativity in the current system.

From the pH tests it was clear that the highest rates, and thus the better resolution, could be obtained above the pK_a, at pH ~ 6.3 - 6.5, therefore all subsequent hydrolysis reactions were run in this regime.

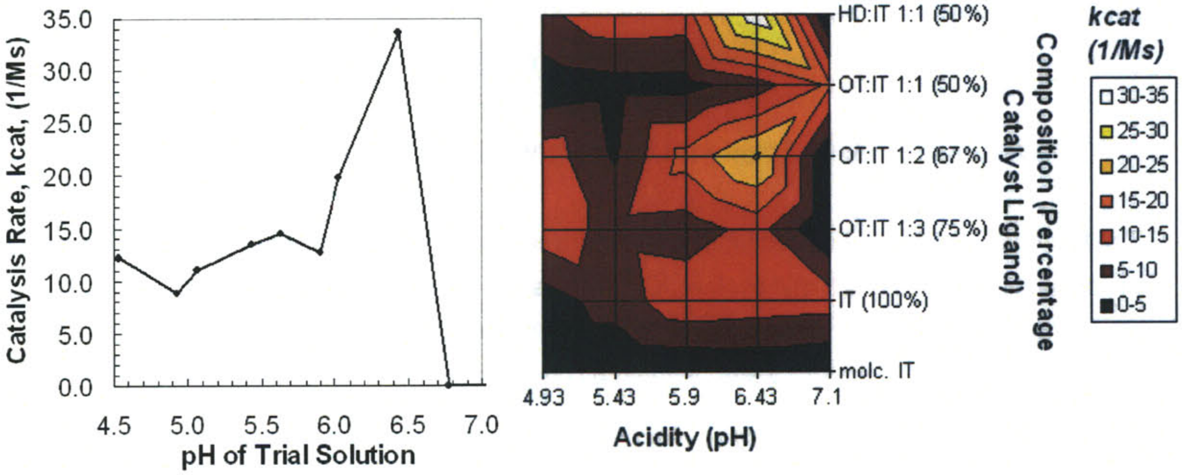

Figure 3.4.1: (Left) Example of catalytic rate as a function of acidity for HD:IT 1:1, demonstrating the sigmoidal transition at ~ pH 6.0 and the solubility loss at pH > 6.5. **(Right)** OT:HD:IT synthesis 1 catalytic rates as a function of acidity in an overview map. The brighter the section of the map, the larger the catalytic rate. It can be seen that a modulation in catalysis is seen at pH ~ 6.4, and that solubility drops off after 7.1. In addition the free form molc. IT control shows a far lower catalysis compared to the nanoparticles.

3.5 1-Octanethiol and 1-Hexadecanethiol : 11-(1N-imidazo)-undecane-1-thiol Catalytic Hydrolysis Trials

Catalysis rates of the OT-IT and HD-IT systems were measured using the initial rate of reaction which is given by the linear regime obtained in the first two hours of catalysis, shown in **Figure 3.5.1**. This was done because these particle systems are very slow and require almost a day to complete. As will be discussed further, the alternative method is to measure the catalytic rate by fitting it to the fully developed kinetic curve, which is how the MHA-IT system was analyzed. Quantitatively these two methods cannot be compared, as the initial rate is usually an order of magnitude larger than the full kinetic curve's rate, however the qualitative *trend* is reproducible between the two methods and is acceptable since I am concerned with observing the relative difference between ripple and non-ripple particles.

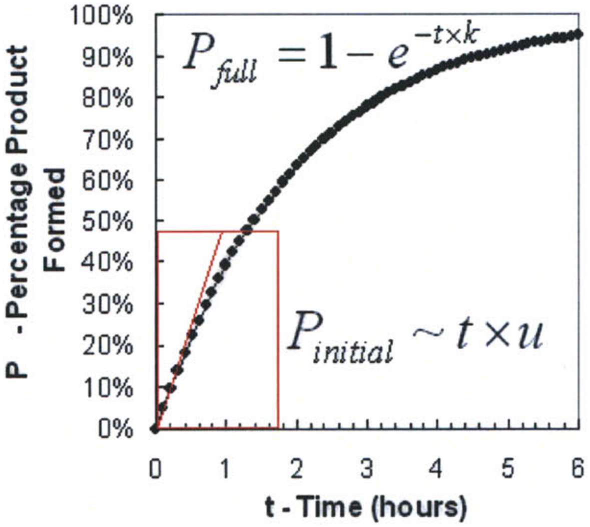

Figure 3.5.1: Schematic kinetic curve showing the percentage of product, P, formed by a hypothetical catalyst as a function of time. The curve illustrates the differences in the *full catalytic rate*, k, which describes the entire, exponential, catalytic process up to completion, and the *initial catalytic rate*, u, which describes only the linear regime seen in the beginning of the catalysis. The slope of the initial linear regime defines u, whereas k must be obtained from fitting the entire kinetic curve.

To prove that the particles are the source of the catalytic rate, samples of nanoparticles in the reaction solution were prepared and then filtered to remove the nanoparticles. The reaction solution was tested for catalysis and showed only the background solvent induced catalysis rate, demonstrating that the particles are the source of catalysis and that no contaminate in the nanoparticle or reaction solutions is adding to catalysis. The free form molecular catalyst ligand (molc. IT) was run to demonstrate the previous result that the nanoparticles enhance catalysis over the free form.

OT-IT and HD-IT were run at pH = 6.4 as a compromise between the protonation of the imidazole (which lessens its catalysis rate) and the increased insolubility of the particles at more basic levels. Non-ripple, homo-ligand OT or HD monolayer particles could not be tested in the ethanol:water system due to insolubility. Homo-ligand IT particle were run as the non-ripple control and compared to these particles with the 1:2 OT:IT and 1:1 HD:IT particles showing an enhanced catalytic rate. The 1:3 and 1:1 OT:IT particles showed a suppressed catalytic rate, and in comparing 1:1, 1:2 and 1:3 OT:IT a modulation in rate is observed. **Figure 3.5.2** summarizes the catalysis rates for the OT-HD-IT synthesis 1. Using a testing of hypothesis (t-test) it is found that the difference in means between any two ligand ratios is significant with 99% confidence.

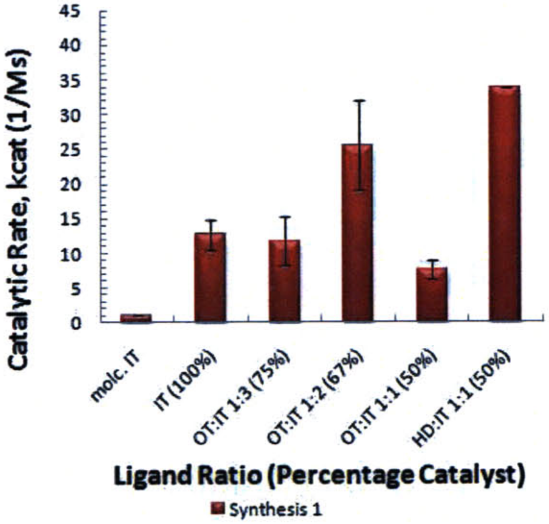

Figure 3.5.2: Catalytic rate as a function of ligand ratio for the OT:HD:IT synthesis 1, demonstrating the modulation in catalytic rate with ligand ratio and the weak enhancement in catalysis (i.e. HD:IT 1:1 and OT:IT 1:2) compared to the homo-ligand catalyst.

To focus on reproducibility the OT-IT system was considered alone. For intra-batch trials the reproducibility between trails shows deviations mainly in the ripple domain particles with deviations of +/- 20% at maximum (**Figure 3.5.2**). When the same batches of particles are tested over time it was seen that after a gap of two months between the first and second series of trials that the observed catalytic rate decreased, most observably for the 1:3 and 1:2 OT:IT particles

(**Figure 3.5.3**). Using an analysis of variance, it is found the population means are the same for the catalysis rates over time with 48% confidence.

For inter-batch trials, a new OT-IT synthesis 2 was made. Comparison of the catalytic rates for these trials shows a large deviation in the values between syntheses (**Figure 3.5.4**). The observed rates for the homo-ligand fluctuate within the same range as the ripple domain particles. The highest catalytic rate for the ripple domain type particles shifts from 1:2 to 1:1. An analysis of variance finds that the population means are the same (and thus reproduce) for the catalysis rates between syntheses 1 and 2 with only 15% confidence.

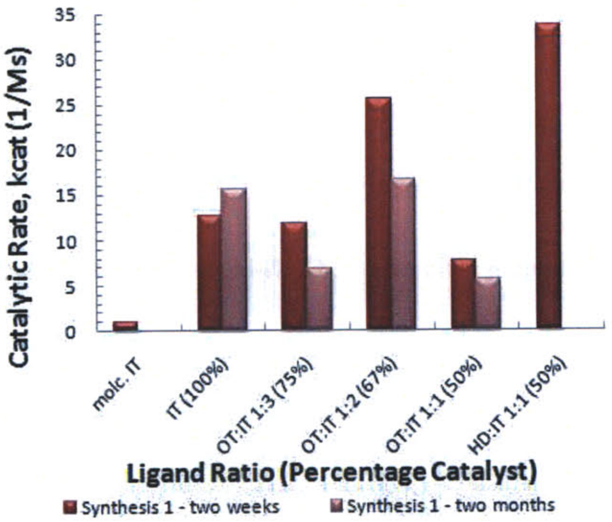

Figure 3.5.3: Catalytic rate versus ligand ratio for the intra-particle reproduction of OT:HD:IT Synthesis 1.

Although the HD-IT system showed a marked enhancement in catalytic rate over both the OT-IT and homo-ligand IT particles, it was difficult to reproduce the synthesis of these particles. All synthetic attempts produced particles that showed very low solubility in ethanol and could not hydrolyze. This limited further investigation on this system, but the data is included here to demonstrate why the MHA-IT system was developed based on the HD-IT's rate.

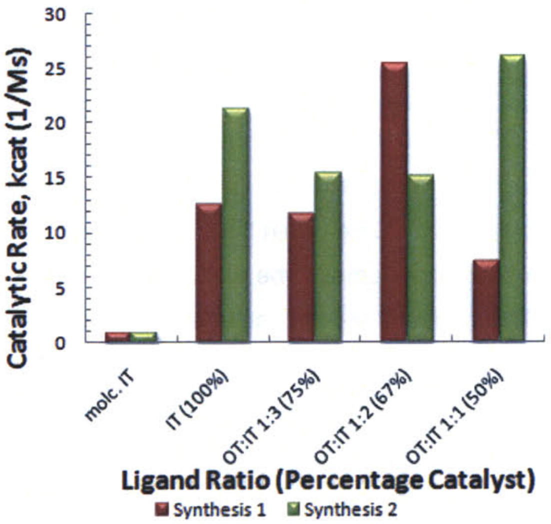

Figure 3.5.4: Catalytic rate versus ligand ratio for the inter-particle reproduction of OT:IT system.

3.6 16-Mercaptohexadeca-1-oic acid : 11-(1N-imidazo)-undecane-1-thiol Catalytic Hydrolysis Trials

MHA-IT catalysis trials ran a magnitude faster than OT-IT or HD-IT (2 to 4 hr compared to 12 to24 hr). This allowed the full kinetics curve to be obtained and the full catalysis rate to be calculated. The absolute values of the observed rates from MHA-IT cannot be compared to OT-IT or HD-IT, however the *trends* in the relative rates can be, equivalent to comparing the *ratios* of the rates for the same particle types within a series. The particles were tested to demonstrate they were catalytic by adding multiple doses of substrate to the same solution of particles (**Figure 3.6.1**).

As discussed the presence of borate in the homo-ligand IT particles required an additional hydrolysis step. The two IT batches synthesized for MHA:IT syntheses 1 and 2 were used to generate the MES and acetic acid hydrolyzed particles, respectively. These particles were tested as the non-ripple controls.

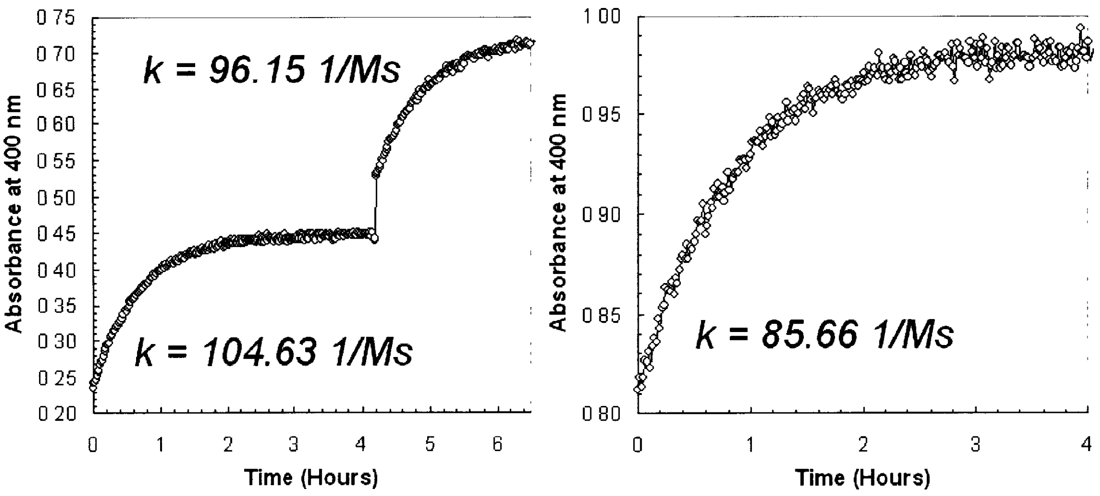

Figure 3.6.1: Plots showing the product formation, as tracked by absorbance at 400 nm, as a function of time for a single catalyst trial of MHA:IT 1:1 synthesis 1 particles. Three doses of substrate have been added to demonstrate the catalytic nature of the particles; each dose of substrate is completely converted to product as seen by the three plateaus. The catalytic rates, k, for each dose are given. **Left** – Two doses of substrate added at 0 and 4 hr on the first day. The jump seen at 4 hr is due to the increase in absorbance at 400 nm from the substrate. **Right** - Third dose of substrate added at 0 hr after letting trial sit for 12 hr overnight.

The MHA-IT series show that the ripple domain particles', 2:1, 1:1 and 1:2 MHA:IT all have attenuated catalytic rates compared to the homo-ligand catalyst particle (**Figure 3.6.2**). The rates, going with increasing catalyst loading, show a rough monotonic increase in catalysis rate, which must be considered remembering that all hydrolysis trials were run with the same loading of catalyst and substrate. A slight modulation is seen within the ripple domain particles, with 1:1 having an enhanced catalytic rate compared to 2:1 and 1:2.

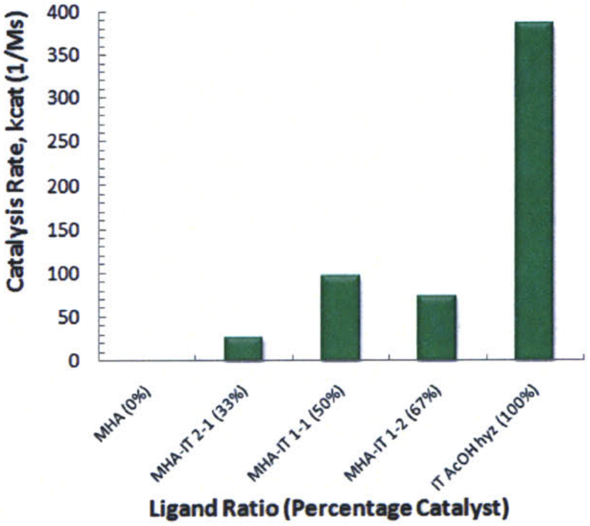

Figure 3.6.2: Catalytic rate as a function of ligand ratio for the MHA-IT synthesis 1.

To prove that the particles are the source of the catalytic rate, samples of nanoparticles in the reaction solution were prepared and then filtered to remove the nanoparticles. The reaction solution was then tested for catalysis and showed only the background water induced catalysis rate, demonstrating that the particles are the catalysis source and that no contaminate in the nanoparticle or reaction solution is adding to catalysis. The free form, molecular catalyst control could not be run because of its insolubility in pure water.

To test the intra-batch reproducibility of MHA-IT particles, samples were run using a UV-VIS plate reader spectrometer. Eight independent samples could be run simultaneously and 24-36 independent trials were collected. This method is limited to measuring the initial rate obtained in the first 10 minutes of reaction. As before, the observed rates cannot be compared quantitatively to the full kinetic curves, but the trend is seen to be the same. As is observed, the reproducibility is good within the same series of particles (see **Figure 3.6.3**).

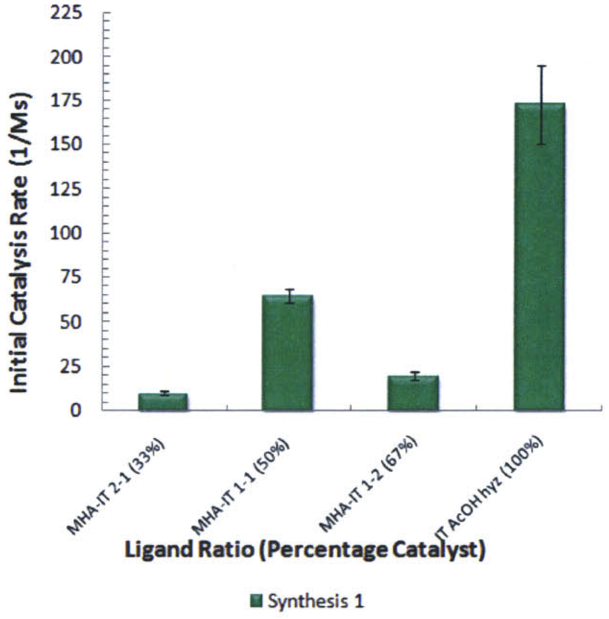

Figure 3.6.3: Initial catalytic rate as a function of ligand ratio for the intra-particle reproduction of MHA-IT synthesis 1. The error bars show the first standard deviation of 24-36 independent trials.

To test inter-batch reproducibility a second series was prepared, MHA-IT synthesis 2. MHA-IT synthesis 2 was tested to demonstrate catalytic capability using multiple-doses of substrate (**Figure 3.6.4**). This series demonstrated good intra-batch reproducibility (**Figure 3.6.5**) but, when compared to the first MHA-IT series, showed poor inter-batch reproduction, especially for 1:2 MHA:IT (**Figure 3.6.6**). The inter-batch reproducibility is poor regardless of whether measuring the initial catalysis rate (**Figure 3.6.5**, 42% confidence of reproducibility, analysis of variance in population mean) or the full catalysis rate (**Figure 3.6.6**, < 1% confidence of reproduction, analysis of variance in population mean).

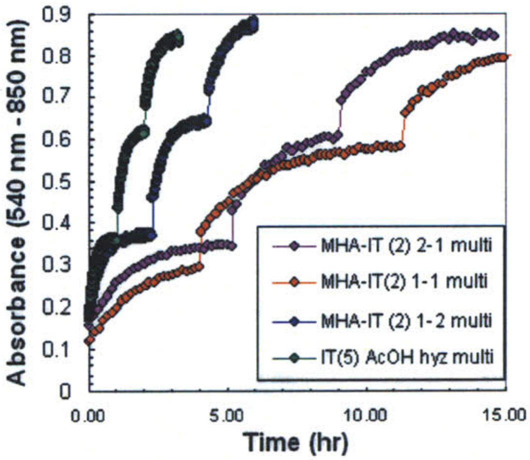

Figure 3.6.4: Plot of product formation, as tracked by absorbance at 400 nm, as a function of time for single catalyst trials of MHA:IT synthesis 2 particles. Each particle trial has been run with three doses of substrate added sequential. Each dose of substrate is completely converted to product as seen by the asymptotic plateaus. The plot demonstrates the catalytic nature of the nanoparticles.

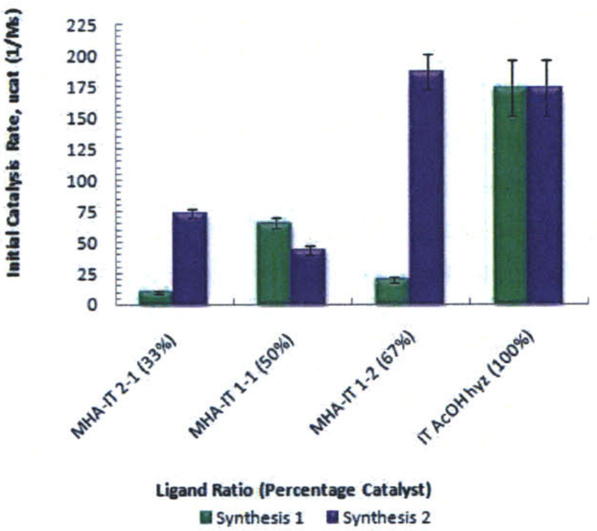

Figure 3.6.5: Initial catalytic rate as a function of ligand ratio for the intra-particle reproduction of MHA-IT system. Synthesis 1 – white dots, synthesis 2 – black dots. The error bars show the first standard deviation of 24-36 independent trials.

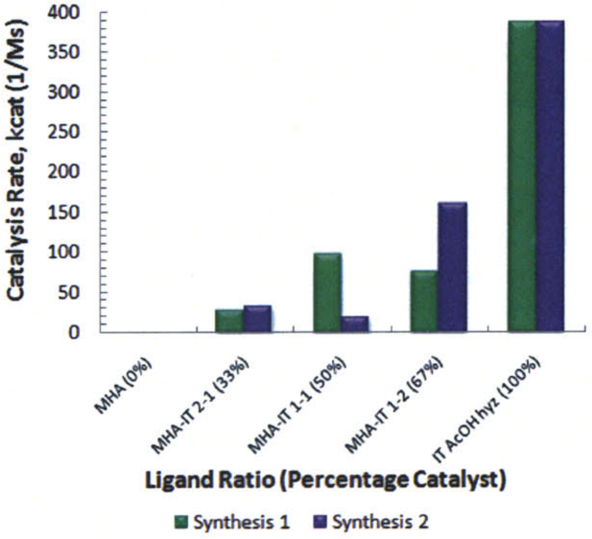

Figure 3.6.6: Catalytic rate as function of ligand ratio for inter-batch reproducibility of MHA-IT system. Synthesis 1 – white dots, synthesis 2 – black dots.

3.7 16-Mercaptohexadeca-1-oic acid : 11-(1N-imidazo)-undecane-1-thiol Binding Constant and Efficiency Trials

The rapid catalytic rate in the MHA-IT system afforded the opportunity to obtain information on the kinetic parameters of the particles, in particular the binding constant and the efficiency of catalysis. Observation of the catalysis efficiency provides another quantity which can be compared for testing the hypothesis. The quantification of the efficiency is based on the Michaelis-Menten formulation of enzymatic catalysis, which describes the kinetics of a catalysis which requires the formation of a catalyst-substrate complex or intermediate to proceed. I am led to this analysis by envisioning that for the substrate to become hydrolyzed, it must interact with the particle surface. In the case of the MHA:IT particles, the catalyst is below the monolayer/solvent interface, thus I imagine the substrate must become somewhat embedded or bound to the monolayer to be effectively catalyzed. I draw an analogy of this surface interaction as a bound intermediate and seek a quantification of its kinetics.

To obtain the efficiency, first the binding constant K was obtained. Hydrolysis trials for the two series of MHA-IT particles were run using the UVVIS plate-reader method. A series of hydrolysis trials was run at varying levels of substrate concentration (at a fixed catalyst concentration) as shown in **Figure 3.7.1**. The MHA homo-ligand particle was not run in these experiments because it showed no catalytic activity. From the plot of initial rate versus substrate loading (**Figure 3.7.2**) the binding constant and the maximum velocity is obtained. The binding constant is seen to be fairly reproducible between the two syntheses (**Figure 3.7.3**) with an analysis of variance finding a 74% confidence that the population means are the same between syntheses. The maximum initial catalysis rate is more sporadic (**Figure 3.7.4**) with a 54% confidence of reproduction between syntheses (by analysis of variance), a statistical value close to that seen for the reproducibility in the inter-batch catalysis rates, of which the maximum rate closely mimics trend-wise. The maximum efficiency, calculated from the ratio of the maximum catalytic rate and the binding constant, also fluctuates wildly (**Figure 3.7.5**) with a 32% confidence of reproduction (by analysis of variance).

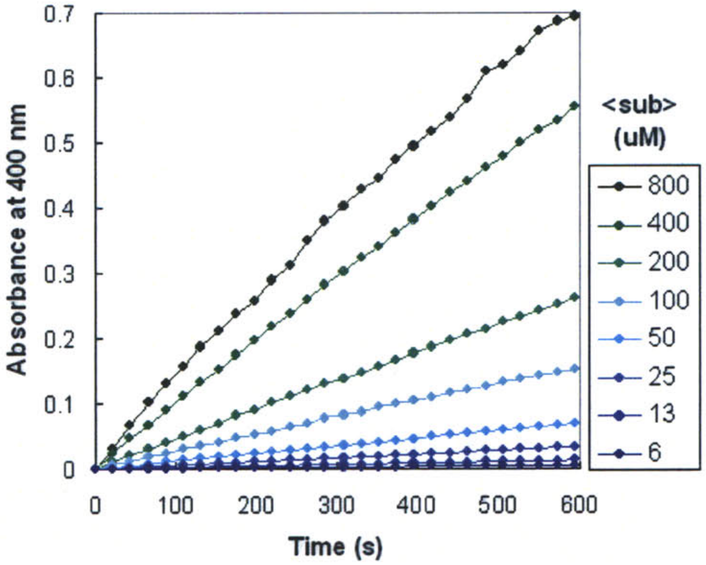

Figure 3.7.1: Example of kinetic curves, from MHA:IT 1:2 synthesis 1, for series of substrate concentrations, <sub>, for the binding constant determination.

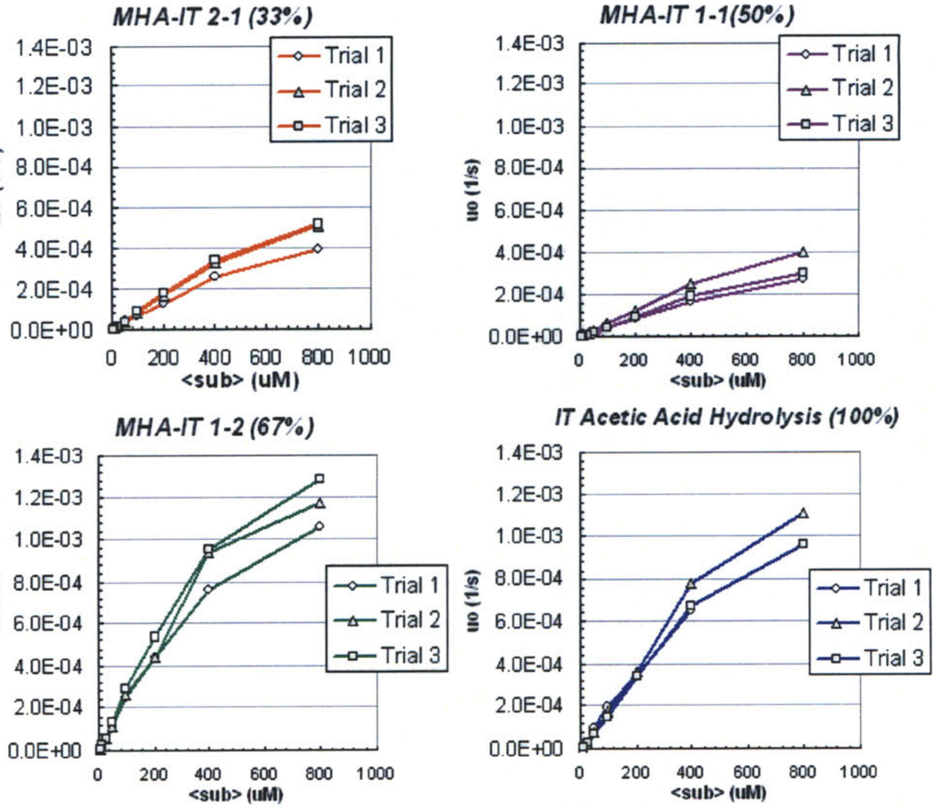

Figure 3.7.2: Initial catalysis rates as a function of substrate concentration for the MHA-IT synthesis 2 demonstrating the reproduction in the trials. All scales are equivalent.

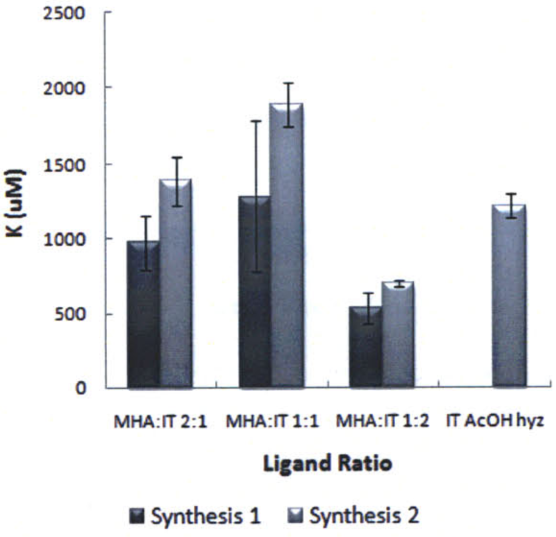

Figure 3.7.3: Binding constant, K, as a function of ligand ratio for MHA-IT system. The control MHA was not run because it showed no catalytic activity.

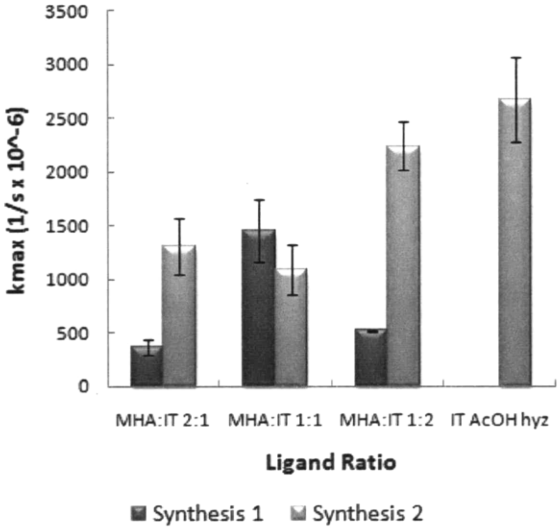

Figure 3.7.4: Maximum initial catalytic rate, u_{ma}, as a function of ligand ratio for MHA-IT system. Synthesis 1 – red bars, synthesis 2 – maroon bars. The control MHA was not run because it showed no catalytic activity.

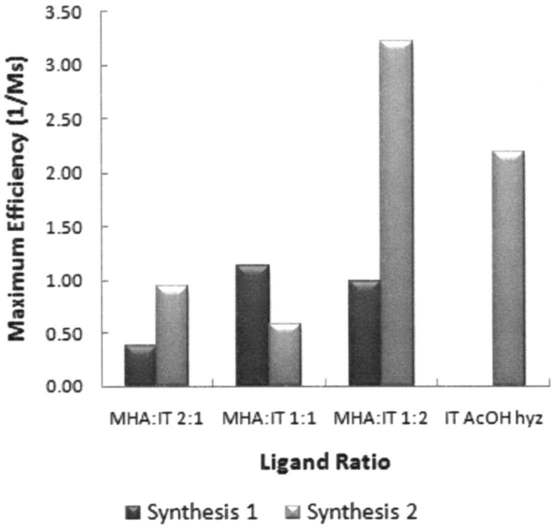

Figure 3.7.5: Efficiency as a function of ligand ratio for MHA-IT system. Synthesis 1 – green bars, synthesis 2 – emerald bars. The control MHA was not run because it showed no catalytic activity.

3.8 16-Mercaptohexadeca-1-oic acid : 11-(1N-imidazo)-undecane-1-thiol Thermodynamics of Catalysis

To compliment the kinetic parameters, the thermodynamics of the MHA-IT system were analyzed. Hydrolysis trials were run at constant catalyst and substrate loading but varying temperatures (between 10 ^{0}C and 80 ^{0}C). The resulting Arrhenius plots could be fitted to obtain the activation energy E_A and attempt frequency (see **Figure 3.8.1**). The correlation factors, r, for the Arrhenius fits are given in **Table 3.8.1**, showing between -0.8 to -1.0 correlation, indicative of a strong inverse relation as is expected. The activation energy is seen to reproduce well inter-batch (**Figure 3.8.2**), with an analysis of variance finding a 68% confidence that the population means are the same between syntheses. The acquired values for the activation energy for the different ligand ratios are nearly the same, and are about half the non-catalyzed hydrolysis of DNPA literature value, ~ 48 kJ/mol, and the value determined empirically in-house, ~50 kJ/mol.

The attempt frequency is highly irreproducible in magnitude; though it follows the same trend in relative value when normalized (compare the left and right plots in **Figure 3.8.3**). For the normalized values there is a 90% confidence that the population means are the same between syntheses (by analysis of variance), suggesting the relative pattern of modulation is reproducing, although the absolute values are considerably altered.

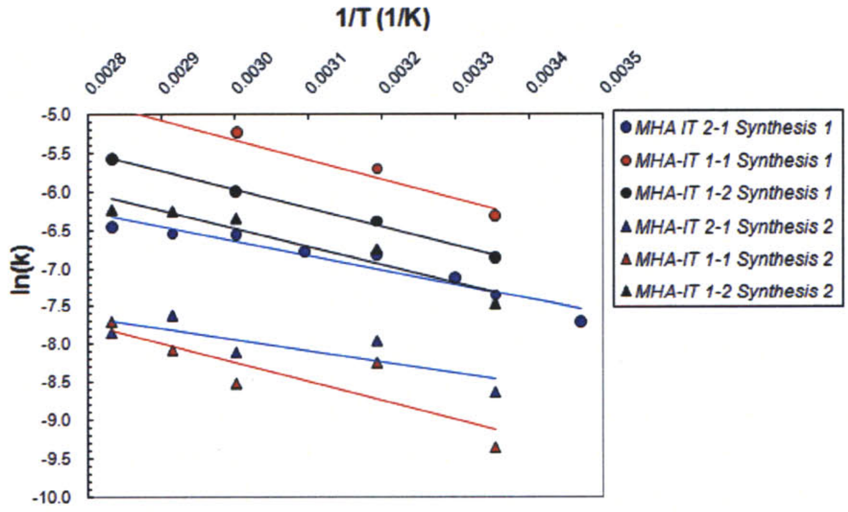

Figure 3.8.1: Arrhenius plots from temperature series for MHA-IT system. The control MHA was not run because it showed no catalytic activity.

Synthesis 1

Ligand Ratio	***r***
MHA:IT 2:1	-0.82
MHA:IT 1:1	-0.87
MHA:IT 1:2	-0.96
IT AcOH hyz	-0.95

Synthesis 2

Ligand Ratio	***r***
MHA:IT 2:1	-0.96
MHA:IT 1:1	-0.98
MHA:IT 1:2	-1.0
IT AcOH hyz	-1.0

Table 3.8.1: Correlation factors, r, for the Arrhenius plots of MHA:IT particles in **Figure 3.8.1**. A correlation factor of r = -1.0 implies a strong, negative relation between the ln(k_{cat}) and 1/T, as implied by Arrhenius-type temperature activated reactions. A factor of r = 0 implies no correlation.

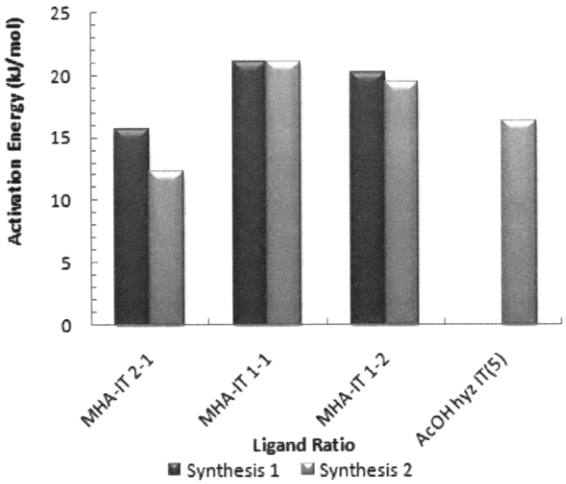

Figure 3.8.2: Activation energy as a function of ligand ratio for MHA-IT system. The control MHA was not run because it showed no catalytic activity.

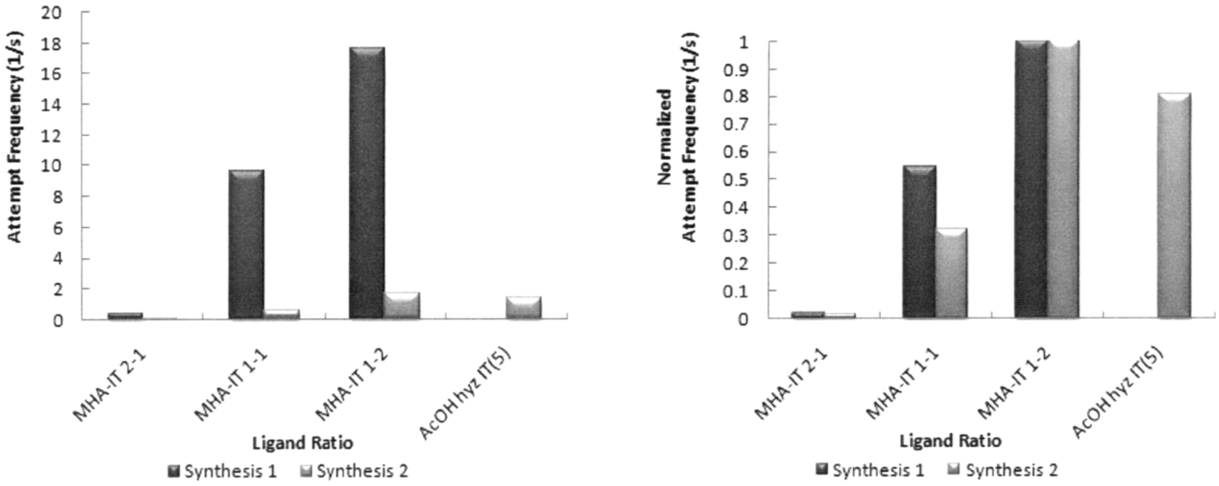

Figure 3.8.3: (Left) Attempt frequency as a function of ligand ratio for MHA-IT system as measured. The control MHA was not run because it showed no catalytic activity. **(Right)** Normalized attempt frequency as a function of ligand ratio, demonstrating modulation with ripple domain.

3.9 Attempted Knoevengel Condensation Type Catalysis Reactions

The results from the OT-IT and HD-IT hydrolysis trials prompted a search to expand these particle systems to other catalytic reactions that would reproduce more consistently. The hydrolysis reaction of the DNPA ester, though easy to observe and well characterized, represents a facile chemical target; the ester bond is highly reactive due to the gain in entropy upon hydrolysis and the delocalization of electron density back into the activated phenyl ring. A new target was set to carry out catalysis on a *bond forming* reaction as another method of testing the hypothesis. To improve the clarity of analysis, a single, organic solvent, chloroform, was used. An aldol-type condensation reaction was chosen in which the basic properties of the imidazole could be used catalytically. The Knoevengel Condensation (K-con), shown schematically in **Figure 3.9.1**, occurs when a highly acidic carbon center is deprotonated to form an enolate which then condenses with an aldehyde to produce a carbon-carbon bond[6,7]. Further dehydration generates an olefin. The reaction is catalyzed by a base which extracts and transfers protons, and can be catalyzed by organic bases such as piperidine, pyridine, imidazole and pyrrol[6].

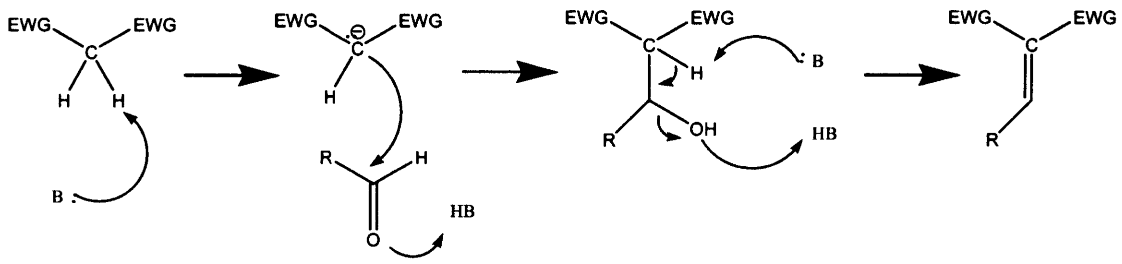

Figure 3.9.1: Schematic of general Knoevengel Condensation (K-con) of an activated carbon center with an aldehyde by a base. The 2nd step demonstrates the formation of the enolate on the acidic carbon center. B – base, EWG – electron-withdrawing group (acceptor).

A K-con reaction with ethyl cyano-acetate (ECA) as the acidic carbon center and nitrobenzyl aldehyde (NBA) was attempted (see **Figure 3.9.2**). NBA was chosen since it absorbs in the visible regime at ~ 266 nm, and upon condensation forms (Z)-ethyl 2-cyano-3-(4-nitrophenyl)acrylate (ECNA) which has a delocalized pi system and concomitant bathochromic shift to ~ 340 nm (**Figure 3.9.3**). The reaction was run in chloroform at 90 ^{0}C with OT-IT and HD-IT particles[8]. As with the hydrolysis reaction, the concentration of catalyst was kept the same for all the ligand ratios. The reaction was monitored over two days and the absorbance (concentration of ECNA) plotted versus time. A sample of ECNA was synthesized using pyridine, purified and its NMR and UV-Vis analyzed in order to verify the relation between the absorbance signal and the molecular structure.

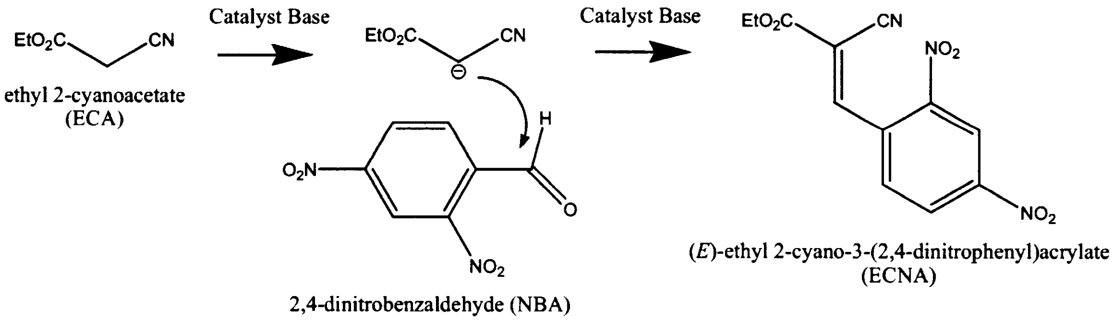

Figure 3.9.2: Schematic of Knoevengel condensation used in this study.

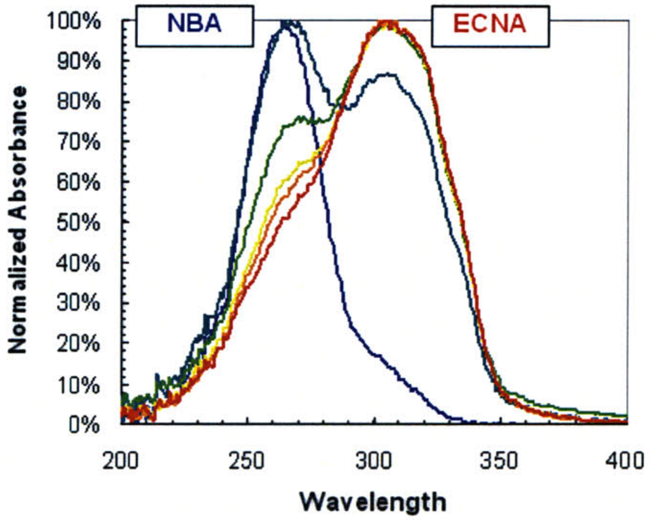

Figure 3.9.3: UV-Vis absorbance series showing the red-shift transition between the substrate aldehyde, NBA, and the final product, ECNA.

No kinetic rate could be obtained from the data. It was observed that for a given series, with increasing catalyst ligand the quantity of ECNA would rise up and then level off, as seen in **Figure 3.9.4**. Since all samples had the same loading of substrates they should level off at the same final ECNA concentration, but instead the higher the catalyst ligand percentage the higher the leveling off value. This implied that the reaction was not going to completion but instead reacting to some stage and then desisting (or proceeding too slow to quantify). This was further confirmed when an additional dose of substrates was added and no further rise was observed. A plot of catalyst ratio versus the leveled off quantity of ECNA (**Figure 3.9.5**) is linear, suggesting that either the amount of catalyst (or filler) dictates the leveling off.

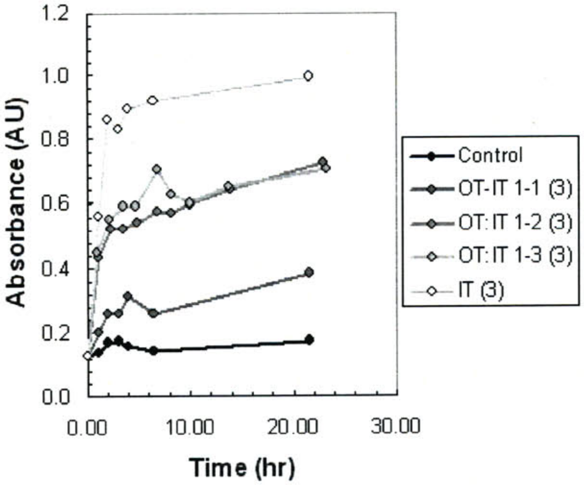

Figure 3.9.4: Kinetic curves of the Knoevengel condensation catalysis trials with OT:IT synthesis 1, demonstrating the unusual leveling off behavior.

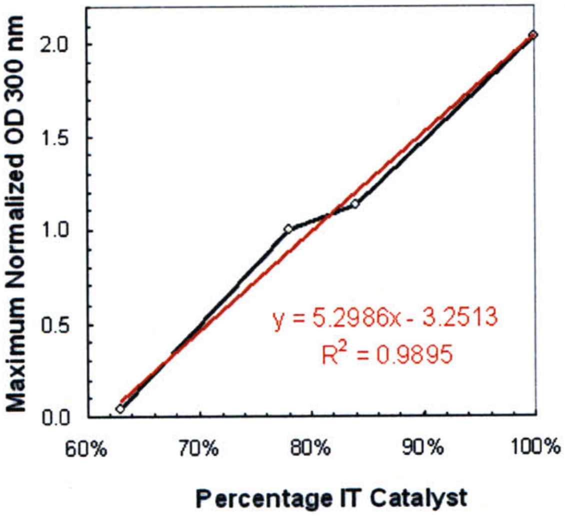

Figure 3.9.5: Maximum leveling off absorbance as a function of percentage catalyst in the OT:IT synthesis 1 series, showing the linear relation of the two properties.

When a solution of nanoparticles is filtered through a 100 nm PTFE filter to remove the particles and the extract is run in the K-con reaction the same leveling off is observed (see **Figure 3.9.6**). This suggested that something in the supernatant of the particle solutions was reacting. From previous work in our group we have known about the possibility of borate contaminates from the synthesis of the particles. To test if borate could cause the observed reaction, a sample of borate solution in ethanol was prepared at the molarity used in nanoparticle synthesis. When this solution is added to a chloroform solution of the substrates an immediate color change is observed, demonstrating the rapid reaction of NBA and ECA caused by the borate (**Figure 3.9.7**). The absorption spectrum of this reaction matches identically to that observed in the K-con and thus implied a borate contaminate in the particle solutions was the cause of the peculiar K-con data. Using a THF solution of NBA and ECA as a qualitative test of borate contaminate, the centrifuge purification method was retested to see if borates existed in solution. It is found that if particles are not washed at least three to eight times with water that the borates will persist in the particles and leech into solution (**Figure 3.9.8**). The MHA-IT particles were washed with ethanol instead of water, however the borate test showed no contaminates after four-five washes. From the extract experiments run on each series of particles it is known that the borate contaminates do not affect the hydrolysis reaction, since the extracts have catalysis rates equivalent to pure solvent. However the presence of the borates determined by these experiments led to the re-evaluation of the IT particles' poor solubility and the subsequent hydrolysis step.

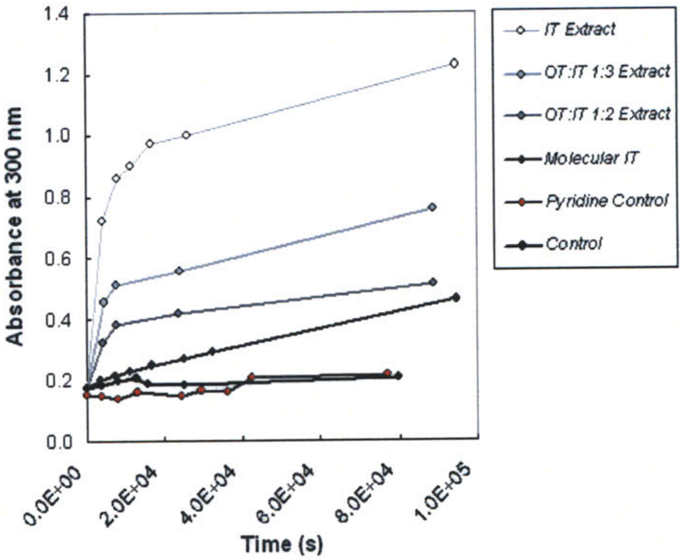

Figure 3.9.6: Kinetic curves of the Knoevengel Condensation catalysis trials with the extracts of OT:IT synthesis 1, demonstrating the supernatant induces the leveling off behavior.

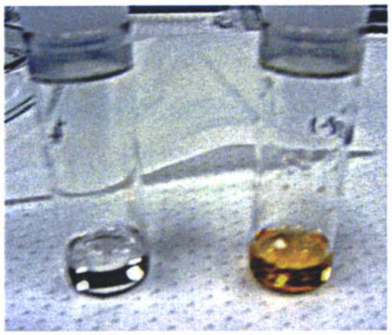

Figure 3.9.7: Picture of the color-change induced in an NBA / ECA mixture with the addition of borate solution.

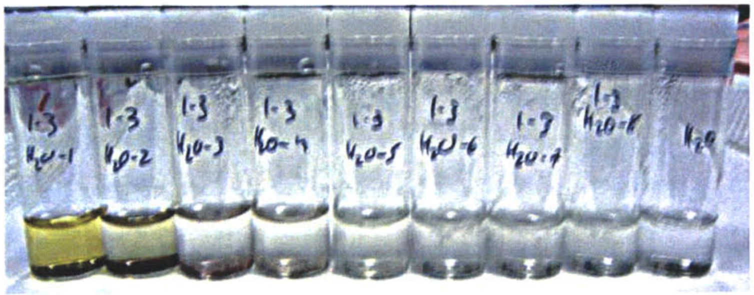

Figure 3.9.8: Series of water supernatants from water wash centrifugations of OT-IT 1-3 synthesis 2, demonstrating the loss of borates. The borate test color disappeared spectroscopically by wash five, but three more washes were carried out to be thorough. The right-most vial contains pure water as a qualitative standard.

When OT-IT nanoparticles are cleaned with water and retested in a K-con reaction, the resulting ECNA formation versus time is very slow and erratic (see **Figure 3.9.9**). The data shows that no major catalysis is taking place with the imidazole nanoparticles, regardless of ripple or non-ripple monolayers, which suggests the imidazole chemistry itself is not entering into the reaction. The pK_a of the acidic carbon center of ECA is apparently too high for the imidazole to de-protonate, thus the reaction cannot initiate and no catalysis is seen. The deviation in the data is interesting, especially considering that large fluctuations are not seen in the control samples which contain only free ligand or no catalyst at all. All curves seem to exhibit a rise-then-dip behavior, which would imply an activated or more-conjugated complex is forming temporarily and then disintegrating in time. There is qualitatively a trend that the onset of the rise and dip is earlier with decreasing catalyst content. The nature of this behavior is beyond the current work of this thesis.

The main conclusion from the K-con experiments is that a more basic catalyst is required to test the hypothesis.

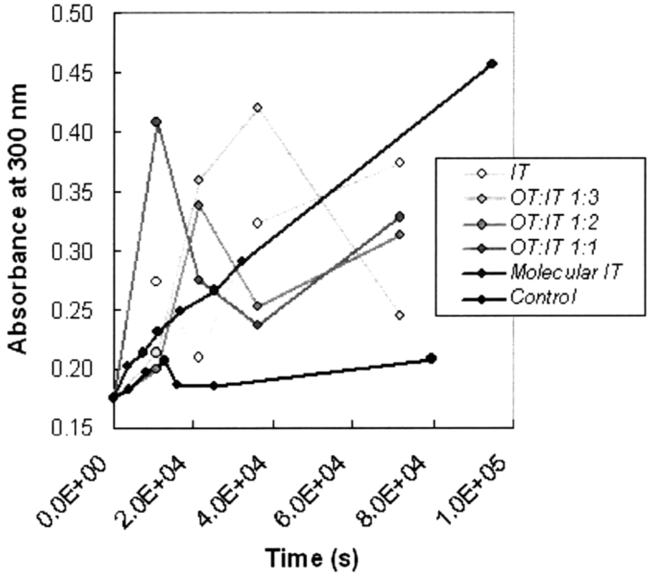

Figure 3.9.9: Kinetic curves of the Knoevengel condensation catalysis trials with the water purified OT:IT synthesis 1, demonstrating the lack of catalytic activity in the particles.

Chapter 3 References

1. Kuna, J.J. et al. On the Role of Nanometer Structure in Interfacial Energy. *Publication in progress.*
2. Pasquato, L., Rancan, F., Scrimin, P., Mancin, F. & Frigeri, C. N-Methylimidazole-Functionalized Gold Nanoparticles as Catalysts for Cleavage of a Carboxylic Acid Ester. *Chemical Communications*, 2253-2254 (2000).
3. Bailey PD. *Organonitrogen Chemistry*, (Oxford University Press, Oxford, 1996).
4. Sidgwick, N.V. *The Organic Chemistry of Nitrogen*, (Clarendon Press, Oxford, 1966).
5. Liu X, A.M., Wang J, Huo Q. Extinction Coefficent of Gold Nanoparticles with Different Sizes and Different Capping Ligands. *Colloids and Surfaces B: Biointerfaces* **58**, 3-7 (2007).
6. Carey FA, S.R. *Advanced Organic Chemistry*, (Springer, New York, 2007).
7. Phan NTS, J.C. Highly Accessible Catalytic Sites on Recyclable Organosilane-Functionalized Magnetic Nanoparticles: An Alternative to Functionalized Porous Silica Catalysts. *Journal of Molecular Catalysis A: Chemical* **253**, 123-131 (2006).
8. Wiley RH, S.N. m-Nitrosytrene. *Organic Syntheses* **4**, 731 (1963).

CHAPTER 4 - DISCUSSION

4.1 Evidence that Nanoparticles are the Catalysts

Before evaluating whether ripple domain nanoparticles modulate the catalytic rate compared to non-ripple particles, it is important to first establish that the particles can carry out catalytic reactions and are not simply reacting stoichiometrically.

The background catalysis rate of 3:2 ethanol:water is $k_0 = 1.25 \times 10^{-6}$ 1/s and in pure water $k_0 = 20 \times 10^{-6}$ 1/s . Comparatively, the OT:IT and HD:IT observed rates are between 66 and 150×10^{-6} 1/s, and for MHA:IT between 100 and 600×10^{-6} 1/s, demonstrating that the particles are affecting the hydrolysis of DNPA. If the particles are mixed with the reaction solvent, and then removed by filtration, the supernatant reproduces the background water hydrolysis rate, giving evidence that the particles are the source of catalysis and not a contaminant in the solution. This data only proves the nanoparticles react faster than the background solvent. To prove that the nanoparticles are catalytic, it is observed that the catalytic rates are the same even when the substrate loading is 6 to 10 times the catalyst concentration, i.e. there are 6 to 10 DNPA molecules for every catalyst ligand, suggesting catalysis and not stoichiometric reactions, is taking place. Furthermore, the direct evidence that the same sample of nanoparticles can fully catalyze two to three doses of substrate (each 6x the catalyst concentration) reinforces their catalytic nature. Although the OT:IT, HD:IT tests were run in the linear regime, if a trial test of particles is allowed to run to completion over a day it produces a full kinetic curve of average rate $k \sim 1.0 \times 10^{-4}$, an order of magnitude faster than water, demonstrating that at 6x excess substrate, the system is catalytic. The slight decrease over time in the catalysis rate in the multiple-catalysis trials is attributed to a misbalance in the pH as the large excess of acid product overwhelms the buffer concentration and induces aggregation and precipitation. For the present study no experiments were performed to test the catalytic activity from re-used nanoparticles.

4.2 Catalysis as Function of Acidity Series

The acidity series was used to compare the current ligand system to the original model developed by Scrimin and co-workers. It did not confirm the cooperativity peak seen by Scrimin et al. around the pKa point of the imidazole. This peak was assigned to the action of several imidazole groups working to complete each catalytic reaction. It is conjectured that this cooperativity is seen at the pKa due to a split in the imidazole population into protonated and de-protonated species, providing ligands capable of acid and base chemistry in close proximity. None of the OT:IT:HD series showed this cooperativity peak, and the MHA:IT system could not be tested for this peak due to the high precipitation seen at lower acidity.

It is not possible to test if the cooperativity peak has been shifted to higher pH in our system because no data can be obtained above ~ pH 7.1 due to precipitation. As stated, our catalyst ligand is not identical to the ligand used in Scrimin's work. The lengths of the IT and MID are different: 11 methylenes (1.26 nm) in IT versus 16 (1.89 nm) for the MID molecule. For IT, the linking of the imidazole occurs through the 1N position, as opposed to the 4C for MID, with the concomitant sealing of the 1N position with a methyl group, and the presence of the peptide bond which increase the overall length and exposes a carbonyl and secondary amine. The IT ligand used in our experiments was chosen due to its commercial availability and the suitability of its alkane chain length which allowed us to design experiments to test, along with morphology, the effect of the position of the catalyst in the ripple domain. The structural differences in the imidazole do not change the *chemistry* of the imine group, and thus are considered to a first approximation to be equivalent. The presence of the peptide bond is a possible difference in the systems, since this peptide can form a six-member ring conformation and thus lend its hydrogen bonding capability to the terminal catalysis.

A more important consideration is means of synthesis. Scrimin and coworkers used ligand exchange methods to produce their particles from pre-synthesized particles; therefore they did not expose the catalyst ligand to borohydride, and the catalyst ligand was physically inserted into the monolayer instead of self-assembling onto the nucleating core. The particles used in this study were produced by synthesis to maintain the same conditions that had previously been explored for ripple domain formation. The presence of borates could have an effect on any cooperativity because it alters both the chemistry of the imidazole by blocking the imine from forming a charge complex, and spatially by generating a larger excluded volume around the imidazole. However, the correct pKa transition seen in the acid catalysis trials suggests that the OT:HD:IT imidazoles can accept / donate protons and are therefore not bound in a borate complex.

In the Scrimin et al system the imidazole ligand extends beyond the aliphatic filler and thus if their system is viewed as a ripple domain type morphology, the catalyst site forms the ridges around the ripple domain gaps. Neither the OT:IT (extended catalyst site) or HD:IT (buried catalyst site) particles demonstrate cooperativity, suggesting this is not a condition for the cooperation. The rates observed in our system are about an order of magnitude larger than in the Scrimin work, which is expected considering our use of the linear regime in the kinetic curve.

Taken together, the data suggests that the mode of synthesis is altering the cooperativity in the particle shell. It may be that the ligand exchange method produces a monolayer morphology conducive to a cooperation mechanism, while the synthesis method produces a ripple domain morphology that does not support cooperation.

The main question is if the lack of cooperativity means the current particles cannot be used to evaluate the hypothesis. The current thesis is concerned with the effect of the ripple domain morphology on catalysis, *not* the effect on cooperativity. A cooperativity effect, as seen by Scrimin and coworkers, leads to a monotonically (though many times non-linear) rise in catalytic rate as a function of catalyst concentration on the nanoparticle; this is not the behavior that is being tested in the hypothesis. The nanoparticles possess the two requirements necessary for our experiments: they are catalytically active, and they are synthesized in the correct ratios and ligand parameters to possess ripple domain morphology. Therefore I consider it acceptable that the data obtained from these particles can be used to draw valid, scientific conclusions. The question of why the cooperativity is not apparent is an interesting side consideration. It is not valid to suggest the work of Scrimin and coworkers' is incorrect because the current system differs in several ways experimentally from this original work. The question of ripple domain and cooperativity is left for a future experimental direction.

4.3 Test of Hypothesis: Ripple and Non-Ripple Domain Nanoparticle Catalysis

In testing the hypothesis, we compare catalytic rates between the ripple nanoparticles and the non-ripple homo-ligand particles. As stated in section 3.4 I have controlled the experiments to be at constant catalyst concentration in order to measure the catalysis due to a single imidazole ligand; therefore I scale the pseudo first order rate constant by the catalyst concentration - k_{cat} (1/sMcat):

$$k_{cat} = \frac{k_{observed}}{M_{cat}}$$

Before examining the hypothesis it is important to observe that all nanoparticles are more active than the free-form ligand molecule. Although the catalyst particles all show large deviations in their catalytic rate, they all have catalytic rate magnitudes significantly larger than the free form catalyst rate by a factor of 10-30. The free form catalyst rate does not deviate by more than 1% when reproduced in triplicate. This result justifies investigating the catalytic chemistry of nanoparticles for it demonstrates the particles can yield an improvement over the pure ligand, a result which is not novel in nanoparticle catalysis but which is important to verify before proceeding to study effects of monolayer morphology. The enhanced catalysis rate of nanoparticles over the free-form catalyst ligand is not a cooperative effect but a *concentration effect* in which the local concentration of imidazole is orders larger in the local environment of the nanoparticle monolayer than is presence around a substrate in a solution of free ligand.

Comparing the OT:IT and HD:IT ripple domain nanoparticles to the non-ripple, homo-ligand catalyst particles for synthesis 1 it is observe that certain ripple domain ligand compositions exhibit an enhancement and others an attenuation in catalytic rate. In particular, the OT:IT 1:2 and HD:IT 1:1 particles both show an enhanced catalysis rate of ~ 2-3 compared to the homo-ligand, whereas the OT:IT 1:1 particles are lower by a factor ~ 2. The OT:IT 1:3 composition catalysis rate is close to the homo-ligand value. It must be considered that all nanoparticles were run at the same concentration of catalyst, and therefore if the concentration of catalyst was the only factor in the resultant catalytic rate it would be expected that all particles, ripple or non-ripple, would obtain the same rate. Instead we observe a modulated behavior, much akin to the surface energy modulation previously described. This behavior supports the hypothesis, suggesting that *octanethiol and hexadecanthiol / imidazole catalyst ripple domains modulate catalysis.*

The pattern of modulated catalysis rates reproduces for the same synthesis, demonstrating the observed modulation is real. When synthesis 2 is tested a modulation behavior in catalysis rate is also observed, with OT:IT 1:1 enhanced over the homo-ligand particles, and OT:IT 1:2 and 1:3 attenuated. The HD:IT 1:1 particles were not reproduced for the second synthesis due to troubles in their purification and solubility, therefore the inter-batch reproducibility is concerned only with the OT:IT particles. However, in comparing synthesis 1 and 2 it is observed that the pattern of modulation is inconsistent, with some nanoparticles showing enhancement in one synthesis and attenuation in another. Furthermore, the magnitude of the homo-ligand nanoparticle itself, which is the reference against which the hypothesis is tested, changes by a factor ~ 2 between the two syntheses. The deviations in the ripple particles are seen to be especially large for the ripple domain ligand ratios between 50-65% catalyst ligand. The deviations seen in the OT:IT and HD:IT system suggest that with the current data that the pattern of modulation cannot be predicted from the ligand ratios. Therefore we conclude the *hypothesis of ripple domain induced modulated catalysis is not supported by the octanethiol imidazole particles because the modulation pattern shows poor reproducibility between nanoparticle batches.*

For the MHA:IT system the free-form ligand cannot be tested in water due to its insolubility, demonstrating that the *acid-imidazole monolayer has the advantage of allowing the catalysis reaction to take place in a solution in which the catalysis is not readily soluble.* Comparing the MHA:IT ripple domain nanoparticles to the non-ripple, acetic acid hydrolyzed (AcOH hyz) homo-ligand catalyst particles and the MHA homo-ligand particles for synthesis 1 it is observed that all of the ripple domain particles have lower, attenuated catalysis rates compared to the homo-ligand catalyst particle. Between the ripple domain particles there is a weak modulation observed, with MHA:IT 1:1 slightly larger than either the 2:1 or 1:2 ligand ratios. The all-carboxylic acid homo-ligand particle shows no catalysis, proving that the *carboxylic acids are not the catalytic species*. As with the OT:HD:IT system, all of the MHA:IT particles were run with equal catalytic concentrations so if there was no effect due to morphology the catalytic rates should be equal. Instead there is a sharp distinction between the homo-ligand particles with high catalytic rates and the ripple domain particles which are all low. Therefore in the MHA:IT system it is observed that the ripple domain seems to suppress catalysis compared to the non-ripple particles, and this suppression is a form of attenuation which supports the hypothesis; *mercapto-hexadecanoic acid / imidazole catalyst ripple domains attenuate the catalyst, decreasing its rate.*

The attenuation pattern for the MHA:IT ripple domains reproduced within the same synthesis when tested with 24 to 36 independent catalysis trials using the plate reader method and measuring the initial rate of reaction. For synthesis 2 the homo-ligand nanoparticles still out-strip all of the ripple domain nanoparticles, but the pattern of modulation within the ripple domain particles is altered from that seen in synthesis 1. Thus, like the OT:IT system, the *MHA:IT system demonstrates modulation but cannot support the hypothesis due to strong deviation between nanoparticle batches.*

The overall conclusion is that the ripple domain morphology does affect the catalysis properties of the nanoparticle by modulating the catalytic rate and these modulations can be reproduced *within* a given batch of nanoparticles but show strong deviations *between* batches. We must be careful in this conclusion; for how can we distinguish modulation from deviation? Are we dealing with a true but apparently fragile effect in which morphology modulates catalysis but slight changes can greatly affect the outcome, or is the catalysis rate just being influenced by a variety of synthetic and environmental factor and I am mistaking random fluctuations for a pattern? Statistically for the OT:HD:IT system at 95% confidence there is no significant difference between the catalysis rates for any of the ligand ratios. This situation does not change even at 50% confidence. The situation is only slightly better for the MHA:IT system, in which at 95% confidence the homo-ligand catalysis ligand is significantly different from all of the ripple ligand domains. What justifies accepting the hypothesis? First, the realities of nanoparticle synthesis put a limit to the number of independent syntheses that can be tested and I am left with comparing the data between two batches for each ligand system; this makes it difficult to assert strongly how much the system actually deviates which would clarify between random fluctuation and a concerted effect. We are left with observational evidence; the fact that the nanoparticles do not all obtain the same catalysis rate, despite being run with the same amount of catalyst, implies that some other factor is involved. In addition, as will be discussed below, measurement of the kinetic and thermodynamic parameters of catalysis (namely the binding constant and the attempt frequency) suggest that the monolayer is active in influencing the catalysis and that the weak effects seen in the catalysis rate are actually due to underlying modifications in the transition state of the catalyst system. Before discussing these observations we should consider the nature of deviations in nanoparticle catalysis.

4.4 Reproducibility of Catalysis Rate

It is important to discuss why the inter-batch deviations arise. We can exclude changes due to the spectrometer used to record the kinetic rates because the accuracy of the absorbance can be monitored using standard samples, which shows no changes in the observed absorbance. This leaves either the sample preparation or the nanoparticle chemistry.

Sample preparation for each catalysis trial requires three steps: buffer mixing, particle mixing, and centrifugation. Buffer mixing sets the pH of the reaction and therefore is critical to the catalytic state of the imidazole. If the pH is different between trials it can change the reactivity of the catalysis center which also will causes changes in the solubility of the nanoparticles. These two factors combined would alter the catalysis in the particles and thus lead to deviations. In addition, changes in pH affect the background catalysis rate and therefore would lead to fluctuations in the observed catalysis rate. The mixed buffers are checked using an electronic pH-meter to verify the correct pH, and it is observed that the nanoparticles reproduce even over 32 independent trials within the same synthesis batch, suggesting that the buffer mixing is not the source of deviations. Particle mixing introduces the nanoparticles into the buffer, using a concentrated stock of nanoparticles. Centrifugation removes heterogeneous clusters of nanoparticles, leaving only the soluble, homogeneous nanoparticles in solution for catalysis. The final concentration of nanoparticles left in solution is the critical factor; changes in the concentration between trials can lead to non-linear changes in the catalytic rate. Before each catalysis trial the concentration of nanoparticles (and thus of catalyst) is checked by UV-Vis absorbance. As in the buffer mixing, no deviations are seen within the same synthesis suggesting again that the particle mixing and centrifugation steps are not affecting catalysis. In general I do not suspect the sample preparation is the source of deviation.

This leaves the nanoparticle chemistry, which refers to both the monolayer morphology and the reactivity of the catalytic species, as a possible source of deviation. First, we ignore for the moment any influence of the monolayer morphology and focus only on the chemistry of the imidazole catalyst. Even if between any two synthetic batches of nanoparticles the monolayer ligand ratio and morphology is the same, if the catalytic species in each batch becomes inactivated or altered unequally (randomly), this would lead to deviations in the catalytic rate between the syntheses. The contamination with borate motivates examining this possibility, for nitrogen-boron complexes would inactivate the catalyst. Assuming that this inactivation occurs randomly and thus varies between syntheses, the resulting catalysis rates would be correspondingly attenuated and thus lead to deviation. Moreover, such differences could occur even between different ligand ratios (ripple domains) of nanoparticles and could be misinterpreted as modulation. The main arguments against this chemical inactivation are in the use of the chemical test for borates, which showed no borates present in all samples tested for catalysis, both in the nanoparticles themselves and in the extracted samples, and the improved purification procedures. This argument could be further refined in future work in which titration combined with analytical spectroscopy could be used to verify the free imidazole species; however currently we must conclude that the *presence of borates during synthesis could modify the catalysis and therefore lead to deviations between batches.*

The final source in the nanoparticle chemistry is the ligand ratio and the monolayer morphology. The ligand ratio affects both the amount of catalyst present on a nanoparticle and, because of the self-assembly nature of ripple domains, the morphology. Therefore changes in ligand ratio between syntheses could lead to changes in the catalyst concentration and the ripple domain morphology. We know that the ligand ratio does not differ by more than ~10% between syntheses. All trials are run with the same concentration of catalyst, thus eliminating the possibility of differences in catalyst affecting the final rates. If the small changes seen in the ligand ratio equate to changes in the ripple domain structure and hence deviations between syntheses, this would imply a very strong morphology effect on catalysis. This however is *not substantiated by the catalysis rates for the same synthesis that shows small changes in ligand ratio causes small changes in catalysis modulation.* The only case so far seen where this is not true is in the MHA:IT system in which going from a 1:2 MHA:IT ligand ratio to a fully homo-ligand catalyst particle has an increase in catalysis of ~2x (larger than any other single change between two successive ratios). Therefore the small ligand ratio changes are reasoned to not be the source of deviation.

Monolayer morphology also depends on the size of the nanoparticle; the radius of curvature affecting the conformational entropy, and thus the degree of phase separation in the monolayer. The direct relation between particle size, ligand composition and ligand structure is not yet established in general and not in particular for the alkanethiol-imidazole ligand systems used in this study. We make the assumption that our ligands do not differ substantially from those studied previously for ripple domain nanoparticles[4] and compare the size regime in which ripple domain particles occur to those average particle sizes obtained for the current thesis (**Figure 4.4.1**). It is seen that the current particles obtain the radii as found previously to generate ripple domain morphology. However this only supports whether the particles have ripple domains at all at the given sizes.

As ripple domain nanoparticles increase in size, simulations suggest that the each ripple stripe no longer can circumnavigate the nanoparticle and thus becomes an elongated stripe that does not close onto itself, termed a *worm-like domain*. For smaller sizes, the ripple domain gap expands, effectively generating wider ripples that, at small enough sizes, generate two, separate hemisphere spanning domains, termed *Janus (two-faced) particles*. Such changes in ligand organization can change the interactions of the monolayer with the solvent and the local, chemical environment experienced by the catalyst ligands. We could expect then changes in the catalysis rate due to size.

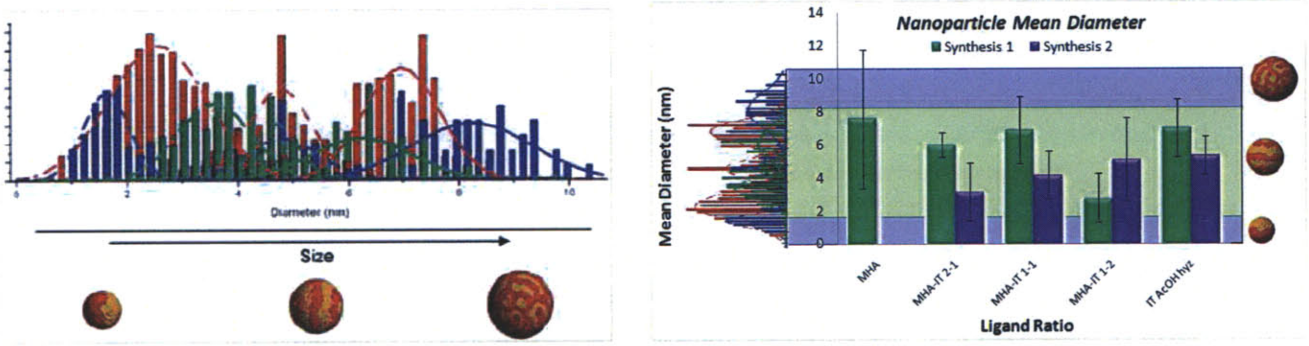

Figure 4.4.1: (Left) Population of octanethiol:mercaptobenzene nanoparticle sizes suspected of being ripple particles (**green**) and non-ripple (**blue**) for three batches of particles as determined by microscopy analysis of particles that form chains through chemical cross-linking. The cross-linking can occur only on those particles with the ripple domain. The total population of each batch is given in **(red)**. **(Right)** Using the ripple domain regime **(green)** derived from the data on the left, each MHA:IT ligand ratio average particle size exists within the expected ripple domain morphology. Green bars – synthesis 1, Purple bars- synthesis 2.

A comparison of catalytic rate as a function of average particle size for the OT:HD:IT and MHA:IT systems does not a consistent correlation (**Figure 4.4.2**), suggesting the particle size is not the

---

[4] Original ligands studied included aliphatic octanethiol, a carboxylic terminated mercapto-propionic acid, and the aromatic benzyl thiol; thus exhibiting the same structure, chemistry and charge as the three types of ligands used in this study.

source of the deviation seen between syntheses. This data can be examined in an alternative way, looking at the changes in catalytic rate for each ligand ratio between syntheses and relating this to the change in average particle size between syntheses (**Figure 4.4.3**). This analysis shows for the OT:HD:IT system that there is no clear trend between the catalysis rate and the particle size. For the MHA:IT system there is a seemingly linear trend (increase in size yields increase in catalysis), but the relation is poor. These analyses all suffer from the small amount of experimental data (only two syntheses for each particle system).

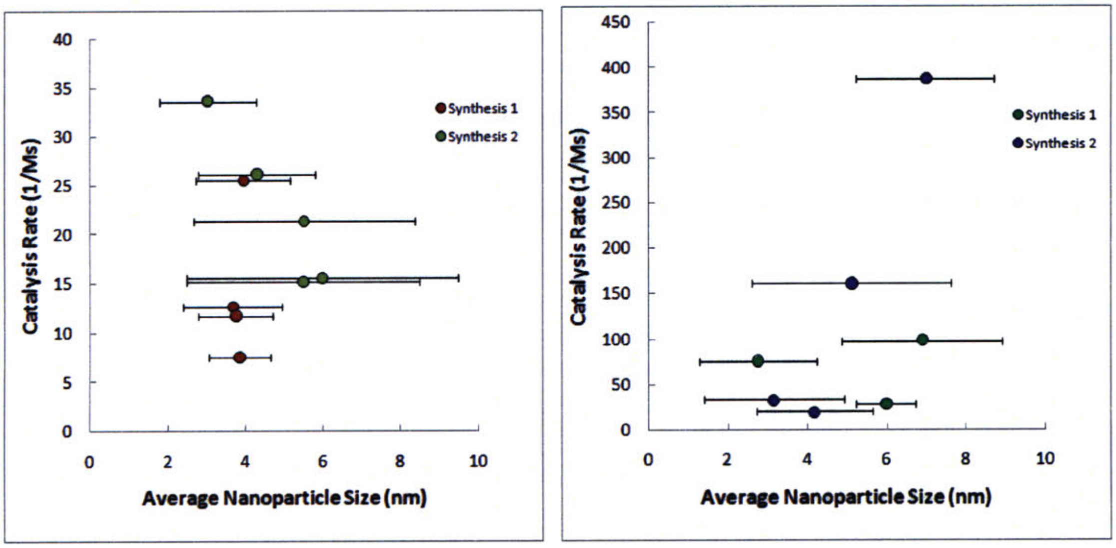

Figure 4.4.2: Catalysis rate as a function of average particle size for OT:HD:IT system **(Left)** and MHA:IT system **(Right)**. The error bars show the standard deviation of the particle sizes. **Note**: the order of the data points does not correspond in any way to the sequence of ligand ratios.

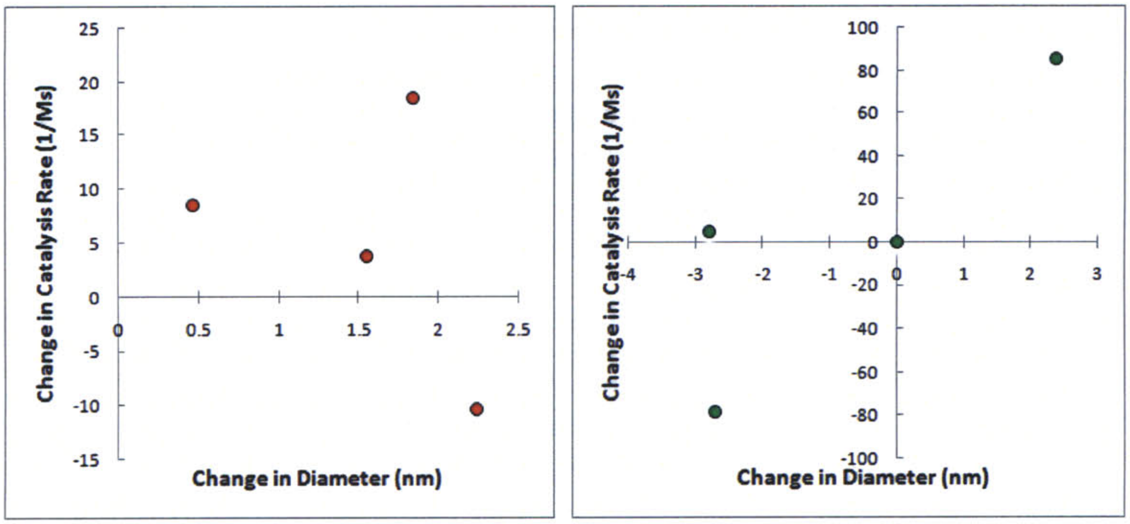

Figure 4.4.3: Change in the catalysis rate between synthesis 1 and synthesis 2 as a function of changes in average particle size for OT:HD:IT system **(Left)** and MHA:IT system **(Right)**.

In using the average particle size we are ignoring a salient feature of the nanoparticles; their poly-dispersion. All the nanoparticles exhibit a range of particle sizes as demonstrated by TEM, and these distributions do not reproduce between syntheses (in terms of average particle size, standard deviation or extrema). This distributed nature of the nanoparticle samples therefore would be expected to have a statistical, catalytic nature. Changes in the population distribution between syntheses would lead to changes in observed catalysis. Even if each particle size has only a slightly different catalysis rate, the blending of different populations of such particles would generate a catalysis rate that could fluctuate between two different distributions. The inherent, statistical behavior we are proposing for a nanoparticle population should be contrasted with catalyst systems such as organometallic complexes or biological enzymes which are well-defined and identical within a population. These well-defined catalysts are expected to exhibit a very small deviation around the overall catalytic mean (when run under identical conditions) due to consistency in structure. In analogy, the characterization of nanoparticle catalysts to well-defined catalysts is the same situation as that of a polymer to a single molecule; the variation in the polymer requires a statistical approach whereas the single molecule can be characterized fully by a set of constant factors.

It is difficult currently to synthesize mixed-ligand polar / non-polar nanoparticle species of a single crystal morphology and molecular structure in the ripple domain regime. In approaching this study, it was taken implicitly that the deviations in the particle populations, whether experimental or fundamental in nature, were small compared to the measured catalysis rate. Now it is clear that *the deviations in the nanoparticle catalysis rates are the same magnitudes as the means and* *this implies that to fully characterize the catalysis of the ripple particles that the statistics from several synthetic trials must be collected.* If the catalytic rate of a given population of nanoparticles is considered a distribution, then the current data set gives only two points within this distribution; this cannot define the statistics fully and therefore additional syntheses are needed. The catalytic rates and efficiencies deviate much more than the surface energy seen in the original study, suggesting catalysis is more sensitive to either the particle preparation and/or molecular structure.

Based on the wide deviation seen in the data, it was suggested a "bootstrap" calculation be performed to get a sense of the spread in the catalytic rate. The bootstrap calculation uses the current, available data to estimate the range of possible values the final catalysis rate would be expected to yield in order to gain an understanding of the statistics of the system. Using the rough statistics obtained from the two syntheses, a calculation was made of the catalytic rate spread based on deviations in five parameters: the average diameter, the organic portion, the ligand ratio, the measured absorbance of the nanoparticles, and the observed catalytic rate. For each parameter, a normal distribution was assumed and the mean and standard deviation calculated from the experimental data. Using a random number generator, three sets of 2,000 catalytic rate calculations were made. The generated distributions were fit to a lognormal and the expectation value and deviation calculated (see **Figure 4.4.4**). For the calculation the MHA-IT 1:1 synthesis 2 data was used. From this, for the catalytic rate, the median ~ 48.41 +/- 1.50 $1/sM_{cat}$, mean ~ 65.11 +/- 3.16 $1/sM_{cat}$, and deviation ~ 59.03 +/- 5.18 $1/sM_{cat}$. This is comparable to the experimental mean catalyst rate of 58.99 $1/sM_{cat}$, with deviation of 55.34 $1/sM_{cat}$. Comparing this calculation to the experimental data it can be seen, as already noted, that the spread in the catalytic rate covers the observed rates seen in the ripple domain ligand ratios.

How do these factors affect the tentative acceptance of the hypothesis? The reproducibility of the modulation within a synthesis suggests that the chemistry of the monolayers is stable and the experimental conditions executed reliably, allowing the conclusions the *monolayer morphology affects the catalysis rate*. However the deviations between syntheses suggest that something has changed fundamentally in the chemistry. We have reasoned that this change is either in chemical negation of the catalysis by borates or, we conjecture as more likely, the distributed nature of the nanoparticle sizes (and hence ripple domain morphologies). The current data cannot quantify the degree of deviation or link specifically these factors to the deviations; however this problem is actually an extension of the original hypothesis, asking to what extend *changes* in the monolayer morphology *affect* the observed modulation.

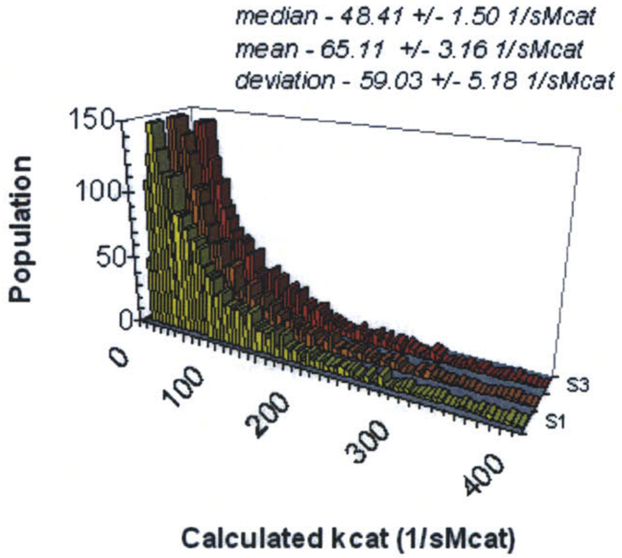

Figure 4.4.4: Plot of three, calculated catalytic rate distributions generated for the MHA:IT 1:1 ligand ratio. The catalytic rate was calculated by randomly selecting values from normal distributions of the nanoparticle diameter, percentage of organic material, percentage composition of catalyst, measured absorbance and experimentally observed catalysis rate. The normal distributions of these parameters were generated using the experimental data for the MHA:IT 1:1 particles. The median, mean and deviations values are the average of the three calculations.

4.5 Experimental Error

The one-phase synthesis method used to produce the catalytic nanoparticles is a straightforward method of synthesizing homo-ligand, aliphatic thiol nanoparticles, and by extension work in my lab, to mixed-ligand systems using polar and non-polar ligands. It has been reported and observed in-house that more structurally complicated and/or polar ligands can modify the yield, quality, dispersity and even success of a one-phase synthesis. Several factors of the synthesis are crucial, including purity of the ethanol, the water content, the rate of stirring, the water-absorption in the sodium borohydride (referred to as its *freshness*), the method of cooling the reaction, and the rate of addition of borohydride solution. This last factor is of particular importance because the rate at which the reducing reagent (sodium borohydride) is added to the reaction controls the nucleation and growth kinetics of the nanoparticles, and thus their final monolayer composition. Changes in the addition rate, especially at the critical regime between when the seed nuclei cross the critical growth radius and begin accumulating mass, can lead to large changes in the nanoparticle size distribution.

How sensitive is a synthesis to slight (unaccounted or unobserved) changes in protocol? As was seen, the fluctuations in the mean particle size are ~1.0-1.8 nm (~20-50% of the mean) for a given series of syntheses, in which each particle was in a separate vessel with independent operations, but following the same procedure and within the same time period as the other particles in the series. This suggests that the important factors such as cooling and addition of reducing agent were not substantially different within these syntheses. Strangely, the only series that deviates significantly is MHA:IT synthesis 2 which was performed on the same day with all particles being synthesized within minutes of each other. The material analysis conducted on the particles accounts in some measure for the size dispersion and changes in monolayer composition but introduces its own source of deviation, as will be discussed.

The deviations in the average particle size are larger between any two syntheses which are separated at least by two months for both the systems. This implies a factor in the syntheses changes within a monthly period, a possible source being the reagents: ethanol, gold salt, sodium borohydride, and the ligands. NMR analysis of the ligands showed no composition change, arguing against the filler or catalyst ligands. There is little data on the effect of solvent or gold salt purity, although the presence of oxygen in these reagents can lead to thiol oxidation and reduced SAM formation, leading to larger particles that aggregate easier [1]; however the stability of the particles suggests against thiol oxidation in the current work.

The freshness of the sodium borohydride is known to be crucial to the one-phase synthesis. Sodium borohydride is hygroscopic and will form nonreactive hydrates overtime unless sealed from atmospheric moisture. These hydrates cannot reduce the metal ions to metal atoms and may interfere with the nucleation / growth kinetics as suggested by the large poly-dispersities and poor yields seen when "poor" sodium borohydride is used. In our lab, we have found that borohydride freshness will affect the dispersity and solubility of particles, and because of this, all syntheses were prepared with new sodium borohydride within one to two weeks of purchase. No method was used to quantify the integrity of sodium borohydride.

4.6 Kinetics of Catalysis: Binding Constants

The binding constant, K, relates indirectly to the lifetime of a putative intermediate between the substrate and nanoparticle that is necessary to initiate catalysis. A larger binding constant indicates a weaker intermediate. The current work used the Michaelis-Menten formulation of the binding constant (see *Appendix A* for details) since the nanoparticle system operates in a solution based, homogeneous catalytic reaction. The most important observation from the data is that the MHA:IT 1:2 particles have a lower binding constant than the other ripple systems and the homo-ligand catalyst particles. This suggests that the monolayer of these particles can stabilize the intermediate; however this does not imply superior catalysis, as demonstrated by the catalytic rate. In this case it appears the 1:2 monolayer is more capable of capturing the substrate but that reaction of the bound state is still slower compared to the homo-ligand catalyst. In this case, we can see a separation of effects: the monolayer determines the physical absorption of the substrate, but the catalyst – in particular the concentration of catalyst – controls the final reactivity and thus rate of catalysis. These observations suggest that, assuming the monolayer affect on the binding constant is real, that a better catalyst species must be used that can take advantage of the higher binding capacity.

Although the monolayer morphology affects the binding constant, it is not clear what factor of the structure modifies this binding. In considering the ripple domain, the unique feature is the gap formed by the two ligand phases, which presents a local environment that can differ physically and chemical from the surrounding solvent. It is possible that changing the ligand ratio, which changes the average gap width, produces a compartment which accommodates the substrate. For future work it would be interesting to probe the *specificity* of the monolayers, using the binding constant and catalysis rates of structurally similar substrates as a probe what can be accommodated in the monolayer.

4.7 Thermodynamics: Activation Energy

It was observed that the activation energy showed significant reproducibility between syntheses for the MHA:IT system. The activation energy was found to range 12-21 kJ/mol, 18 kJ/mol mean, less than half the value found for the background water catalysis, 50 kJ/mol. The consistency across the ligand ratios and syntheses suggests that *the activation energy is not a probe of the monolayer structure but rather of the substrate-catalyst-solvent system itself*, giving evidence that the mixture of ligands and their morphology are not affecting the catalytic reaction directly. It would be interesting to know if the free form ligand yielded the same activation energy; however, this cannot be done at present due to insolubility of the studied catalyst ligand in pure water.

4.8 Thermodynamics: Attempt Frequency

It was observed that the attempt frequency magnitude changed substantially between the two syntheses for MHA:IT. However, if the two sets of data are normalized to the maximum attempt frequency, it is observed that the attempt frequency follows a trend with monolayer morphology. We cannot account for the difference in magnitude, especially in that it is the same across each synthesis. However the fact the same trend in catalysis appears for each synthesis gives evidence that the monolayer is affecting the attempt frequency. Furthermore, we observe that the MHA:IT 1:2 nanoparticles have the highest attempt frequency of the ripple domain particles, implying that substrates in the 1:2 MHA:IT monolayer interact the most with the catalyst ligand. This observation is in line with the lower binding constant, providing further evidence that the monolayer provides a physical environment in which the substrate becomes bound and able to interact with the catalyst.

If the MHA:IT 1:2 nanoparticles have enhanced binding sites and substrate/catalyst interactions, why are they poorer catalysts (in terms of catalytic rate) than the homo-ligand catalyst particles? The answer lies in the combination of activation energy and attempt frequency; although MHA:IT 1:2 has a higher attempt frequency, its activation energy differs from the homo-ligand particle by ~ +3.5 kJ/mol. Thus the homo-ligand particle requires less energy to begin the reaction, and since the attempt frequencies of the two particles are close, the overall effect the homo-ligand catalyst rate is greater by a factor ~ 2-3 times MHA:IT 1:2. This reduced energy barrier is reasoned to be due to the high, local concentration of catalyst molecules. We observe that the MHA:IT 2:1 nanoparticle has a low activation energy barrier as well, although it is a poor catalyst due to its inability to form a good binding site and its very low attempt frequency. We reason that this is due to the charged carboxylic acids which might produce a double layer at the monolayer surface that is difficult for substrates to penetrate. However this suggests that if carboxylic acids could be buried into the ripple domain monolayer with the imidazole base, in particular in the 1:2 filler:catalyst ligand ratio, that an enhanced catalytic rate could be obtained.

We must note that the attempt frequency is very sensitive to both experimental conditions and analysis, and open to large deviations as have been recorded [2-4], and is seen in the large difference in magnitude between syntheses. *Therefore we only accept as a new hypothesis, based on the current data, that the monolayer morphology influences the catalytic rate.* Nevertheless, it is interesting to consider the physics underlying the attempt frequency and how it could link the ripple structure to catalysis.

Transition state theory states that in order for a molecule to react it must overcome an energy barrier. This energy barrier is, structurally, the assumption of a high energy transition state (denoted #). To obtain this state the molecule must acquire an amount of energy ΔE; energy used to form the unstable, reactive transition state. From statistical mechanics the transition state rate, $k^{\#}$ (which is the observed rate since it is the limiting process) can be written as [3]:

$$k^{\#} = \frac{k_b T}{h} \frac{z_o^{\#}}{z} e^{-\frac{\Delta E}{k_b T}}$$ **Equation 4.8.1**

With k_b = Boltzmann's constant, h = Planck's constant, T = temperature, z = the partition function of the molecule, and $z_0^{\#}$ = the partition function of the transition state at its ground state [3]. Each partition function is a product of the various degrees of freedom (energy storage) available in the molecule, translation, rotation, vibration and electronic states:

$$z = z_{translational} z_{rotational} z_{vibrational} z_{electronic}$$ **Equation 4.8.2**

Comparing the transition state equation to the Arrhenius equation, the attempt frequency is seen as:

$$v_{atp}^{\#} = \frac{k_b T}{h} \frac{z_o^{\#}}{z}$$ **Equation 4.8.3**

The quotient of partition functions describes a probability – relating the number of reaction promoting conformations (transition state conformations) to the total available to the molecule. This probability can be linked to entropy through statistical mechanics [2,3]:

$$S_0^{\#} - S = \Delta S_0^{\#} = R \ln\left(\frac{z_0^{\#}}{z}\right) - R$$ **Equation 4.8.4**

Where $\Delta S_o^{\#}$ is the change in entropy between the molecule (S) and its ground state transition state ($S_0^{\#}$).

The attempt frequency now reads [3]:

$$v_{atp}^{\#} = \frac{k_b T e}{h} e^{\frac{\Delta S_0^{\#}}{R}}$$ **Equation 4.8.5**

We observe that the attempt frequency is determined by the entropy change between the molecule and its transition state. Highly structured transition states have negative $\Delta S_o^{\#}$ and thus lower frequencies. Typical molecular attempt frequencies for bi-molecular, homogeneous catalytic reactions range between 10^9 to 10^{17} sec^{-1} [3]. The transition state's entropy change is affected both by the type of reaction (which is fixed by the chemistry) and by the energy levels of the transition state's conformations. It is this latter term which is affected by local structure; if the local molecular structure, such as in a catalyst, lowers the energy of the transition state conformations, the quotient of partition functions increases as does the attempt frequency – the probability of forming a reactive transition state has increased and the reaction speeds up.

The activation energy and attempt frequency are not independent of each other; changes in the stabilization of the transition state can affect both factors. However, we are led to conjecture that the ripple domain is affecting the attempt frequency dominantly, and we reason how this link could be established. The ripple domain morphology could shift the conformations allowed to the substrates by both constraining motion within the ripple gap and by providing a local environment which favors certain interactions (such as hydrophobic) that restricts which conformations are low energy, and in effect, the entropy of the transition state. This is a conjecture, but it follows closely the original reasoning used to propose the hypothesis – that the monolayer microstructure could enforce changes in conformation of the substrate, much as was interpreted for changes in the solvent structure for the surface energy.

As with catalysis rate, it appears the attempt frequency of the nanoparticles can be captured best by understanding their statistical distributions, and this requires measuring several synthetic batches. In addition, the resolution in the Arrhenius equation improves with the temperature range and suggests expanding the experimental procedure to the largest ΔT possible.

4.9 Centrifugation Solubility

Ultracentrifugation was used to isolate and purify nanoparticles as well, to remove heterogeneous aggregates of nanoparticles and to measure the relative solubility of the nanoparticles. The use of ultracentrifugation (5,000 RPM) imposes its own conditions on what is considered "soluble". At the given speeds the applied g-force is ~ 2,040 g which is far greater than is experienced by the particles if allowed to precipitate under standard gravity. Ultracentrifugation greatly expedited experiments that would otherwise take weeks to prepare, but how the process affects the observed solubility must be considered. The OT:IT system solubility shows a stark, inter-batch irreproducibility, though it demonstrates the same modulated trend. The OT synthesis 1 particles have, on average, smaller diameters compared to synthesis 2 (5.32 nm and 3.80 nm average). This leads to the average mass of a single, synthesis 1 particle to be smaller than that of a synthesis 2 particle by a factor of ~ 3, implying that the magnitude of the centrifugal force will be only marginally somewhat stronger on the synthesis 2 particle, compared to synthesis 1.

The OT:IT synthesis 2 particles have on average about twice the ligands of synthesis 1 particles in their monolayer; however the average volume densities are comparatively close, 5.5 g/mL (synthesis 1) and 8.1 g/mL (synthesis 2), suggesting the particles have on average the same effective mass and thus would experience the same average, centrifugal force. These factors cannot account for the absolute difference in solubility observed. The centrifugation process does eliminate any clusters or aggregations of particles that exist in solution. The synthesis 1 solubility was measured approximately one month from its time of synthesis, and synthesis 2 approximately two weeks from it synthesis. Given the tendency for aggregation mentioned before, it is likely that the OT:IT synthesis 1 particles aggregated more and this is reflected in the overall lower solubility. The fact that the homo-ligand catalyst particle suffers the same as the ripple domain ratios follows this reasoning. No difference in the NMR or the crystallization behavior of the IT molecules used for syntheses 1 and 2 suggests no difference in the chemical composition of the ligand used.

4.10 Relation of Centrifuge Solubility and Catalytic Rate

It was observed during the experimental work an apparent correlation between the solubility of the nanoparticles and the catalytic rate; the lower the solubility the higher the catalysis. This fit, conceptually, into the idea that the more ordered the ripple domain, the stronger the salvation shell ordering, and hence the less soluble the particles but the more reactive the catalyst sites. The quantitative values of the catalytic rate and centrifuge solubility cannot be directly compared between OT:IT and MHA:IT, but their trends can be compared if the values are normalized. When these normalized values are compared it is seen that there is no statistical correlation between solubility and catalytic rate (see **Figure 4.10.1**), the correlation factor being only $r = 0.015$[5]. The situation does not change substantially if the two systems are treated separately, $r = -0.039$ for OT:IT and $r = 0.35$ for MHA:IT. If the homo-ligand catalyst is removed from the data the correlation becomes $r = -0.27$, which follows the observed notion that increasing solubility gives decreasing catalysis. The poor correlation factors suggest that there is no link between solubility and catalysis rate, which further suggests the mechanism by which the ripple domain influences the surface energy (and hence solubility) is not the same, or is contra-active, to that which affects catalysis.

---

[5] A correlation factor of $r = 1$ means the data is positively correlated and $r = -1$ means the data is negatively correlated. For $r = 0$ there is no correlation. For a 90% confidence in correlation, require $r = 0.9$ or -0.9.

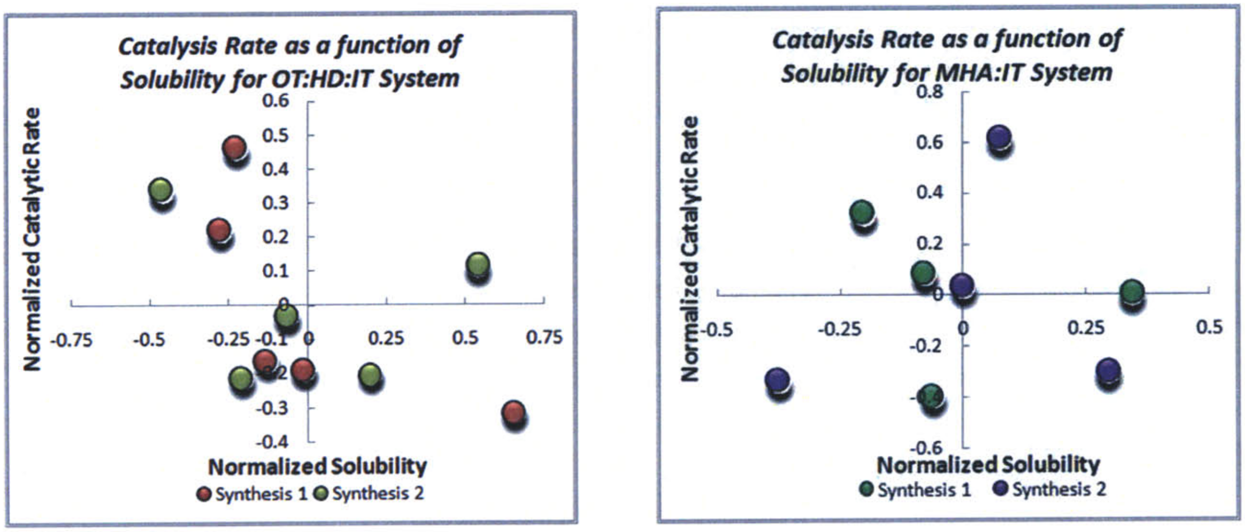

Figure 4.10.1: Scatter plot of *difference from the group mean* in the normalized catalytic rate and normalized centrifuged solubility for OT:HD:IT system **(Left)** and MHA:IT system **(Right)**.

4.11 Thermalgravimetric Analysis and Monolayer Coverage

TGA was used to quantify the average amount of ligand present in the nanoparticle samples. The importance of this quantification is to determine the amount of catalyst presence during a reaction, which determines the final catalytic rate that was calculated. A first question regards the assumption that the decomposed material, the *organic portion*, quantifies the actual ligand monolayer. It is known organic ligands decompose at 200-300 ^{0}C, and that they can desorb from an organic surface between 200-400 ^{0}C [5-7]. I do not expect that molecular rearrangement of the organic substances would survive up to 600^{0}C. Mass-spectroscopy was attempted to verify the decomposition species, but was not successful with the small particle samples available. It is possible that the organic ligands form a carbon film, equivalent to an ash, which explains the very slow, slight decomposition tail seen above 500 ^{0}C; however, the major decomposition events are seen in the transitions at ~ 250 ^{0}C and ~ 400 ^{0}C.

Using thermogravimetric data, the percentage of catalyst in the monolayer, and particle distributions obtained from the TEM images, and assuming these distributions capture the population density of each particle correctly, we can estimate the *percent coverage of organic molecules*, Γ (ligands/gold atom) [7]. The coverage allows us to interpret the thermal data in a more physical, real manner, since it demonstrates how close-packed the nanoparticle monolayer is. We estimate the coverage using a formula derived by Murray and coworkers [7]:

$$\Gamma = \frac{\chi_{org} \frac{4}{3} \pi r^3 \rho_{Au} AW_{Au}}{4\pi (r - r_{Au})^2 \rho_{HCP} MW_{avg} (1 - \chi_{org})} \qquad \textbf{Equation 4.11.1}$$

With r = average (expected) radius of nanoparticle (nm), χ_{org} = organic portion, ρ_{Au} = atomic density of gold (58.01 atoms/nm^3), AW_{Au} = atomic weight of gold (g/atom), r_{Au} = atomic radius of gold (0.145 nm), ρ_{HCP} = density of surface gold atoms on a hexagonal close-packed lattice (13.88 atoms/nm^2), and MW_{avg} = average molecular weight of monolayer calculated from the percentage of catalyst.

The percent coverage ranges between 0.40 and 0.65, as seen in **Figure 4.11.1**. These values are in line with the close-packed monolayers seen on nanoparticles, and imply that the nanoparticle has a higher degree of close packing than on a flat SAM [5,7,8]. For the MHA-IT system we see that, except for MHA-IT 2-1, that the values are fairly consistent for the particles. The discrepancy in MHA-IT 2-1 stems from the large difference in particle size between the first and second synthesis; as predicted by previous work the smaller nanoparticle (synthesis 1) has a tighter packed shell [7]. For the OT:HD:IT system, there is a systematic discrepancy between the first and second synthesis, which can be seen in the original TGA data. The calculation implies the first synthesis particles have a more tightly packed monolayer, stemming again from the fact these particles have a smaller core compared to the second synthesis. The apparent discrepancy in the TGA, therefore, is proposed to be due to differences in the as-synthesized particle distributions. The more tightly packed monolayer might explain the reduced centrifuge solubility seen for synthesis 1, implying the more tightly packed monolayer hindered the shell from interacting with solvent, either through forcing a tighter hydration shell that cannot interact with the surrounding solvent, or by limiting the conformational freedom of the monolayer.

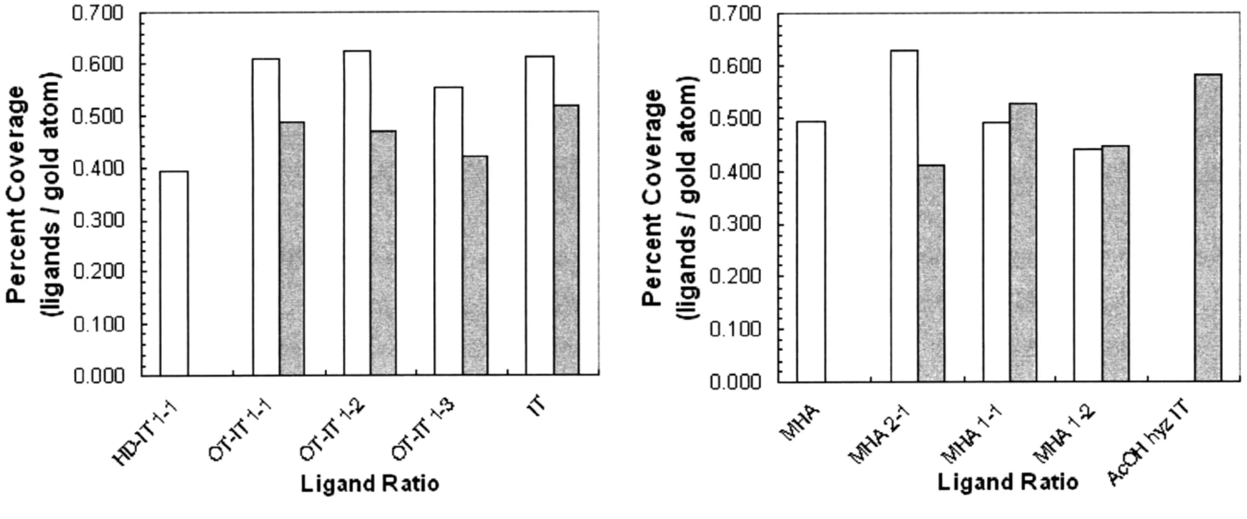

Figure 4.11.1: Calculated percent coverage of ligands to surface gold atoms for the OT:HD:IT system **(Left)** and MHA:IT system **(Right)**. Synthesis 1 – white bars, synthesis 2 – gray bars. The MES hydrolyzed homo-ligand catalyst particles were not analyzed for the MHA:IT system due to their lack of catalytic activity.

4.12 Particle Distributions

The particle distributions obtained from TEM estimate the distribution of nanoparticle core radii. The analysis used for the particles has a rough cut off around ~ 1.5 – 2 nm. This is due to a combination of resolution obtained at the magnifications used in the TEM images and the Image-J software analysis. A compromise was struck between images that obtained a large enough population of particles to count, a resolution acceptable for analysis, and a number of pictures which could be analyzed in a reasonable time. Magnifications of 27 kx to 50 kx were used to obtain acceptable populations, but small particles are lost to the noise level of the background. In analyzing the particles, a threshold method is used which partitions images into black (nanoparticle core) and white (background). In doing so some of the background noise is captured as "particle type" and in order to eliminate this from the analysis a particle rejection threshold of ~ 20 pixels is used. This pixel range is within the ~ 1.0 nm particle range. These concerns necessitated the log-normal distribution[6] fit in order to recapture the initial tail, assuming that these smaller particles exist and have been lost by the imaging process. It should be noted that clusters (< 500 Au atoms) cannot be seen or accounted for in the current analysis, but their small ligand population is assumed to not contribute substantial to the observed catalytic rate due

---

[6] The lognormal distribution is used as it gives the best fit, in terms of highest R^2 value, to the particle distributions.

to the low number of catalyst molecules and small population. The log normal is used to fit particle distributions seen under nucleation / growth conditions.

The fact that some particles have high count populations (notably in the OT-IT synthesis 1 and MHA-IT synthesis 2) is a consequence of aggregation. For those particles with a lower count population, a high degree of particle aggregation was observed; only those particles that were free from the aggregates could be counted by the software. A comparison of the particles in the aggregates and in the free range was made by hand to check that the aggregates were not composed of different size particles and thus skewing the distribution. The observed aggregation for the MHA-IT system is due to the need to deposit particles in a mixed ethanol : water system to avoid destroying the carbon film by water tension. The ethanol causes some aggregation in the particles, as well as the drying effect of the residual water. For the OT:IT system it is not clear what causes the aggregation, although the drying effect due to condensed water is possible.

The 1:1 MHA:IT synthesis 1 distribution is bi-modal.. Larger particles, in the 10-12 nm diameter regime, are seen in this batch. Looking at only the lower radii peak shows a close agreement with the other particles in the series. The presence of these particles suggests that an unaccounted for change in the dropping rate generated two populations of nuclei, the earlier one having more opportunity to grow large and aggregate.

For the OT:IT system, within a given synthesis the particles exhibit roughly the same distributions, however, between syntheses they are not equivalent. For MHA:IT there is no significant equivalence within or between the syntheses. This demonstrates a general problem of reproducibility in nanoparticle synthesis that is found in the one-phase methodology and in particular for mixed-ligand polar-non-polar nanoparticles. The consequences of this will be addressed below.

4.13 Borates

The evidence of borates in the nanoparticles comes from the chromogenic reaction of NBA and ECA and the effect this has on the observed kinetics of the Knoevengel Condensation (K-con). It is known that nitrogen, through an sp_2 orbital, can form an ionic bond with electron-deficient boron [9-12]. These complexes can be very strong, such as t-butyl amine borane complexes which are air stable and can be stored indefinitely [12]. The imidazole-boron complex is mildly strong, but can be broken by acid assisted hydrolysis in which protonation of the amine generates a charged intermediate which actives the boron atom to condensate with water [10,11]. For the catalyst ligand used, only the 3N imine (the reactive group) is available for complex, and the aromatic delocalization in the heterocycle with this imine accounts for its weaker bonding to boron.

It was not considered in the planning of the experimental work that a nitrogen-boron complex could form. The presence of borate complexes has been found in nanoparticles synthesized with sodium borohydride. Thorough washing with water was considered adequate for removal of these mineralites, and this is evidenced by the disappearance of the NBA ECA coloration with water washing during centrifuge purification. However, the borate complex is not a freely dissociable crystal or secondary complex; the nitrogen-boron bond must be broken, and hence this complex remained despite the washing cycles.

In the K-con reaction, the electron rich, Lewis-base type borate can abstract a proton from the carbon center, facilitating the condensation and giving the false-positive seen in the kinetic data. From the experimental data we see that the borates are excellent reagents for initiating the condensation reaction, but does the borate also affect the dinitro-phenyl acetate hydrolysis reaction which is the major focus of this study? From the extraction experiments it is seen that any borates in solution do not contribute to catalysis, which leaves only the borate complexes within the monolayer. For the MHA:IT system this is straight forward; the fact that hydrolyzed nanoparticles show no difference in catalytic rate compared to non-hydrolyze supports that the borate is not effecting either the chemistry or the density of catalysts.

For the OT:IT, HD:IT systems this is not straight forward because there is no data of the before and after hydrolysis reaction. The extracts from these particles show only the background water hydrolysis suggesting that the borate, if present, has no direct consequence on the catalysis. Additionally, when a solution of sodium borohydride at the synthetic molarity is run in a catalyst trial no catalysis is seen (see **Figure 4.13.1**). However, borate complexes with the imidazoles could have reduced the general density of reactive group available for catalysis. This offers an alternative explanation for the high deviation and equal overall mean of the catalytic rates seen in the OT:IT and HD:IT syntheses; the rates fluctuated due to variations in the amount of borate complexes formed, and the overall mean is due to the weak catalytic capacity of either a few remaining free imidazoles or a borate-imidazole complex. This would explain differences seen between the OT:IT (ethanol : water) and MHA:IT (only water) systems. The formation of imidazole borate complexes with a borohydride is difficult in open atmosphere, in the presence of water (trace in the ethanol) due to competing oxidation of boron. Further work is necessary to clarify the role of the borate in the OT:IT system.

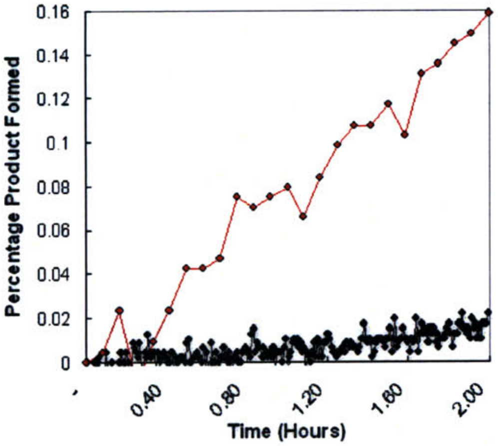

Figure 4.13.1: Kinetic curves demonstrating the non-activity of borates, black dots, compared to an example nanoparticle catalyst OT:IT 1:2, red dots. The OT:IT 1:2 nanoparticle catalyst gives the lowest catalytic rate of the series. The borate kinetic curve is comparable to the background water catalysis curve.

Returning to the case of the homo-ligand catalyst particles, IT, it is observed there is a physical effect on the solubility and catalysis rate due to *hydrolysis*, but given the evidence, it is not certain that it is an effect of borates. It is possible that the imidazole monolayers cause particle aggregation during the synthesis reaction which can only be disrupted with applied heat and agitation. Other nanoparticles, particularly homo-ligand and mixed ligand particles with aliphatic thiols and carboxylic acids, have demonstrated this behavior in our group. The mixed ligand MHA:IT particles cannot resolve this question because of the presence of carboxylic acid terminals which are strongly polar and can "pull" the particles into solution.

4.14 Knoevengel Condensation Catalysis

The poor response of the Kcon reaction, even after the removal of suspected borates, presents a new challenge. Considering the 3N imine is pKa ~ 6.6 – 6.8, while that of ethyl cyano-acetate is ~ 13 demonstrates that the current catalyst is not a strong enough base to effectively deprotonate the activated acid. Using the IT catalyst made the assumption that the local environment of the monolayer would either increase the basicity of the imine (raise its pKa), or induce chemical changes in the acid that would increase its acidity (lower its pKa). The fact that almost no catalysis is observed suggests that neither of these phenomena occurred appreciably. Application of the imidazole catalyst to the Kcon represents an attempt to use an already established system in a new chemistry. Its performance suggests that a new catalyst ligand with a higher pKa (stronger base) must be used, an obvious choice being a piperiazine or pyridine derivative. An alternative concept would be to change the filler ligand to produce a local environment that favors deprotonation. The testing of the Kcon reaction is important to this study in revealing the presence of borates and developing a simple method for their detection in solution.

Chapter 4 References

1. Love JC, E.L., Kriebel JK, Nuzzo RG, Whitesides GM. Self-Assembled Monolayers of Thiolates on Metals as a Form of Nanotechnology. *Chemical Review* **105**, 1103-1169 (2005).
2. Arnaut L, F.S., Burrows H, (ed.) *Chemical Kinetics - From Molecular Structure to Chemical Reactivity*, (Elsevier, Amsterdam, 2007).
3. Chorkendorff I, N.J. *Concepts of Modern Catalysis and Kinetics*, (Wiley-VCH, 2003).
4. Bugg T. *Introduction to Enzyme and Coenzyme Chemistry*, (Blackwell Publishing, Oxford, 2004).
5. Hostetler, M.J. et al. Alkanethiolate Gold Cluster Molecules with Core Diameters from 1.5 to 5.2 nm: Core and Monolayer Properties as a Function of Core Size. *Langmuir* **14**, 17-30 (1998).
6. Templeton, A.C., Wuelfing, W.P. & Murray, R.W. Monolayer-Protected Cluster Molecules. *Accounts of Chemical Research* **33**, 27-36 (2000).
7. Terrill, R.H. et al. Monolayers in Three Dimensions: NMR, SAXS, Thermal and Electron Hopping Studies of Alkanethiol Stabilized Gold Clusters. *Journal of the American Chemical Society* **117**, 12537-12548 (1995).
8. Hostetler, M.J., Stokes, J.J. & Murray, R.W. Infrared Spectrosocopy of Three-Dimensional Self-Assembled Monolayers: N-Alkanethiolate Monolayers on Gold Cluster Compounds. *Langmuir* **12**, 3604-3612 (1996).
9. Carey FA, S.R. *Advanced Organic Chemistry*, (Springer, New York, 2007).
10. Bailey PD. *Organonitrogen Chemistry*, (Oxford University Press, Oxford, 1996).
11. Sidgwick, N.V. *The Organic Chemistry of Nitrogen*, (Clarendon Press, Oxford, 1966).
12. Matsumi N, M.A., Sakamoto K, Ohno H,. Liquid Imidazole-Borane Complex. *Chemical Communications*, 4557-4559 (2005).

CHAPTER 5 - CONCLUSIONS

5.1 Conclusions

I have investigated in this thesis if ripple domain nanoparticles exhibit *modulation* of the catalytic rate with respect to a non-ripple, homo-ligand catalyst particle. The work demonstrates that modulation can be seen in ripple nanoparticles, however this modulation deviates strongly between nanoparticle batches. The effect of modulation, either enhancement or attenuation with respect to the non-ripple particles, depends on the type of ligands chosen and the reaction environment. Gold nanoparticles coated in two alkanethiol ligands, in which one of the ligands contains a catalytic imidazole group, generate the ripple domain morphology by self-assembly. This morphology involves phase-separation of the two ligands to form stripes with well defined widths and depths (difference in the lengths of the two ligands). The width of the stripes can be adjusted by changing the ratio of the two ligands, allowing different ripple domains to be tested. I have tested two systems of ligands: (1) 1-octanethiol *or* 1-hexadecanethiol (OT:HD) or (2) 16-mercapto-hexadecanoic acid (MHA) with the catalyst imidazole ligand (IT). The OT:HD:IT system is soluble in aqueous ethanol solutions and shows ripple domain nanoparticles with enhanced and attenuated catalysis rates. The MHA:IT system is soluble in water, and all the ripple domains show attenuation compared to the non-ripple homo-ligand catalyst particles. My results cannot currently confirm the idea that the monolayer morphology can affect the local environment of the catalyst ligand and its interactions with the solvent and substrate, and thus influence catalytic activity, however they provide a basis of understanding for further investigation, opening the way for exploring interfacial ordering as a means to catalysis.

The MHA:IT system was further tested for changes in the kinetic and thermodynamic properties of the particles as a function of ripple structure. The substrate binding energy was seen to change with ripple domain structure, with a 1:2 MHA:IT ligand ratio generating a lower binding constant (stronger binding intermediate) compared to the homo-ligand particles (300 μM versus 450 μM), suggesting the ripple morphology produces a structure that is better able to contain and stabilize the substrate. Furthermore, experiment found the presence of ripple domain nanoparticles can affect the Arrhenius attempt frequency which describes the thermally activated chemical transition. Whereas the activation energy was changed very little (+/- 8 kJ/mol ~20% maximum) the attempt frequency changed by over 90% between 2:1 and 1:2 MHA:IT ligand ratios. This supports the idea that the monolayer is affecting the ability of the substrate to bind and interact with the catalyst and suggests better catalysts could be designed that control independently the activation energy and attempt frequency for maximum activity.

Experiments to extend the catalyst systems to the synthetic reaction of the Knoevengel Condensation did not work, due to difficulties in the pK_a of the systems. However, the work demonstrated an easy method for qualitatively determining the presence of borates in the nanoparticle solutions, allowing determination of particle purity and confirming that borate minerals can form in nanoparticles during synthesis.

5.2 Future Work

5.2.1 Inter-Batch Reproducibility

It was observed that while the nanoparticles demonstrated good reproducibility in catalysis rate within a given synthetic batch, the reproducibility between batches showed deviations on the same order of the means. This suggests the modulation behavior is sensitive to the structure of the nanoparticles, in particular to the means of synthesis, the particle sizes, and the ligand ratio. In addition, the presence of borates can influence the catalysis observed by forming nitrogen-boron complexes which inactivate the catalyst. The inherent poly-dispersity of the particles generated by the synthetic method (which was required in order to obtain the ripple domain state) is reasoned to give nanoparticles with inherent dispersion in catalytic properties. This suggests that to better quantify nanoparticle catalysts, and the effect of morphology in the nanoparticle monolayer on catalysis, that either (1) several synthetic batches must be tested and the distribution of catalysis rate determined to fully quantify the effect of morphology or (2) particles with more mono-disperse properties are generated.

The large deviations in the inter-batch catalysis rates between ligand ratios are hypothesized to be due to the poly-dispersity in the particle population. To test this, a series of syntheses for each ligand ratio could be prepared and the catalytic rates for each of these syntheses tested. At the given level of deviation, it is estimated 20-40 syntheses must be run to acquire a 90% confidence of difference in catalysis rates at the current resolution of the experiments (+/- 0.1 1/Ms). Such a large number of syntheses is both time and money consuming, suggesting that to carry out such an experiment requires developing a new synthetic method of making several, micro-scale batches of particles. In this proposed method, the nanoparticle synthesis is scaled down from 100-200 mL to 2-10 mL, allowing several independent syntheses to be produced from the same quantity of materials used to produce a single, normal batch. This in turn could allow enough independent inter-batch catalysis trials to be made to quantify the poly-dispersity in the catalysis rates and thus to make a second, stronger evaluation of the hypothesis that ripple domain particles modulate catalysis.

An alternative method would be to generate ripple domain particles on pre-synthesized, mono-dispersed particles. This can be accomplished through the phenomenon of *ligand exchange* in which alkanethiols de-absorb and re-absorb onto a gold surface, allowing different ligands to be inserted into preformed monolayers. Currently it is not known if ligand exchange generates ripple domain nanoparticles and therefore for this method to be viable it must first be established if thermodynamically and kinetically ripple ordering occurs. If the answer to this question is yes, then monodispersed nanoparticles (which can be synthesized easily for non-polar, single ligand nanoparticles) could be used to generate ripple domain morphologies. The conjecture is that these monodispersed particles would give a better resolution and reproducibility of catalysis rate between batches, and therefore provide a better set of data to test ripple domain catalysis. Furthermore, the avoidance of synthesizing the nanoparticles with the catalyst ligand exposed to the reducing sodium borohydride will eliminate the concern of borate contamination.

5.2.2 Specificity and the Binding Constant

The observation that the binding constant of the nanoparticles is affected by the morphology of the ripple shell suggests further work to explore what structural features of the substrate affect the intermediate's formation. Using the same methodology developed in enzymatic biochemistry, it is envisioned that a series of similar substrates, each differing in only molecular detail, could be used in catalysis reactions and the binding constant determined for each. It is reasoned that the substrates that form good intermediates will show low binding constants, and this will give evidence of what factors in the structure most strongly affect the bound intermediate. Furthermore, this type of testing could be conducted under conditions of changing pH or temperature to test how changes in the catalyst site's reactivity contribute to the binding intermediate. Such probing trials could be used as a general method to explore the chemical and physical features of the local molecular structure in the ripple domain, providing a new tool for correlating morphology effects to observed properties.

5.2.3 Solvent Compatibility

It was observed that the homo-ligand catalyst particles performed with different catalysis rates in aqueous alcohol (3:2 $EtOH:H_2O$) and pure water. In aqueous alcohol the nanoparticles showed a catalyst rate lowered by a factor of ~ 30x compared to in aqueous water. In contrast, the ripple domain nanoparticles showed modulation that could actually be enhanced in aqueous alcohol by ~ 2x. This suggests exploring ripple nanoparticles as catalyst systems in alternative solvents. Ripple domain nanoparticles can have very different solubilities even in families of solvents that are quite similar structurally. Further work could look at how the solubility of a nanoparticle in a given solvent correlates to its catalytic reactivity. In conjunction, the solubility of the substrates could also be tracked to see if the ripple nanoparticles provide a better local environment to absorb and react molecules. The overall aim of this work would be to establish the unique solvent based solubility of catalyst ripple domain nanoparticles and see if it correlates to catalysis modulation. Such work could help understand better the chemistry of the monolayer interface, and select out solvent/particle matches that would be uniquely suitable for syntheses that are otherwise difficult to carry out in standard industrial or laboratory conditions.

5.3 Closing Remarks

The results of my thesis work contribute several significant aspects. First, although it is often stated that ripple domain nanoparticles are a facile system to synthesize, being easily self-assembled in a one step reaction and open to numerous types of ligands and therefore catalyst types, my work cautions that nanoparticle distributions can alter substantially both between syntheses and with changes in ligand structure, suggesting that nanoparticle data must be carefully analyzed and tested repeatedly to ensure statistical relevance. The ability to alter chemical reactions by fashioning a ripple domain shell opens the possibility for producing cheap, inexpensive catalysts with the type of specificity and reactivity desired in higher-catalysts such as enzymes. In considering biological systems, the current work gives evidence that ripple domain nanoparticles could be used as a platform on which to probe the type of solvent/substrate/catalyst/interface interactions seen in living organisms. These conjectures must still be solidified with stronger, statistically significant data, however if this proves substantial, I can imagine developing a test-bed ripple nanoparticle, tailored to have the same type of surface energy and catalyst site as seen on an enzyme that, when combined with the easy of synthesis and customization through ligand selection, could allow investigation of fundamental questions of biochemical mechanisms. Researchers have already begun exploring nanoparticles as enzyme analogs, but this work adds a new tool to these endeavors by showing that the ripple domain morphology itself, which represents a unique, confined environment at the solvent/monolayer interface, can influence the catalysis. Furthermore the ligands use to produce this ripple domain can be functionalized to allow several types of chemical groups to be presented into the ripple gap, allowing the assembly of a whole catalytic machinery in a single, well-defined nanostructure.

Finally, ripple domain nanoparticles opens the idea of using morphology and chemistry together to produce new, active materials. This idea shifts from considering just what type of chemical moiety is present to the idea of how these moieties are organized spatially. This idea is not new to chemistry or biology, but has now been extended to nanoparticles with this thesis. The observation of ripple domains affecting the binding constant and attempt frequency suggests that tailoring the interactions in the monolayer along with the chemistry of the catalyst site could elaborate nanoparticles as uniquely suited to a single molecule. It is imagined that further work on ripple domain nanoparticles could allow the synthesis of custom catalysts that can augment or even replace some of the processes now used in industry or research chemistry.

Experimental

Nanoparticle Synthesis

Materials are acquired from these sources: 100% ethanol, acetonitrile reagent grade, chloroform reagent grade, tetrahydrofuran reagent grade (VWR Internional), 11-(1N imidazo)-undecane-1-thiol (IT) catalyst was purchased in 200 mg units (ProChimia Surfaces), 1-octanethiol (OT), 1-hexadecanethiol (HD), 16-mercaptohexadecane-1-oic acid (MHA), hydrogen tetrachloroaurate 99% anhydrous, sodium borohydride 95% anhydrous, potassium hydroxide reagent grade (Sigma-Aldrich). 2,4-dinitrophenyl acetate (DNPA) (Acros Organics International). Deuterated chloroform and deuterium oxide, NMR spectroscopic grade (Cambridge Isotope Laboratory), Water (18 MΩ) was taken from a Millipore^{TM} filtration system. All reagents were stored in a refrigerator at ~ 10^{0}C, except for the IT catalyst which was stored at ~ 4^{0}C.

Nanoparticles for a given series were synthesized within a day to a week. For each ligand ratio a 250 mL round-bottom, one-neck flask (Chemglass) was rinsed with aqua regina (1:3 vol:vol nitric acid to hydrochloric acid) for 1-2 min, then rinsed consecutively with water, acetone, ethanol, and jet dried. Each flask is set into an ice bath over an Ika^{TM} stir plate (VWR International) with a 1 in. Teflon coated, pill stir-bar (VWR International). 149.4 µmol total of ligands is used per batch of particles, for a given ratio this total is split into the molar filler and catalyst quantities (e.g. for 1:1 MHA:IT this requires 74.5 µmol each of IT and MHA). The IT catalyst was warmed to room temperature and dissolved in ethanol to form a 50 mg / mL solution. The required amount of catalyst is taken from this liquid stock. 80 mL ethanol is added to the flask followed by 58.78 mg (173.0 µmol) hydrogen tetrachloroaurate salt to produce a yellow solution. This is stirred at medium vigor (no sloshing of solution against the walls) and the thiol ligands added, causing the yellow solution to turn a murky golden color. In all syntheses the filler ligand was added first, then the catalyst ligand. This solution is allowed to stir for > 10 min to cool. Meanwhile, to 80 mL ethanol is added 62.72 mg (1,657.9 μmol) sodium borohydride, in a 100 mL pyrex beaker, and stirred with a Teflon coated, pill stir-bar for at least 5 min to completely dissolve the crystals. Meanwhile, over each round-bottom flask is set a 60 mL syringe to which is attached a 21 gauge needle (21G2 - VWR International). The syringe needle is set down into the flask so that the syringe is just barely at the neck of the flask, but allowing air for pressure equilibration. When the 10 min time is up, the stirring on the flasks is increased to a vigorous speed, generating a full vortex in the solution and causing a uniform, controlled wave around the flask wall. To each of the syringes is added 1 mL of the sodium borohydride solution. This is allowed to drop fully, during which time the golden solutions turn a pale brown. This is repeated 2x, refreshing the sodium borohydride each time it finished dropping. After the third drop the syringes are filled and allowed to drop (this requires two stages, since the syringe only holds 60 mL). The ice baths and stirring are maintained throughout the dropping period. The syntheses will go from pale brown to dark brown to opaque purple or magenta, signaling the formation of nanoparticles. When the sodium borohydride solution has completely dropped the syntheses are allowed to stir for ~ 1 hr. The syntheses are then removed from the bath, capped and sealed with parafilm M (VWR International) and set into a freezer at ~ 4^0C overnight.

Purification of Nanoparticles – Centrifugation Method

For MHA-IT, HD-IT and low catalyst OT-IT syntheses, the particles precipitate cleanly out of the ethanol solution, leaving a purple precipitate and a slightly colored supernatant (purple or orange color). For these particles the purification can skip to the removal of the supernatant (described in the following). For high catalyst OT-IT syntheses and homo-ligand catalyst particles the precipitation in ethanol is incomplete. After ~12-24 hr, these particles are rotavaped (Buchner Instruments) down to about 1/4th their volume (~ 40 mL) and an equal volume of toluene added. The particles are then set back into the freezer and allowed to precipitate for ~12 hr. The particles are then allowed to warm to room temperature and the supernatant pipetted out by hand to take out as much solution as possible without losing precipitate material. This generally leaves 5 – 10 mL of solution / precipitate remaining. The remaining material is stirred together and pipetted into a set of 1.5 mL polypropylene centrifuge micro-capsules (microcaps) (VWR International). The material is centrifuged 5 min, 9,000 RPM in a micro-centrifuge, VWR Galaxy (VWR International). The resulting material is collected in a small pellet at the bottom of the tub and the supernatant can be decanted or pipetted off. The following centrifuge regiment is used to purify out the excess ligands and borate salts:

1. 3x total of organic solvent wash. For particles insoluble in ethanol, ethanol is the organic solvent. For particles insoluble in toluene, tetrahydrofuran (THF) is the organic solvent. Each refreshing of the solvent is accompanied by ultra-sonication (90 W) and/or vigorous vortex stirring until the pellet is completely gone from the bottom of the microcap.
2. Each microcap precipitate is mixed with 200 μL ethanol, sonicated to disperse, and then 800 μL Millipore water added. The material is agitated by sonication and vortex stirring and centrifuged at 5 min, 9,000 RPM.
3. The supernatant is removed and tested for borates (described later).
4. So long as the supernatant tests positive for borates *by eye observation* steps 2-4 are repeated.
5. When the borate test is negative, step 2 is repeated 3x more.
6. 1.5 mL of ethanol is added to each microcap but not agitated to disperse the pellet. The ethanol is then removed. This is done to remove as much water as possible.
7. The nanoparticles are then collected by dispersing the pellets in a total of 5 mL of ethanol. This is the nanoparticle *stock solution.*

For the MHA-IT particles the centrifuge procedure is modified. The particles cannot be washed with water so in step 2, 1000 μL of ethanol is used. The borate test is used as normal. In general this requires a larger number of wash cycles. For homo-ligand catalyst particles the water washing step sometimes turns the particles into a slime that coats the surfaces of the solvent and microcap. In these cases a pipette is used to carefully remove the supernatant while avoiding sucking up material. For further water washes, a greater portion of ethanol (300-500 μL) is used. For step 7, the MHA-IT particles are dissolved in water, the HD-IT particles are dissolved in reagent grade chloroform (Sigma-Aldrich).

Transmission Electron Microscopy (TEM) Analysis

For each particle batch, 10 μL of stock solution is mixed with 1000 μL ethanol and sonicated. 10-20 μL of this dilution are dropped onto a copper 300 mesh, formvar carbonized, carbon-coated TEM grid (Ladd Research) which is placed on a Kimi-Wipe (VWR International) to absorb excess liquid. TEM analysis is performed using a JEOL 200 CX Microscope or JEOL 2011 High Contrast Digital Microscope. TEM images are collected using a CCD camera and analyzed for particle distributions using ImageJ (ImageJ 1.38x Wayne Rasband, NIH, USA).

For analysis, each picture is first transformed with *threshold* to distinguish the particles as black and the background at white. It can be seen, as the threshold is scanned, that the background has single pixels of noise. The threshold is set just at the point that this population of noise pixels stops decreasing rapidly, which is about the point that the pixels in the nanoparticles begin to diminish below threshold. The *particle analysis* program is run using > 20 pixel cut off and circularity of ~ 0.5-1.0. Typical pictures are at magnification 40-50 kx. The resulting analysis gives a list of the viable particles and their pixel areas. The pixel areas are converted to a diameter assuming each particle is a sphere. The radius is converted to nanometers by measuring the pixel count in the scale bar in the image. The sequence for analysis is shown in **Figure E1**.

The diameters for each set of images are combined together and, using an in-house program, are put into a distribution, typically between 0 and 15 nm, with 0.2 nm bins. This distribution is fit to a lognormal distribution using the non-linear fitting program in OriginPro 7.0 (Origin Lab Corporation). From the fit lognormal distribution equation the expected value (mean) and standard deviation are calculated. The expected value, D, is used as the average nanoparticle diameter for that particle batch.

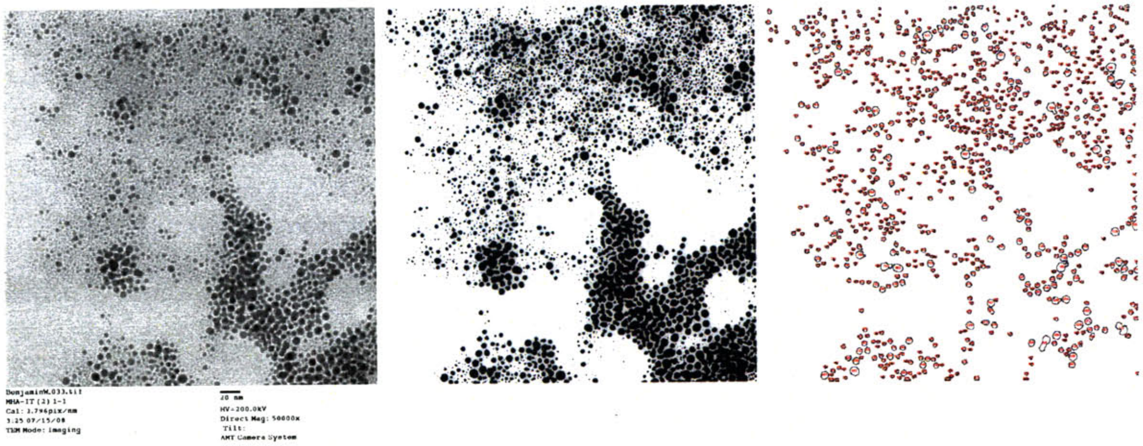

Figure E1: Stages of TEM image analysis using ImageJ. **(Left)** As taken digital TEM image. **(Middle)** Threshold adjusted image showing the conversion of nanoparticle cores to black and background to white. It is not possible to see the noise pixels referred to in the text in this image. **(Right)** Particle analyzed image, showing those particles that were identified in the image. It is seen that not all particles are captured, especially in the aggregates.

Thermalgravimetric Analysis (TGA)

TGA samples were prepared by taking 1 mL of nanoparticle stock and precipitating it in an equal volume of either ethanol (MHA-IT) or THF (OT-IT, HD-IT, IT). The solution is added to a set of microcaps and centrifuged 30 min, 14,000 RPM. The supernatant is removed and the resulting pellets allowed to dry with the microcaps upside-down on a Kimiwipe for ~ 12 hr. Once dry, the pellet can be dislodged by tapping the microcap. TGA samples are run on a TGA Q50 (TA Instruments) with a Thermostar Mass Spectrometer (Pfeiffer Vacuum). Samples are equilibrated at 25^0C then allowed to purge solvent at 100^0C for 2 hr. The sample is then ramped to 600^0C at 3^0/min. The sample dwells at 600^0C for 1 hr. The resulting TGA spectrum is analyzed using the analysis software in the TGA equipment to yield the percentage change in weight. This is taken as the *organic portion*.

Determination of Ligand Ratios

There are four methods used to determine the ligand ratio: synthetic (SYN) method, decomposed particles (DCP) method, post-synthesis supernatant (PSS) method, and elemental analysis (EA).

The SYN ratio is determined simply by the quantities of ligands added to the reaction. This is the ideal ratio but it is based on the pre-reaction quantities and it is not certain that these are the same ratios on the particles. Therefore this is the weakest estimate.

The DCP ratio is determined by taking 1 mL of nanoparticle stock and precipitating it as described for TEM. The precipitate is centrifuged 5 min, 5,000 RPM. The supernatant is removed and the pellet washed (without dispersing it) 3x with deuterated solvent, D_2O for MHA-IT and $CDCl_3$ for OT-IT, HD-IT, IT. 700 μL of deuterated solvent is then added and the pellet dispersed with sonication and vortex stirring and loaded into 5mm Economy NMR tubes (Wilmad Lab Glass). The NMR spectrum is recorded on a Varian-Mercury 300MHz spectrometer. In all samples prepared in this study only a solvent peak (due to excess, hydrogenated solvent) can be seen in these spectra and a very broad peak between ~ δ 1.5- δ 2.5 which is the aliphatic hydrogen signal. No signal is seen from the ligand molecules, demonstrating no free form ligands present in the sample. The sample is then added to a centrifuge microcap and 5 µL of a solution of iodine in ethanol (31.13 mM) is added. The tube is centrifuge 5 min, 3,000 RPM. The supernatant is removed and added to a new microcap. This process is continued until the nanoparticle hue (red-magenta) has disappeared, typically accompanied by a slight hue from the iodine, and no precipitate is formed from centrifugation, usually within 4 to 5 cycles. The supernatant is added to a 4 mL shell vial (VWR International) and the solvent removed carefully by rotavap. The dry product is then further dried on vacuum ~ 1-2 hr at 80^0C to remove as much iodine as possible. The final dry product is then redissolved in 700 μL deuterated solvent and a NMR tube prepared.

The NMR spectra is collected. The ratio of the integrated quantities from the imidazole aromatic peaks and the aliphatic peaks is used to determine the quantity of catalyst present in the particles. This is based on the assumptions: the ligands were liberated into solution by the iodine decomposition, the ligands have equal solubility at the given concentrations, and the iodine does not change the chemical structure of the ligands.

The PSS ratio is determined by taking 5 mL of the supernatant from the precipitated synthesis solution of each batch. The supernatant is rotavaped down to yield a white or yellow solid. 700 μL of $CDCl_3$ is added and the solid dispersed with sonication. Normally the solution is turbid from undissolved borates and salts. These salts are removed by filtering the solution through a 200 nm PTFE syringe filter (Whatman Scientific, GE Healthcare). The clear solution is then prepped into a NMR tube and the NMR spectrum taken.

The EA method was prepared only for MHA-IT 1-1 and 1-2 to check the validity of the other methods because of the large amount of material needed. 2 mL of nanoparticle stock were precipitated as described for TGA analysis. The pellets were dried at 100^0C for > 8 hr under membrane vacuum. The solid pellets were then shipped for carbon-hydrogen-nitrogen-oxygen-sulfur elemental analysis at Columbia Analytical Services Inc., Tuscon, AZ. Samples were tested at least in duplicate, and at max in triplicate. The resulting percentages were compared to the calculated expected values for the given ratios, and the resulting actual ligand ratios backtracked from the experimental results.

Calculation of Particle and Catalyst Concentrations

The nanoparticle concentration, <np> (M_{np}), was calculated by taking the UV-Vis absorbance at 540 nm and 850 nm of 50 μL of particle stock in 2000 μL trial solution (described later). The difference in the absorbances, Ab_{540}-Ab_{850} is taken as the particle absorbance Ab_{np} (AU). The extinction coefficient for each particle batch is determined from the empirical equation:

$$\ln(\varepsilon) = \ln(D)k + a \qquad \textbf{Equation E1}$$

Where ε is the extinction coefficient, D is the mean diameter of the particles in nanometers, k = 3.3211 and a = 10.80505. The nanoparticle concentration is then calculated by:

$$\langle np \rangle = \frac{Ab_{np}}{\varepsilon} \qquad \textbf{Equation E2}$$

The catalyst concentration, <cat> (M_{cat}), in any given solution is calculated by finding Ab_{np} from UV-Vis. The conversion factor, C (M_{cat}/AU), for each batch is calculated using the information from TEM, TGA and the ligand ratio analysis in the equation:

$$C = \frac{4\pi N_A P_{cat} P_{org} \rho_{Au} \left(\frac{D}{2}\times 10^{-7}\right)^3}{3\varepsilon \mu_{cat}\left(1-P_{org}\right)} = 23.917\times \left.\frac{P_{cat} P_{org} D^3}{\varepsilon\left(1-P_{org}\right)}\right|_{for\_IT\_catalyst} \qquad \textbf{Equation E3}$$

Where ε is the extinction coefficient, μ_{cat} is the molecular weight of the catalyst (254.44 g/mol for IT), P_{org} is the mass percentage of organic material (from TGA), N_A is Avogadro's Number, P_{cat} is the percentage of catalyst (determined from material analysis), ρ_{Au} is the density of gold (19.3 g/cc), and D is the mean diameter in nanometers. The catalyst concentration is calculated by:

$$\langle cat\rangle = C\times Ab_{np} \qquad \textbf{Equation E4}$$

Determining and Preparing Trial Solutions

To determine the amount of nanoparticle stock needed to acquire a given <cat> a centrifugation series was run. Typically, two microcaps were filled with the appropriate quantity of nanoparticle stock and buffer, with enough solvent to form a total volume of 1500 μL (the exact quantities are given in the table for each pH and nanoparticle system). It was found to be very important for mixing MHA-IT particles that the buffer and solvent were mixed thoroughly first and then the nanoparticle stock added second to prevent precipitation. Six pairs of two microcaps were prepared with quantities of nanoparticle stock ranging from 1 – 10 μL . This set of twelve caps is centrifuged at 5 min, 5,000 RPM. 1 mL of each microcap in each pair is combined to give 2 mL. The Ab_{np} is measured for these six solutions and the <cat> determined. A linear plot is generated and the linear relation between added nanoparticle stock and <cat> determined. Typically this method is repeated until the linear regime covers the amount of stock needed to generate <cat> ~ 4.0 M_{cat}. This requires usually running one or two centrifugation series with smaller nanoparticle increments to get a good resolution on the correct nanoparticle stock.

From the centrifugation series the nanoparticle stock that gives <cat> ~ 4.0 is used for all catalysis trials. A trial solution is prepared for each catalysis trial in the following manner: in a 20 mL scintillation vial (VWR International) that has been jet-blasted to remove dust, the appropriate quantities of nanoparticle stock, buffer and solvent are added to give a total volume of 5000 μL . This solution is vortex stirred for ~ 30 sec vigorously and sonicated for ~ 10 sec. The solution is then added to three microcaps (not all solution is used) and centrifuged 5 min, 5,000 RPM. 1 mL of supernatant is removed carefully from the top of the each microcap and added to a 4 mL shell vial that has been jet-blasted to remove dust. This is the trial solution and is ready for use in a catalysis trial.

Catalysis Trials using Ultraviolet-Visible Absorbance Spectrometer

This method is used for measuring the overall kinetic curves for the acidity experiments, catalysis experiments, and multiple catalysis experiments. UV-Vis spectra are recorded on either an Agilent 8453 or Ocean Optics QE65000 spectrometer, the kinetic data is equivalent from each machine. A 3.5 ml, 10 mm path-length, quartz, septum-sealed, screw top cuvette (1/Q/10-GL14-S, Starna Cells Incorporated) is cleaned with aqua-regina, water, acetone and then jet dried. The cuvette, filled with 3000 μL of the required buffer and solvent, is used to blank the background. The cell is then emptied, dried and filled with the trial solution. The absorbance spectrum is taken to record Ab_{np} and check for the correct <cat> (~ 4.0 M_{cat}). To begin a catalysis trial 42.6 μL of a 1.77 mM_{sub} DNPA stock in acetonitrile is added to the cuvette. The cuvette is quickly capped, turned upside down slowly and evenly three times to completely mix the solutions, and then reset in the cuvette and the kinetic curve recorded. The total dead time is estimated at ~ 30-40 sec. The time necessary for a complete trial depends on the nanoparticles: OT-IT, HD-IT, IT in 3:2 ethanol : water ~ 12-24 hr, MHA-IT ~ 4-6 hr. As described previously, for the OT-HD-IT system, only the first two hours were recorded for measuring the kinetic rates, but the full day was used to confirm the overall kinetic curve. In a typical trial the absorbance is measured at 400 and 360 nm (the absorbance of DNPA and DNP-OH), 255 nm (a secondary peak of DNPA and DNP-OH), 850 nm (baseline), 540 (nanoparticle plasmon). The increase in absorbance at 400 is the signal of DNPA hydrolysis. The concomitant decrease in 255 nm is used to verify hydrolysis is occurring. The kinetic curve is generated by finding the hydrolysis absorbance, Ab_{cat}, taken as $Ab_{400} - Ab_{850}$. To obtain the maximum Ab_{cat} (i.e. the signal for complete DNPA hydrolysis) when the catalysis trial is over, 50 μL of ~ 1 mg / mL aqueous potassium hydroxide solution is added to the cuvette and mixed thoroughly. The Ab_{cat} is recorded. This process is continued until the Ab_{cat} does not change with the addition of potassium hydroxide. This is recorded as the final absorbance, $Ab_{cat\text{-}final}$.

The kinetic curve is converted from Ab_{cat} to the percentage of product formed, <P>, by normalizing by $Ab_{cat\text{-}final}$. The time is converted into seconds. The <P> kinetic curve is fitted to an associated exponential growth equation using OriginPro 7.0:

$$\langle P\rangle = \langle P_0\rangle + A\left(1 - e^{-\frac{t}{\tau}}\right)$$ **Equation E5**

The important parameter is time constant τ (sec). From this the *observed catalytic rate*, k_{ob} (sec^{-1}), is determined by $k_{ob} = 1/\tau$. This is converted to the catalytic rate, k_{cat} ($1/sM_{cat}$), by:

$$k_{cat} = \frac{k_{ob} - k_0}{\langle cat \rangle} \qquad \textbf{Equation E6}$$

Where k_0 is the observed catalytic rate for the background solvent without nanoparticles. The background catalysis rate of 3:2 ethanol : water is $k_0 = 1.25 \times 10^{-6}$ 1/s and in pure water $k_0 = 20.00 \times 10^{-6}$ 1/s.

Temperature Dependent Catalysis Trials

The set up for catalysis is the same as described previously. The catalysis trials are run on an Agilent 8453 with a Peltier temperature control cell. The temperature is set and the trial solution in the cuvette allowed to equilibrate for 10 min before adding the DNPA and starting the catalysis trial. Trials were only run for 2 hr on MHA-IT because of the rapid catalysis rate.

Catalysis Trials using 96-Plate Reader Ultraviolet-Visible Absorbance Spectrometer

This method is used for the kinetic binding constants method and reproduction intra-batch experiments. Typically 36 microcaps of 1500 μL total trial solution for a nanoparticle batch were prepared and centrifuged. 200 μL of each microcap were added to a new, polypropylene, 96-well plate (BD Falcon) making four columns of eight wells each. For the kinetic binding constants eight DNPA stock solutions were prepared in the following way: a 2 mL, 16.81 mM_{sub} DNPA in acetonitrile solution was prepared. 1 mL of this solution was removed for the first stock solution. The remaining solution is diluted by a half with the addition of 1 mL acetonitrile. This process was continued to generate a dilution series of halves for eight substrate stocks (s1 – s8). For the intra-batch experiments only the s3 (4.20 mM_{sub}) stock was used.

Catalysis trials were recorded with a 96-Plate Absorbance Spectrometer (SpectraMax). For the kinetic binding constant experiments, eight wells were run at one time. The Ab_{np} was measured for each well (note – this number does not correspond to that found on the Agilent and Ocean Optics spectrometers, and must be scaled to correlate the two with the knowledge that the trial solution is <cat> ~ 4.0 M_{cat}). As quickly as possible, 10 μL of each stock is then added to a well in order, using a fresh pipette tip for each addition. With each addition the well is stirred with the tip, pumped several times, stirred, and then pumped again (total time ~ 10 sec / well). The stocks are added starting from the lowest substrate concentration to the highest. The substrate concentrations, <sub>, for the stocks are: 800, 400, 200, 100, 50, 25, 13, 6 μM_{sub} for stocks s1 to s8 respectively. The plate is read and the initial linear kinetic regime collected. Typical parameters are 60 sec of agitation, 10 min scan at 22 second intervals, reading 400 nm (product absorbance), 540 nm (nanoparticle plasmon) and 850 nm (baseline absorbance). The initial observed catalytic rate, u_{ob} (sec^{-1}), can be obtained by taking the slope of a linear fit to the data. The initial catalytic rate, u_{cat} ($1/sM_{cat}$) is calculated just as for k_{cat}, using the observed rate for the background solvent. For the intra-batch experiments the same procedure is followed but only the s3 stock is used for all the wells.

Calculating the Catalytic Properties

To calculate the activation energy, E_A (kJ/mol) and attempt frequency, υ_{atp} (sec^{-1}), the natural logarithm of the catalytic rates was plotted against the inverse temperature, taken from the temperature dependent catalysis trials. The resulting Arrhenius plot is fitted to a line to obtain E_A and υ_{atp} :

$$\ln(k_{cat}) = \frac{RE_A}{T} + \ln(v_{atp}) \qquad \textbf{Equation E7}$$

To calculate the binding constant, K (M_{sub}) and maximum initial catalysis rate, k_{max} ($1/sM_{cat}$), the initial catalytic rates were plotted against the substrate concentration <sub>, taken from the kinetic binding catalysis trials. An exponential curve was fit to the plot using OriginPro 7.0 to give K and k_{max}:

$$u = \frac{k_{react}\langle S_o\rangle}{K + \langle S_o\rangle} \qquad \textbf{Equation E8}$$

The kinetic binding trials were run in triplicate and the binding constants and k_{max} averaged

Knoevengel Condensation Reaction

For each ligand ratio, a 40 mL, long-body, scintillation vial (VWR International) was jet-blasted to remove dust, rinsed with ~ 5 mL of chloroform, and jet dried. Each vial is loaded with 8 mL reagent grade chloroform, 10.50 mg (69.48 µmol) NBA, 25 µL (234.95 µmol) ECA, and enough nanoparticle stock solution to give an excess ratio <NBA>/<cat> (mol/mol) ~ 4.0. Each solution is sonicated for ~ 30 sec each and an initial sample of 10 µL removed. A Teflon-coated pill stir-bar is added to each vial and the vial is sealed. The vials are suspended into a silicon oil bath at

65^0C so that the solvent and oil levels are equal. The vials are stirred vigorously. Every hour the vials are removed from the oil bath one by one and 10 µL removed. To avoid contamination in the hot chloroform, a 10 µL micro-capillary with a pump bulb was used to extract the sample. The vial is then sealed and returned to the oil bath. It required 2-3 min for each sample to be extracted.

Each 10 µL extracted sample is added to 3 mL chloroform, mixed thoroughly, and measured for a UV-Vis absorbance spectrum. The ECNA product absorbance, $Ab_{ECNA} = Ab_{303} - Ab_{850}$, and NBA substrate absorbance, $Ab_{NBA} = Ab_{265} - Ab_{850}$, measured. The concentrations, in µM, are given by:

$$\langle ECNA \rangle = 35.205 \times Ab_{ECNA} + 1.026 \qquad \textbf{Equation E9}$$

$$\langle NBA \rangle = 65.411 \times Ab_{NBA} - 1.252 \qquad \textbf{Equation E10}$$

The reactions were allowed to run up to one full day. The appearance of a yellow color in the solution is evidence of ECNA formation.

(Z)-ethyl 2-cyano-3-(4-nitrophenyl)acrylate (ECNA)

In a 250 mL round-bottom, one neck flask (Chemglass), 1.29 g (8.54 mmol) NBA, 1 mL (9.40 mmol) ECA, 1 mL (12.36 mmol) pyridine and 120 mL 100% ethanol were added. The flask is sealed with a water-cooled condenser and refluxed with vigorous stirring at $70\text{-}75^0C$ for 12 hr. A white/yellow precipitate forms within minutes. After the reaction cools, the precipitate is collected on filter paper with a Buchner funnel and vacuum, washing with copious amounts of ethanol. The precipitate is scraped into a 20 mL scintillation vial and dried on vacuum for 2 hr. NMR of the product shows the requisite peak structure. A concentration series of UV-Vis absorbance at 303 nm was used to determine the Bier equation for <ENCA> (given previously).

^{1}HNMR, 300 MHz, $CDCl_3$,
δ 1.42 $C\underline{H_3}CH_2OC(O)$-, t, 3H, J = 7.2 Hz
δ 4.43 $CH_3C\underline{H_2}OC(O)$-, qd, 2H, J_A = 3.6 Hz, J_B = 10.8 Hz
δ 8.13 ene-side of phenyl, dd, 2H, J_D = 4.5 Hz, J_{DD} = 0.3 Hz
δ 8.32 nitro-side of phenyl, d, 2H, J = 5.6 Hz
δ 8.37 –OC(O)C(CN)=C$\underline{H}$-, s, 1H

Borate Test

This test is qualitative and was used only to indicate the presence of borates. The test solution is mixed from 10.50 mg (69.48 µmol) NBA, 25 µL (234.95 µmol) ECA and 8 mL tetrahydrofuran (THF). To test for borates, 200-500 µL of test solution is added to 1 mL of tested solution and shaken. If the solution turns orange-yellow immediately then borates are present in the solution. For alcohol solvents a precipitate of ECNA forms rapidly after mixing.

Statistical Analysis

Analysis of Variance (ANOVA) and hypothesis testing (t-test) were performed using the statistical software in OriginPro 7.0. Unless indicated, the significance levels were calculated at 99%, α = 0.01.

TGA Organic Portion Estimation Calculation

To calculate the organic portion the archetypical Au(111) thiol monolayer was used. This monolayer produces a lattice with ~ 1 thiol per 3 gold atoms. For a given particle batch, the area and volume were calculated for each diameter in the distribution. From the area is calculated the number of surface gold atoms using the lattice constant of Au(111). From the volume is calculate the mass of gold, the inorganic portion, using ρ_{Au} = 19.3 g/cc. The number of thiols is calculated from the number of surface gold atoms, and this separated into the filler and catalyst populations by the ligand ratio. The mass of the organic portion is calculated. The inorganic, organic and total masses for each diameter were scaled by the normalized distribution. The ratio of the summed organic mass and summed total mass was taken as the calculated organic portion.

Bootstrap Calculation

The bootstrap calculation is an attempt to show the spread of catalytic rates that could be generated from the experimental conditions. This involves generating catalytic rates using the distributions of each parameter used to calculate the rate. To do this the catalytic rate was broken into five parameters: average diameter, D, organic portion, ligand ratio, Ab_{cat} and observed catalytic rate. For all parameters there are only two data points (the two syntheses) for each particle batch thus the deviations are large and this calculation represents a conservative estimate of the spread. Using these parameters and a random number generator, a set of 2000 independent calculations was run which calculate the conversion constant, the concentration of catalyst and the resulting catalytic rate. For each calculation, for each of the five parameters, a value was randomly generated that was the mean +/- one, two or three deviations. The calculations generating the rate constant are the same as described in the previous parts of the experimental section, except now the empirical data is replaced by the randomly generated parameter. From the 2000 calculations a distribution was generated and fit to a log-normal, giving the mean, expectation value and deviation. The 2000 sample calculation was repeated three times and the catalytic rate values averaged.

Appendix 1: Catalysis and Basic Kinetics

Catalysts operate to speed up a reaction with two primary methods – serving either to decrease entropy or act as an intermediate. Enzymes are considered to function through a molding process where their reactive site captures and strains a molecule so that it becomes more reactive. The fundamental basis for this reactivity is a significant change in entropy (*41-44*). Solid state catalysts such as metals, ionic solids, as well as organometallics and some organic catalysts, function as reservoirs, providing low energy states through which electrons can be donated and accepted between molecules. These two operations are not exclusive, and many catalysts use both in combination. In all cases, the catalyst speeds up the chemistry by increasing the probability of reaction, and this is done by priming the molecule (structurally and electronically) into a reactive configuration.

To prime molecules, each catalyst possesses a *local environment* – an array of atomic structure, electron orbitals and consequential electromagnetic gradients. Each local environment is morphologically and energetically suited to stabilize a molecule in a higher energy transition state. The crux of this capability is conjectured to be due to local environment compensating destabilizing electronic states – twisted bonds, concentrations of charge, repulsive strain – by locating counteracting electronic density around the molecule, partly negating the interactions that would drive the molecule to its lower energy, stable state. Sometimes this involves transfer of charge or mass, as seen in the case of metal centers which absorb molecules and "weld" them together through sequences of insertion, oxidation, reduction and elimination. These are all transitions that could not be sustained without the guiding environment of the catalyst. The key concept is that by placing molecules which normally would not react into the correct, structural arrangement a chemical reaction can be induced. The focus becomes understanding how to generate such structures.

Catalysts are not consumed by the reaction they enhance, and this is because they link chemical reactions of opposite mass and charge transfer. Hydrolysis of an ester provides a simple example: one reaction is the "reduction" of water to hydroxide by the abstraction of a proton. This is both a mass and electron transfer for the catalyst which must acquire the cationic proton. The hydroxide is then free to attack the ester carbonyl and generate the alkoxide ion. A reverse mass and charge transfer of the proton "oxidizes" this ion to the free alcohol.

The basic parameter to characterize a catalytic reaction is the *catalytic rate (turnover rate)*, k_{cat}, which represents the number of reactions the catalyst runs in a given time. Faster catalysts are associated with "better" catalysts because they carry out more reactions in a given time.
The basic catalytic process can be depicted schematically. A substrate, S, associates with an active site, *, and forms a bound intermediate, S*. This intermediate can either decay back to the free substrate or proceed through a transformation to the product, P, as shown in **Scheme 2.4.1**.

$$S + * \underset{k\text{-unbind}}{\overset{k\text{-bind}}{\rightleftharpoons}} S^* \xrightarrow{k\text{-react}} P$$

Scheme 2.4.1: Catalysis reaction in with a substrate, S, and catalysis site, *, bind to form an intermediate, S*. This intermediate then reacts to form a product, P. In this reaction the intermediate is assumed to be able to break apart back to the original reactants, or proceed irreversibly to the product. The associated rate constants, k, are given for each step in the reaction.

Kinetics assumes the change in a substance's concentration is proportional to the concentration, and the portion is given as the rate constant. Defining the *number* of available catalysis sites, N, and the *fraction* of sites filled with substrate, θ, the catalytic process rates are (*43*):

$$\frac{-d\langle S\rangle}{dt} = Nk_{bind}(1-\theta)\langle S\rangle - Nk_{unbind}\theta \qquad \textbf{Equation A1}$$

$$\frac{d\langle \theta\rangle}{dt} = k_{bind}(1-\theta)\langle S\rangle - (k_{unbind} + k_{react})\theta \qquad \textbf{Equation A2}$$

$$\frac{d\langle P\rangle}{dt} = Nk_{react}\theta \qquad \textbf{Equation A3}$$

For our purpose, the last equation is the most important, giving us the catalytic rate, k_{cat}. To simplify the equations, it is assumed that the active sites are filled and vacated in the same proportion, allowing a steady state approximation:

$$\frac{d\langle\theta\rangle}{dt} = 0 = k_{bind}(1-\theta)\langle S\rangle - (k_{unbind} + k_{react})\theta \quad \textbf{Equation A4}$$

$$\theta = \frac{\left(\frac{k_{bind}\langle S\rangle}{k_{unbind} + k_{react}}\right)}{1+\left(\frac{k_{bind}\langle S\rangle}{k_{unbind} + k_{react}}\right)} \quad \textbf{Equation A5}$$

Solving for the product rate gives:

$$\frac{d\langle P\rangle}{dt} = Nk_{react}\frac{\left(\frac{k_{bind}\langle S\rangle}{k_{unbind} + k_{react}}\right)}{1+\left(\frac{k_{bind}\langle S\rangle}{k_{unbind} + k_{react}}\right)} = \frac{Nk_{react}\langle S\rangle}{K+\langle S\rangle} \quad \textbf{Equation A6}$$

$$K = \left(\frac{k_{unbind} + k_{react}}{k_{bind}}\right)$$

This is the basic catalysis rate equation. The second form of the equation is typically used in organic and biochemical catalysis and is known as the *Michaelis-Menten Formulation* (*45*). The factor K (units M_{sub}) is called the *binding constant* which quantifies how well the catalyst forms the bound intermediate. A lower K means less substrate is needed to fill up the binding sites, a.k.a. the catalyst binds more strongly to the substrates.

In most catalyst reactions, the chemical transformation is much faster compared to the intermediate formation (i.e. $k_{react} >> k_{bind}$, k_{unbind}) leading to:

$$\frac{d\langle P\rangle}{dt} = \frac{-d\langle S\rangle}{dt} \sim \frac{Nk_{react}\langle S\rangle}{\frac{k_{react}}{k_{bind}} + \langle S\rangle} \sim \frac{Nk_{react}\langle S\rangle}{\frac{k_{react}}{k_{bind}}} \sim Nk_{bind}\langle S\rangle \qquad \textbf{Equation A7}$$

Where the product has been converted to substrate using <P> = <S$_o$> - <S> (<S$_o$> is the initial substrate concentration). This equation integrates to give the basic rate formula:

$$\langle P\rangle = \langle S_o\rangle\left(1 - e^{-k_{obs}t}\right) \qquad \textbf{Equation A8}$$

Where the observed rate is $k_{obs} = Nk_{bind}$. The catalyst rate (units 1/sM$_{cat}$) is given then as:

$$k_{cat} = k_{bind} = \frac{k_{obs}}{N} \qquad \textbf{Equation A9}$$

The rate formula allows a determination of the catalysis rate by measuring experimentally the substrate (or product) change with time. In general, the observed rate is the sum of both the catalysis and any background reactions (such as induced by the solvent or contaminates) and thus these intrinsic rates must be subtracted off to obtain the catalyst rate.

Equation A6 shows that the catalyst rate depends in a non-linear manner on the concentration of substrate present; therefore reproducibility and comparison of catalysis rates requires a strict control of the starting substrate quantity. Measurements of changes in the catalysis rate as a function of substrate concentration can yield information on the intermediate kinetics of the reaction, in particular the binding constant of the reaction and the maximum obtainable rate. To see this, we can re-insert **Equation A8** into **Equation A6**:

$$\langle S\rangle = \langle S_o\rangle e^{-k_{obs}t}$$

Equation A10

$$\frac{d\langle P\rangle}{dt} = \frac{Nk_{react}\langle S_o\rangle e^{-k_{obs}t}}{K + \langle S_o\rangle e^{-k_{obs}t}}$$

If we consider the beginning of the reaction, at t ~ 0, then a preliminary change in product concentration $\Delta\langle P\rangle/\Delta t$ will be approximately equal to the number of catalyst sites present times the *initial rate of reaction*, u:

$$\left.\frac{\Delta\langle P\rangle}{\Delta t}\right|_{t\sim 0} \sim Nu \qquad \textbf{Equation A11}$$

Inserting this relation into **Equation A10** yields:

Equation A12

$$u = \left.\frac{k_{react}\langle S_o\rangle}{K + \langle S_o\rangle}\right|_{t\sim 0}$$

If we use the assumption the reaction rate, k_{react}, is must faster than the binding rates we obtain:

Equation A13

$$u \sim k_{react}$$

The reaction rate, k_{react}, is often called the *maximum catalytic rate* or k_{max}, because it is the absolute fasted rate at which the catalysis can proceed. The chemistry of the reaction determines the maximum catalytic rate, and therefore changes in the mechanism or electrostatics of the chemistry can causes changes in the maximum rate.

The initial catalysis rate, u, used above can be approximated from the full rate equation, **Equation A8** by taking the limit as t → 0, yielding:

$$\langle P\rangle\big|_{t\sim 0} \approx \langle S_o\rangle k_{ob} t \equiv utZ$$

Equation A14

Where Z is the number of active catalyst sites (i.e. sites have become bound to substrate molecules). For catalyst systems in which the concentration of substrate is far greater than the binding constant of the catalyst, Z ~ N, the total number of catalyst sites present.

Analysis of a more complicated reaction, involving two substrates which must bind together on a single catalyst site as shown in **Scheme 2.4.2**, describes better the type of hydrolysis reactions used in this work:

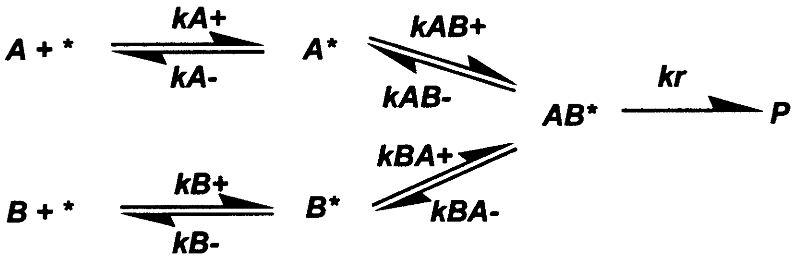

Scheme 2.4.2: Catalysis reaction in which two substrates, A and B, must bind to the same catalyst site, *, to form an intermediate, AB*, before reacting to the product, P.

The rate equations for this reaction can be written as before:

$$-\frac{d\langle A\rangle}{dt} = Nk_A^+\langle A\rangle(1-\theta_A-\theta_B-\theta_{AB}) - Nk_A^-\theta_A - Nk_{AB}^-\theta_{AB}$$

Equation A15

$$-\frac{d\langle B\rangle}{dt} = Nk_B^+\langle B\rangle(1-\theta_A-\theta_B-\theta_{AB}) - Nk_B^-\theta_B - Nk_{BA}^-\theta_{AB}$$

Equation A16

$$\frac{d\theta_A}{dt} = k_A^+(1-\theta_A-\theta_B-\theta_{AB}) + k_{AB}^+\theta_{AB} - k_A^-\theta_A - k_{AB}^-\theta_A$$

Equation A17

$$\frac{d\theta_B}{dt} = k_B^+(1-\theta_A-\theta_B-\theta_{AB}) + k_{BA}^+\theta_{AB} - k_B^-\theta_B - k_{BA}^-\theta_B$$

Equation A18

$$\frac{d\theta_{AB}}{dt} = k_{BA}^+\theta_B + k_{AB}^+\theta_A - k_{AB}^-\theta_{AB} - k_{BA}^-\theta_{AB} - k_r\theta_{AB}$$

Equation A19

$$\frac{dP}{dt} = N\theta_{AB}k_r$$

Equation A20

Using the steady-state approximation the product rate can be solved:

$$\frac{dP}{dt} = Nk_r\frac{a_1(1-b_1)k_{AB}^+ + b_1(1-a_1)k_{BA}^+}{g(1-a_1b_1) + (a_2-a_1b_2)k_{AB}^+ + (b_2-b_1a_2)k_{BA}^+}$$

Equation A21

Where the constants are given by:

$$a_1 = \frac{k_A^+}{k_A^+ + k_A^- + k_{AB}^-} \qquad a_2 = \frac{k_{AB}^+ - k_A^+}{k_A^+ + k_A^- + k_{AB}^-}$$

$$b_1 = \frac{k_B^+}{k_B^+ + k_B^- + k_{BA}^-} \qquad b_2 = \frac{k_{BA}^+ - k_B^+}{k_B^+ + k_B^- + k_{BA}^-}$$

$$g = k_{AB}^- + k_{BA}^- + k_r$$

This rate equation is *second order* due to the dependence on both the substrate concentrations. As is relevant to the experimental conditions of this study, three approximations reduce the complexity of this second order equation to the first order described previously. First, if the chemical transformation happens much faster than all other kinetic processes (k_r >> all other k) the product rate simplifies to:

$$\frac{dP}{dt} \sim N\frac{a_1(1-b_1)k_{AB}^+ + b_1(1-a_1)k_{BA}^+}{(1-a_1b_1)} \qquad \textbf{Equation A22}$$

The constants k_{AB}^+ and k_{BA}^+ are the rates for binding the second substrate to the catalyst site. If we assume the presence of one substrate does not affect the capability to bind the second (i.e. A* and B* are equivalent to free sites), we can relate these rates to the substrate concentrations:

$$k_{BA}^+ \cong k_A^+\langle A\rangle \quad k_{AB}^+ \cong k_B^+\langle B\rangle \qquad \textbf{Equation A23}$$

If one of the substrates, B, is considered to be in excess over the other substrate (<B> >> <A>), such that the rate of substrate B's capture is very fast (k_B^+ >> all over k) we can further simply the product rate to:

$$\frac{dP}{dt} = -\frac{dA}{dt} \sim Nk_A^+\langle A\rangle \qquad \textbf{Equation A24}$$

This recaptures the first order equation derived previously. Since this equation actually yields from a second order rate it is termed *pseudo-first order* to imply that one of the substrates, by being in high excess, does not affect the rate of reaction.

Besides the catalysis rate, the catalytic equation allows the definition of the *catalytic efficiency (specificity constant)* η:

$$\eta = \frac{k_{cat}}{K} \qquad \textbf{Equation A25}$$

The efficiency measures the potency of a catalyst; a very efficient catalyst requires a lower concentration to react the same substrate quantity compared to an inefficient catalyst. The most efficient catalysts in diffusion situations can obtain efficiencies close to the absolute limit of ~ 9-10 x 10^9 1/Ms (*45*).

Finally, molecular catalytic reactions follow thermodynamic law and therefore are subject to thermal activation. The relationship of temperature to catalytic rate is given approximately by the *Arrhenius Equation*:

Equation A26

$$k_{cat} = \nu_{atp} e^{-\frac{E_A}{k_b T}}$$

Where ν_{atp} is the attempt frequency (sec^{-1}) , E_A is the activation energy, and k_b is Botlzmann's constant.